MASTER OF SCIENCE THESIS

A SENSOR-BASED LAMINAR-TURBULENT WALL-STRESS MODEL FOR LARGE EDDY SIMULATION

Kin Sam LAM

Faculty of Aerospace Engineering · Delft University of Technology

TU Delft Delft University of Technology

Challenge the future

A SENSOR-BASED LAMINAR-TURBULENT WALL-STRESS MODEL FOR LARGE EDDY SIMULATION

MSc. Thesis

to obtain the degree of MSc.
at Delft University of Technology,
to be defended in public on Thursday, September 14, 2023 at 13:45.

by

Kin Sam LAM

This MSc. thesis is supervised by

Responsible thesis supervisor: prof. dr. Habil. S. Hickel
Company supervisor: Dr. V. Pasquariello

Composition Graduation Committee:

Chairperson of the Committee:
Prof. Dr. Ing. Habil S. Hickel — Delft University of Technology

Independent Examiner:
Dr. D. Ragni — Delft University of Technology
Dr. S.J. Hulshoff — Delft University of Technology

External:
Dr. V. Pasquariello — Lilium eAircraft GmbH

An electronic version of this MSc. thesis is available at
http://repository.tudelft.nl/.

Contents

ACKNOWLEDGEMENTS

During my MSc. thesis I had the privilege of having two knowledgeable supervisors supporting me every week. Vito, I have bothered the most, with whom I have discussions about my thesis almost daily. I am thankful for all your time and patience even with all your work. In the same way, I thank Stefan for taking the time to meet with us every week or sometimes multiple times a week. I know that not all students have the privilege of being able to meet with their supervisor(s!) multiple times a week.

While I originally came back with the sole reason of finishing my studies, I definitely stayed due to all the amazing people I have met this year. To keep this short, I thank all my friends and colleagues for keeping me sane. I would also like to thank my whole team for listening to me every week while I struggled with my thesis.

Finally, I thank all the friends and students I met, hung out, studied and worked with during my studies whom I share varying levels of camaraderie. There are too many to mention, but I thank and wish them all well in their future ahead.

ABSTRACT

Wall-modeled large eddy simulations (WMLES) are becoming an increasingly viable tool to study complex unsteady turbulent flows. Conventional wall models applied in these simulations are however not applicable to laminar boundary layers. While these encompass only a tiny fraction of the total surface area, erroneous predictions in this region of the flow can greatly impact the downstream flow field. In the present study, a new wall model is proposed by combining the laminar wall model and turbulent wall model with the use of a transition model marking the laminar and turbulent regions. The proposed wall model is applied to the laminar flat plate, wedge and laminar NACA 0012 flow. Results show that errors incurred at the unresolved leading edge, where the similarity solution used by the laminar wall model is invalid, accumulate in the velocity profiles for the flat plate and wedge flow cases. In underresolved regions near the leading of the NACA 0012 or near the tip of the wedge, good approximations to reference data have been found. The proposed wall model is also applied to a high Reynolds number flow involving an airfoil near stall. The proposed wall model shows promising results with good agreement for the skin friction distribution, especially in capturing the laminar skin friction peak if the transition location is known. However, the transition sensor considered for switching between the laminar and turbulent mode of the wall-stress model performs unsatisfactory. Other discrepancies in the results, such as capturing the laminar separation bubble and trailing edge separation are attributed to the relatively coarse meshes used. Last but not least, the computational cost incurred by the new wall model is marginal.

List of Figures

LIST OF TABLES

1

INTRODUCTION

Computational fluid dynamics (CFD) is increasingly used in both academia and industry to study fluid flows in a wide range of applications, ranging from the design of aerospace vehicles, turbomachinery, and HVAC systems to the analysis of blood flow in cardiovascular systems made possible by an abundance of computational power in recent years. In academia, performing direct numerical simulations (DNS) have consequently become much more viable to study the mechanisms of turbulence in all its details. However, the computational cost required to perform DNS in engineering is still out of reach as the required effort scales poorly with Reynolds number.

In the past several decades large eddy simulation (LES) has grown out to be one of the focus in academic turbulence research to analyze unsteady turbulent flows. In particular, LES is becoming increasingly attractive for higher Reynolds numbers as the computational effort increases significantly less compared to DNS as LES only resolves the largest turbulent structures, while smaller, more universal, structures of the flow are modeled using a sub-grid scale (SGS) model.

Nevertheless, the use of LES in industry is still limited due to the cost in adequately resolving the turbulent structures in boundary layers. Simply because the boundary layers are much thinner in size relative to the actual geometries simulated which requires a very high resolution near the walls. To make matters worse, the cost to resolve boundary layers also scales poorly with Reynolds number. Indeed, it is this "near-wall problem" that prevents LES to be widely used in industry.

In the last fifty years, numerous studies have proposed to model (part of) the boundary layer rather than resolving it. These proposals have consequently introduced two sub-variants of LES. Namely, Detached Eddy Simulation (DES) which performs a LES but models the full boundary layer and Wall-Modeled Large Eddy Simulation (WMLES) in which, in contrast to DES, resolves the outer part of the boundary layer ($\approx 80\%$) and models the wall-shear stress that results from the small-scale structure of the inner layer.

Intuitively, resolving more of the physics of the flow implies a more accurate solution but at a higher computational cost. Hence, WMLES should be able to reconstruct the flow more accurately than DES but worse than wall-resolved LES (WRLES). Perhaps

excellent wall-modeling causes the solutions retrieved from WMLES to come close to WRLES with significantly lower cost.

Many wall models have been proposed to improve the conventional equilibrium wall model (EQWM) in turbulent boundary layers. Recently, also the importance of modeling laminar boundary layers has been noted (Dauricio & Azevedo, 2022; Gonzalez et al., 2020). In addition, a general wall model requires a transition model.

Indeed, this master thesis focuses on WMLES and aims to answer the question: "How does the proposed laminar-turbulent wall model in a sensor-based approach compare to a turbulent equilibrium wall model?". To answer this question, several sub-questions are formulated:

- Can the Falkner-Skan wall model improve the shear stress prediction compared to the linear wall model?
- What are the differences in the predicted velocity field of wall-bounded flow compared to an EQWM?
- What are the differences in the predicted wall shear stress of wall-bounded flow compared to an EQWM?
- How robust is the laminar-turbulent sensor in distinguishing laminar and turbulent regions over a surface?
- What is the difference in computational cost between the proposed wall model and the EQWM?

The outline of the master thesis is as follows. The literature review in chapter 2 introduces the topic and problem at hand. Then, the methodology of the present code is discussed in chapter 3. After which the features implemented for this thesis are elaborated. Namely, the proposed laminar wall model (chapter 4), and the transition model (chapter 5). Next, the newly implemented features in the present solver are tested by first performing academic test cases and lastly a more application-based test case which tests the integration of the features in the present solver. These test cases are discussed in chapter 6. Finally, a conclusion and recommendations for future work is given in chapter 7.

This thesis is performed in cooperation with a company with the aim to improve the wall-modeling capabilities in their in-house LES code.

2

Literature Review

Firstly, the cost comparison is addressed in section 2.1. Afterwards, the relevant boundary layer theory is discussed in section 2.2. Subsequently, conventional to novel wall-modeling methodologies are mentioned in section 2.3 after which transition modeling is explored in section 2.4.

2.1. Cost Estimation: DNS, LES, and WMLES

To better appreciate the value of WMLES (and DES), a rough but instructive cost estimation is elaborated for DNS, LES and finally WMLES.

2.1.1. Estimating Cost of DNS by Dimensional Analysis

An approximate cost estimate of DNS in terms of the Reynolds number can be obtained from dimensional analysis and using Kolmogrov's hypotheses.

To perform DNS, a mesh resolution is required such that all the length scales of the flow can be represented and resolved i.e., from the integral to the dissipative scales or the so called Kolmogrov scales. Assuming that the DNS resolves a flow field of isotropic turbulence, the dominant dynamics in this flow are the processes occurring in the energy cascade i.e., (kinetic) energy transfer from the large-scale eddies to successfully smaller eddies and viscous dissipation by the smallest of such eddies. Indeed, following Kolmogrov's first similarity hypothesis, these two dominant dynamics can be uniquely determined by the dissipation rate ϵ, and the kinematic viscosity, ν. By dimensional analysis, the definition of the Kolmogrov length scale η, see eq. (2.1) is derived from the fact that $\eta \sim \nu\epsilon$.

$$\eta \equiv (\nu^3/\epsilon)^{1/4} \tag{2.1}$$

$$\epsilon \sim u_0^3/l_0 \tag{2.2}$$

By then observing that the kinetic energy of the largest eddies scales by u_0^2, results in eq. (2.2), where the subscript 0 denotes the integral scales. Finally, recall that the DNS mesh resolution must be able to represent the smallest scales. Considering a flow field of size l_0 requires that at least l_0/η grid points along each direction. Substituting eq. (2.1) and eq. (2.2) into l_0/η then gives the cost estimate of DNS in one dimension in terms of

$\mathscr{R}e$ shown in eq. (2.3). For three-dimensional space, the mesh resolution must then at least be in the order of $\mathscr{O}(\mathscr{R}e_0^{9/4})$.

$$l_0/\eta = \left(\frac{u_0 l_0}{\nu}\right)^{3/4} = \mathscr{R}e_0^{3/4} \qquad (2.3) \qquad T/\Delta t \sim \mathscr{O}(l_0/\eta) = \mathscr{O}(\mathscr{R}e_0^{3/4}) \qquad (2.4)$$

For numerical stability, the numerical simulation must advance with a timestep of Δt such that fluid motion moves a fraction of some grid spacing η and so $\Delta t \sim \mathscr{O}(\eta/u_0)$. Moreover, typically simulations are run for several integral time units for numerical accuracy so the total simulation time is $T \propto \mathscr{O}(l_0/u_0)$, resulting in the DNS time cost shown in eq. (2.4). Thus, the total DNS cost is $\mathscr{O}(\mathscr{R}e_0^3)$.

Assuming that an airfoil simulation at $\mathscr{R}e = 1000$ is performed in one second, a similar DNS performed at Reynolds numbers in the aeronautical range of $\mathscr{R}e = \mathscr{O}(10^6)$ implies a simulation time in the order of 1×10^9 s, which is roughly 30 years. Hence, it is obvious that the viability of DNS in transitional to high Reynolds number flows is still severely limited for the foreseeable future, especially in an industrious setting which is why the focus is set on LES which is computationally cheaper than DNS.

2.1.2. COST OF LARGE EDDY SIMULATION

LES has been the focus in the past several decades in academic turbulence research to analyse unsteady complex turbulent flows as it is much more viable due to lower cost scaling in $\mathscr{R}e$. However, why LES scales much better will be explored subsequently. As the cost derivation is not the main topic of this study, the cost of LES is concisely discussed. For a more detailed analysis, the reader is suggested to consult Choi and Moin (2012), Pope (2000), and Yang and Griffin (2021).

LARGE EDDY SIMULATION

The main idea of LES is to resolve the largest eddies (turbulence) that contain most of the energy in the flow, thereby reducing the restrictive mesh and temporal requirements of DNS. To achieve this, LES relies on the concept of scale separation by (low-pass) filtering the Navier-Stokes (NS) equations. The largest eddies are then resolved up to some cut-off length scale or wave number ξ_c, while the smaller length scales, or eddies beyond $|\xi| > \xi_c$ are modeled. The momentum equation for LES of incompressible flow is shown in eq. (2.5).

$$\frac{\partial \bar{u}_j}{\partial t} + \frac{\partial \overline{u}_i \overline{u}_j}{\partial x_i} - \nu \frac{\partial^2 \bar{u}_j}{\partial x_k^2} + \frac{1}{\rho}\frac{\partial \bar{p}}{\partial x_j} = -\frac{\partial \tau_{ij}}{\partial x_i} \qquad (2.5)$$

The filtered velocities ($\overline{u}_i$) are known, and so is the product of the filtered velocities ($\overline{u}_i \overline{u}_j$). However, the filtered product of the velocities ($\overline{u_i u_j}$) is not, which is where the modeling part of LES arises. For closure, the filtered product term is replaced by the filtered velocities term, plus the residual or sub-grid scale (SGS) stress tensor, τ_{ij}. The SGS stress tensor includes the effect of the unresolved scales onto the large-scale motions. Hence, successfully modeling the SGS stress tensor, allows for scale separation between the large and small scale structures of the flow. One of these types of SGS models, are the eddy-viscosity based models. For a detailed overview of the advancements made in SGS modeling, the reader is referred to Moser et al. (2021). Next, the cost of LES for two fundamental cases are discussed.

HOMOGENEOUS ISOTROPIC TURBULENCE

One application of LES is the simulation of homogeneous isotropic turbulence (HIT). As mentioned earlier, for isotropic flows, DNS scales roughly with $\mathcal{R}e^3$. However, for LES, the computational cost does not scale strongly with the Reynolds number. This can be clearly explained by considering the model energy spectrum shown in fig. 2.1 for various $\mathcal{R}e_\tau$. On the y-axis, the kinetic energy is displayed while the x-axis denotes the wave number, which can be seen as the various length scales of the flow. Low wave numbers denote large scales.

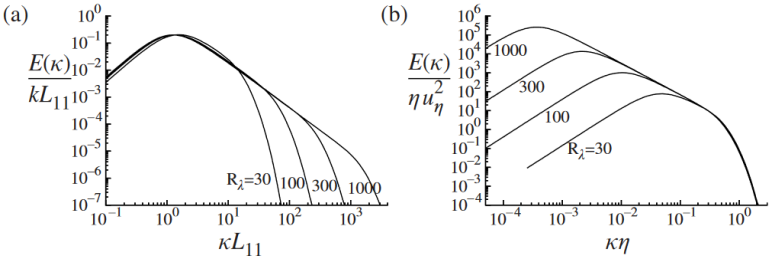

Figure 2.1: The model spectrum for various Reynolds numbers, scaled by (a) k (turbulent kinetic energy) and L_{11} (integral scale), and (b) Kolmogrov scales (Pope, 2000, p. 242).

Remark from fig. 2.1 that as the $\mathcal{R}e$ increases, the energy spectrum shows a clear linear regime between the largest energy-containing scales ($k \sim \mathcal{O}(L_{11})$) and the scales in the dissipative range ($k \sim \mathcal{O}(\eta)$). In particular, this linear range is described as the inertial range, which together with the dissipative range form the universal equilibrium range that satisfies the Kolmogrov's hypotheses of similarity and local isotropy. Indeed, as the name suggests, the scales within this range are universal in nature and a function of ϵ and ν. The takeaway from fig. 2.1 is that as the Reynolds number increases, separation of scales becomes increasingly clear and so does the justification of modeling the scales in the universal equilibrium range. Consequently, LES becomes increasingly attractive in terms of costs as the Reynolds number increases. Hughes et al. (2001) show that an LES of HIT performed at just $\mathcal{R}e_\tau = 90$ is already very close to the DNS solution with half of the mesh requirement.

Unfortunately, not all turbulent flows are isotropic and homogeneous in nature. Most of the turbulent flows are wall-bounded, where at least one "wall" is present e.g., flow over an aircraft. Such wall-bounded flows are inhomogeneous and so the weak scaling with Reynolds number does not (partially) apply to these type of flows.

WALL-BOUNDED FLOWS

Wall-bounded flows are complex and inhomogeneous, requiring a different analysis of the cost scaling with $\mathcal{R}e$. Consider a snapshot of a developing turbulent boundary layer shown in fig. 2.2. Remark that the length scales decrease as one moves closer to the wall. A clear scale of separation is enforced by the presence of the wall as a function of the wall-normal distance.

Consider a turbulent boundary layer of thickness δ, this boundary layer can be split into an inner and outer layer. The inner layer ($\approx 0.2\delta$) is the part of the boundary layer

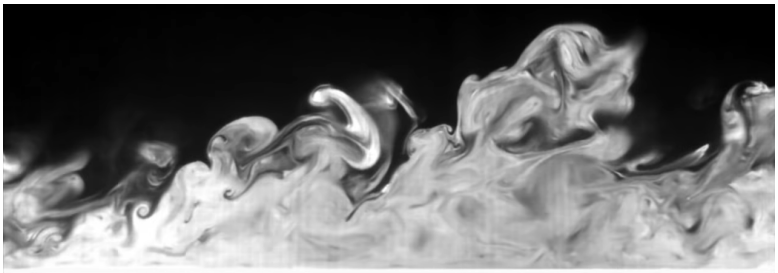

Figure 2.2: Frame from an imaging system capturing a developing turbulent boundary layer along a 5-meter long flat plate submerged and towed through water (J. H. Lee et al., 2012).

closest to the wall and is predominantly affected by the smaller, viscous length scales under the presence of this wall. The outer layer however, sits on top of this inner layer ($\delta > 0.2$), where viscous effects are negligible and is predominantly affected by the external flow beyond δ. Chapman (1979) approximated that the total cost (spatial and temporal resolution) for the outer layer only scales with $\mathscr{R}e^{0.53}$. However, the same does not hold for the inner layer, which scales with $\mathscr{R}e^{2.4}$. Over the years, these calculations have been revisited, among others by Choi and Moin (2012) and Yang and Griffin (2021). Yang and Griffin (2021) showed that the inner layer cost scales with $\mathscr{R}e^{2.72}$ and the outer layer with $\mathscr{R}e^{1.14}$, significantly higher than the original numbers from Chapman (1979), but slightly lower than the earlier improved estimations given by Choi and Moin (2012).

These cost estimations give a great reason to model the inner layer so that a significant cost reduction is achieved, thereby allowing higher Reynolds number simulations to be performed. In fact, the cost estimations given above are analogous to the cost of WRLES (inner layer) and WMLES (outer layer). Now that the cost of DNS, (WR)LES, and WMLES are briefly discussed, the question remains as to how wall-modeling in LES is achieved. Before elaborating on the methodologies used in existing wall models, a fundamental discussion on boundary layers is prerequisite.

2.2. BOUNDARY LAYER FLOWS

A discussion on the boundary layer dynamics is instructive for the subsequent part of this study to better appreciate the proposed wall-modeling approaches, but more importantly understand the reasons for the existing discrepancies in WMLES. Before discussing the boundary layer flows, some fundamentals are explained beforehand.

2.2.1. BOUNDARY LAYER CHARACTERISTICS

Consider a two-dimensional boundary layer flow over a flat plate. A freestream flow with velocity U_e moves over the flat plate, as a result the flat plate induces a drag force onto the flow, developing a shear area i.e., the boundary layer. As the boundary layer flow moves further downstream, the velocity decreases and so to satisfy conservation of mass, the sheared area must increase, deflecting the freestream flow away from the wall. At any distance x from the leading edge, the boundary layer exhibits a velocity profile as a function of the wall-norm distance, y with zero velocity at the wall, and some external

flow velocity U_e at the edge of the boundary layer.
The distance at which the boundary layer flow returns to 99% of the freestream velocity is defined as the boundary layer thickness (δ_{99}). Associated with this, is the displacement thickness (δ^*) which quantifies the amount of deflection experienced by the external flow by the shear layer.

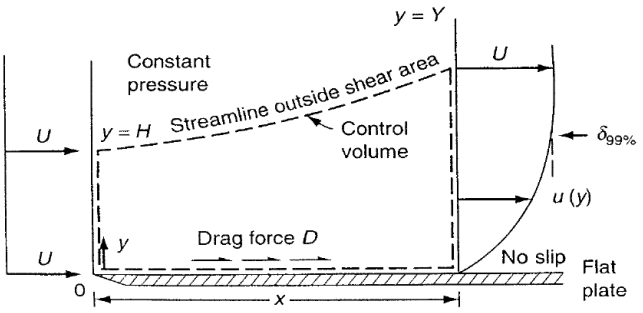

Figure 2.3: Definition of the control volume for the analysis of flow past a flat plate (White, 2006).

$$\delta^* = \int_0^{y\to\infty} \left(1 - \frac{u}{U_e}\right) dy \qquad (2.6) \qquad\qquad \theta = \int_0^{\delta} \frac{\rho u}{\rho_e U_e} \left(1 - \frac{u}{U_e}\right) dy \qquad (2.7)$$

By applying conservation of mass to the control volume, the definition of the displacement thickness is obtained which is given by eq. (2.6), where u is some velocity profile at station y, and U_e is the external flow velocity. This displacement thickness can be interpreted as the displacement of the streamlines in the external flow.

Another characterization of the boundary layer is the momentum thickness θ, which is obtained by applying conservation of momentum instead, shown in eq. (2.7), and is related to the drag of the surface. The ratio of these two parameters results in the shape factor, a non-dimensional parameter which indicates the stability of the velocity profile, where a low H implies a more stable boundary layer.

$$\tau_w = \mu \frac{\partial u}{\partial y}\Big|_{y=0} \qquad (2.8)$$

2.2.2. DERIVATION OF THE BOUNDARY LAYER EQUATIONS

Derivation of the boundary layer equations provides additional insight into their behavior. Several assumptions are made however to simplify the derivations. Namely, consider an incompressible flow at a high Reynolds number ($\mathscr{R}e \gg 1$). In the streamwise direction, flow convection dominates and so the scales can be defined by U_e, L, and $t = U_e/L$, where t is the transit time of the flow. In the transverse direction however, dissipation dominates and so similarly, the scales may be defined by ν and δ, where δ is again the boundary layer thickness. These two scales are related by the $\mathscr{R}e$ as shown in eqs. (2.9a) to (2.9c).

$$\delta = \sqrt{\nu t} = \sqrt{\nu L / U_e} = L \mathscr{R}e_L^{-0.5} \tag{2.9a}$$

$$v = \delta / t = \sqrt{\nu U_e / L} = U_e \mathscr{R}e_L^{-0.5} \tag{2.9b}$$

$$\delta / L = v / U = \mathscr{R}e_L^{-0.5} \tag{2.9c}$$

In other words, the transverse scales are much smaller than the convective scales when $\mathscr{R}e \gg 1$, combined with the integral plate analysis done previously, the following inequalities shown below hold.

$$\mathscr{R}e \gg 1: \quad \delta \ll x \qquad v \ll u \qquad \frac{\partial u}{\partial x} \ll \frac{\partial u}{\partial y} \qquad \frac{\partial v}{\partial x} \ll \frac{\partial v}{\partial y}$$

Now, consider the dimensional Navier-Stokes equations for incompressible flow shown in eqs. (2.10a) to (2.10c), by substituting the non-dimensional parameters shown in eq. (2.11), which are defined based on the obtained approximations previously, a non-dimensional form of the Navier-Stokes equations is obtained.

$$\frac{\partial u}{\partial x} + \frac{\partial v}{\partial y} = 0 \tag{2.10a}$$

$$\rho\left(\frac{\partial u}{\partial t} + u\frac{\partial u}{\partial x} + v\frac{\partial u}{\partial y}\right) = -\frac{\partial p}{\partial x} + \mu\left(\frac{\partial^2 u}{\partial x^2} + \frac{\partial^2 u}{\partial y^2}\right) \tag{2.10b}$$

$$\rho\left(\frac{\partial v}{\partial t} + u\frac{\partial v}{\partial x} + v\frac{\partial v}{\partial y}\right) = -\frac{\partial p}{\partial y} + \mu\left(\frac{\partial^2 v}{\partial x^2} + \frac{\partial^2 v}{\partial y^2}\right) \tag{2.10c}$$

$$\begin{aligned} x^* &= \frac{x}{L} \qquad y^* = \frac{y}{L}\sqrt{\mathscr{R}e} \qquad t^* = \frac{tU_e}{L} \\ u^* &= \frac{u}{U_e} \qquad v^* = \frac{v}{U_e}\sqrt{\mathscr{R}e} \qquad p^* = \frac{p - p_0}{\rho U_e^2} \end{aligned} \tag{2.11}$$

Remark that $\mathscr{R}e \gg 1$ and so terms containing $1/\mathscr{R}e$ can be omitted. As a result the streamwise diffusion term, and the transverse momentum equation reduce to a single term. The latter equation therefore implies a constant pressure in y i.e., the pressure in the boundary layer is equal to the external pressure (at the same x-position). Moreover, note that the form of the continuity equation remains the same, hence conservation of mass is independent of $\mathscr{R}e$. The dimensional form of eqs. (2.12a) to (2.12c) are the incompressible set of boundary layer equations originally developed by Blasius (1908).

$$\frac{\partial u^*}{\partial x^*} + \frac{\partial v^*}{\partial y^*} = 0 \tag{2.12a}$$

$$\frac{\partial u^*}{\partial t^*} + u^*\frac{\partial u^*}{\partial x^*} + v^*\frac{\partial u^*}{\partial y^*} = -\frac{\partial p^*}{\partial x^*} + \cancelto{0}{\left(\frac{1}{\mathscr{R}e}\cdot\frac{\partial^2 u^*}{\partial x^{*2}} + \frac{\partial^2 u^*}{\partial y^{*2}}\right)} \tag{2.12b}$$

$$\cancelto{0}{\frac{1}{\mathscr{R}e}\cdot\left(\frac{\partial v^*}{\partial t^*} + u^*\frac{\partial v^*}{\partial x^*} + v^*\frac{\partial v^*}{\partial y^*}\right)} = -\frac{\partial p^*}{\partial y^*} + \cancelto{0}{\frac{1}{\mathscr{R}e}\cdot\left(\frac{1}{\mathscr{R}e}\cdot\frac{\partial^2 v^*}{\partial x^{*2}} + \frac{\partial^2 v^*}{\partial y^{*2}}\right)} \tag{2.12c}$$

Note that stated equations have their limitations. Equations (2.12a) to (2.12c) can only be valid for incompressible flows where $\mathscr{R}e \gg 1$. Additional limitations include when separation occurs from a decelerating boundary layer. After this separation point, the derived equations become invalid. Another limitation applies to regions with laminar-to-turbulent transition.

2.2.3. SIMILARITY SOLUTIONS FOR LAMINAR BOUNDARY LAYER

Several solutions exist for obtaining the characteristics of laminar boundary layers. Most famously are the Blasius solution for flat plate flow and the Falkner-Skan equations. Both of these rely on the principle of similarity i.e., in the streamwise direction the shape of the velocity profile remains the same and hence independent of x, but the thickness grows and must be scaled based on the x-position. Before discussing the two similarity solutions, first the general similarity boundary layer equation is derived.

Let $\delta(x)$ be the scaling factor so that a scaled wall-normal coordinate is defined. Then, a scaled parameter for the velocity within the boundary layer can be written as eq. (2.13).

Subsequently, rewriting the stream function to introduce $f(\eta)$ in (ψ) such that $\psi = U_e(x)\delta(x)f(\eta)$ allows the velocity components to be written as eq. (2.14) and eq. (2.15). Then, by substituting the expressions for the velocities into the incompressible boundary layer equations shown in eq. (2.16), the general self-similar boundary layer is obtained, see eq. (2.17a), where eq. (2.17b) are the associated boundary conditions.

$$\frac{u(x,y)}{U_e(x)} = f(\eta), \text{ where } \eta = y/\delta(x) \tag{2.13}$$

$$\frac{\partial \psi}{\partial y} = u = U_e(x)f'(\eta) \tag{2.14}$$

$$-\frac{\partial \psi}{\partial x} = v = -\frac{dU_e(x)\delta}{dx}f'(\eta) + U_e(x)\frac{d\delta}{dx}\eta f'(\eta) \tag{2.15}$$

$$\begin{aligned} &\frac{\partial u}{\partial x} + \frac{\partial v}{\partial y} = 0 \\ &u\frac{\partial u}{\partial x} + v\frac{\partial u}{\partial y} = -U_e\frac{dU_e}{dx} + \nu\frac{\partial^2 u}{\partial y^2} \end{aligned} \tag{2.16}$$

$$f''' + \left[\frac{\delta}{\nu}\frac{du_e\delta}{dx}\right] ff'' + \left[\frac{\delta^2}{\nu}\frac{du_e}{dx}\right]\left(1 - f'^2\right) = 0 \tag{2.17a}$$

$$f'(0) = f(0) = 0 \quad f'(\infty) = 1 \tag{2.17b}$$

Subsequently, two forms derived from this self-similar solution are discussed i.e., the Blasius and the Falkner-Skan equations.

BLASIUS FLAT PLATE FLOW SOLUTION

Blasius derived a simple self-similar solution for laminar boundary layer flow over a flat plate by assuming that the external velocity remains constant i.e., $U_e(x) = \text{cst}$ and employing the scaling factor in eq. (2.18). Since, U_e is constant, eq. (2.17a) can be simplified to the problem shown in eq. (2.19).

$$\delta = \sqrt{2\frac{\nu x}{U_e}} \tag{2.18}$$

$$f(\eta)''' + ff'' = 0 \tag{2.19}$$

The Blasius equation is shown to be accurate for laminar boundary layers, as long as $\mathscr{R}e > 1000$ (White, 2006). For lower Reynolds numbers, Blasius underestimates the skin friction. Moreover, the applicability of Blasius is limited to a flat plate geometry and the additional requirement that $U_e = \text{cst}$ aggravates this limitation further. A more general self-similar solution is therefore desired that is applicable to a wider variety of geometries and flows.

FALKNER-SKAN SOLUTION

The Falkner-Skan equation is a self-similar boundary layer problem that is more general and able to express a wider range of laminar boundary layers and is obtained by choosing U_e as eq. (2.20), and η as eq. (2.21), where m is a chosen parameter so that the problem is self-similar. Substituting these into eq. (2.16), results in eq. (2.22).

$$U_e(x) = Kx^m \tag{2.20}$$

$$\eta = \frac{y}{x}\sqrt{\frac{m+1}{2}\frac{U_e x}{\nu}} \tag{2.21}$$

$$f''' + ff'' + \beta(1 - f'^2) = 0, \quad \beta = \frac{2m}{1+m} \tag{2.22}$$

Note that eq. (2.20) gives a power-law relation and therefore m dictates the acceleration (or deceleration) of the external flow. Consequently, this also dictates the streamwise pressure gradient as shown by eqs. (2.12a) to (2.12c) and hence $m < 0$ indicates decelerated flows ($\frac{dp}{dx} > 0$), and accelerated ($\frac{dp}{dx} < 0$) when $m > 0$. Moreover, the value of m (or β) also has a geometrical interpretation. In particular, the Falkner-Skan equation considers the (inviscid) solution for flows past wedges and corners with a half-wedge angle β. The family of Falkner-Skan solutions are shown in fig. 2.4a and fig. 2.4b.

The effect of β on the shape of the velocity profile is evident, a boundary layer experiencing an adverse pressure gradient shows a velocity profile with an inflexion point such that an S-shaped velocity profile is created. For favorable pressure gradients, the velocity profile quickly reaches the local external flow velocity, where the highest acceleration occurs very close to the wall. Finally, a zero-pressure gradient laminar boundary layer exhibits a linear velocity profile near the walls with deceleration occurring further away. Evaluating eq. (2.10b) at the wall ($u = v = 0$), gives the following relation:

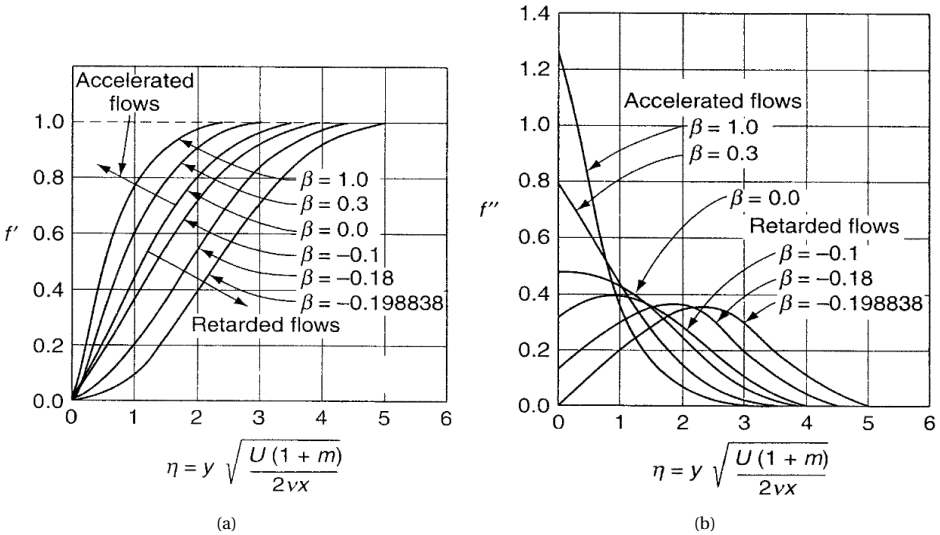

Figure 2.4: (a) Velocity profile, (b) shear-stress profiles for various β angles (White, 2006).

$$\left.\frac{\partial^2 u}{\partial y^2}\right|_{y=0} = \frac{1}{\mu}\frac{dp}{dx} \tag{2.23}$$

Equation (2.23) shows the relation between the experienced pressure gradient and the curvature of the velocity profile at the wall. As mentioned earlier, the velocity profile is an indicator of the stability against separation. Indeed, the curvature of the velocity profile indicates whether separation is possible. Under an adverse pressure gradient, the boundary layer is decelerated, leading to backflow and separation in the boundary layer downstream. This process is depicted in fig. 2.5. Note that separation cannot occur in favorable gradients as the flow is accelerated downstream. Similarly for a boundary layer in zero pressure gradient, as long as a zero gradient is maintained, no separation can occur.

The two most popular similarity solutions for laminar boundary layers are described above. However, due to the assumptions made in these self-similar solutions, the applicability is limited. As noted earlier self-similarity requires that the velocity profile follow some defined profile in the streamwise direction. In practice, this is most likely not the case as the pressure gradient imposed by the outer flow changes e.g., from a favorable to an adverse pressure gradient. Thus, solutions to laminar boundary layers which do not rely on similarity are discussed subsequently.

2.2.4. NON-SIMILAR SOLUTION FOR LAMINAR BOUNDARY LAYER

Non-similar solutions provide a more generalized (set of) equation(s) to characterize laminar boundary layers. Many approaches have been proposed in the last century and can be classified into three general methodologies as shown by Rosenhead (1963). One

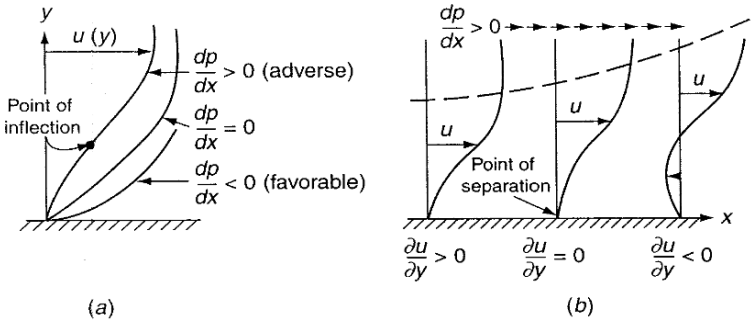

Figure 2.5: Pressure gradient-induced geometric influences: (a) types of profile; (b) persistent adverse gradient (White, 2006, p. 229).

obvious choice is to assume that the velocity profile can be approximated by a polynomial by means of series expansion. Such methods were introduced by Von Kármán in 1921(White, 2006) and in significantly refined form by Pohlhausen (1921). Many integral boundary layer methods exist and are extensively discussed and compared in Rosenhead (1963).

The method of Pohlhausen (VKP) assumes that the velocity profile satisfies a quartic polynomial whose profile is dictated by the continuity boundary conditions at the edge of the boundary layer and wall. Thwaites however, based his method on correlation using existing experimental data instead. Another approach is to use CFD, where the continuity and momentum equations are numerically solved to obtain the velocity profiles. How to numerically solve the laminar boundary layer equations is beyond the scope of this literature study. Many integral and series expansion methods have been proposed to characterize the laminar boundary layer but only the two most popular methods of Kármán-Pohlhausen and Thwaites are discussed in the present literature study.

VON KÁRMÁN-POHLHAUSEN METHOD

Von Kármán first introduced the integrated momentum equation to analyse boundary layers and hence the equation is also referred to as the Kármán integral relation. This integral relation is obtained by multiplying eq. (2.10a) with $(u - U_e)$ and subsequently subtracting it from eq. (2.10c) (White, 2006).

$$-\frac{\partial \tau}{\partial y} = \frac{\partial}{\partial t}\rho(U_e - u) + \frac{\partial}{\partial x}(\rho u(U_e - u)) + \rho(U_e - u)\frac{dU_e}{dx} + \frac{\partial}{\partial y}(\rho v(U_e - u)) \tag{2.24}$$

Then by integrating eq. (2.24), the Kármán integral relation is obtained. A more compact form of this expression is achieved by substituting in the definitions of the displacement eq. (2.6), and momentum thickness eq. (2.7), resulting in eq. (2.25), where v_w is the wall-normal velocity.

$$\frac{\tau_w}{\rho U_e^2} = \frac{C_f}{2} = \frac{1}{U_e}\frac{\partial}{\partial t}(U_e\delta^*) + \frac{\partial \theta}{\partial x} + (2\theta + H)\frac{\theta}{U_e}\frac{dU_e}{dx} - \frac{v_w}{U_e} \tag{2.25}$$

Using eq. (2.24), Pohlhausen (1921) developed an approximate method to characterize laminar boundary layers and obtain the parameters of interest (e.g. τ_w, H) by assuming that the laminar velocity profiles are described by a quartic polynomial. Equation (2.26) is formulated such that all expressivity is contained in a single parameter Λ, referred to as the Pohlhausen parameter, which couples the approximated velocity profile with the local external pressure gradient. Remark that the assumed quartic polynomial form is a linear combination of the expression for the Blasius profile and an expression to model the effect of the pressure gradient. for the elaborate discussion of the derivation and numerical procedure of the VKP method, the reader is referred to Rosenhead (1963) and White (2006), respectively.

$$f(\eta) = u/U_e = 2\eta - 2\eta^3 + \eta^4 + \frac{\Lambda}{6}[\eta(1-\eta)^3], \quad \Lambda = -\frac{\delta^2}{\eta}\frac{dU_e}{dx} \tag{2.26}$$

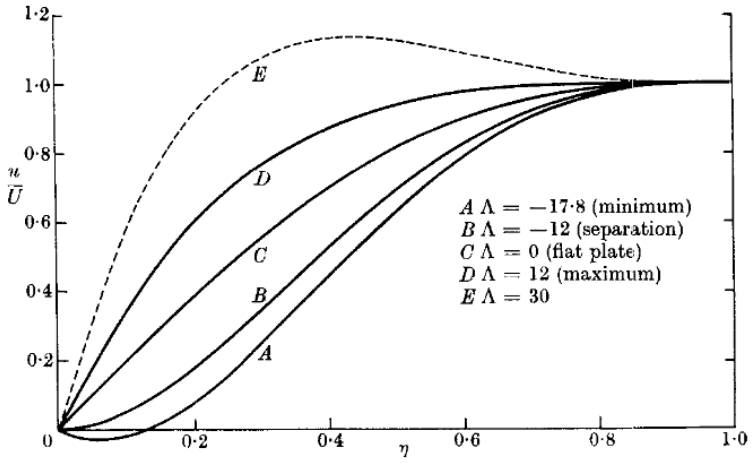

Figure 2.6: Velocity profiles of the VKP method for various Λ (Rosenhead, 1963, p. 295).

Several limitations must be considered with the VKP method. Figure 2.6 shows that for $\Lambda > 12$, the predicted velocity profile becomes unphysical. Indeed, the peak velocity inside the boundary layer becomes larger than the local external flow velocity. Moreover, it is found that $\lambda > -12$ implies flow separation which is beyond the region of applicability of this method. Nevertheless, due to the simplicity of the velocity profile and requiring only the additional knowledge of Λ, the profile assumption approach has been for long considered the most widely used approximate method. Several others have extended the VKP method (Rosenhead, 1963), but Thwaites (1949) instead investigated an approach based on correlation i.e., approximating laminar boundary layer profiles by a universal function based on analytical and experimental data.

THWAITES' METHOD

Thwaites (1949) based his model on a momentum-integral relation where eq. (2.25) is multiplied by $U_e\theta/\nu$, resulting in eq. (2.27) (White, 2006). This makes both sides of the

equation to be related by a single parameter, λ defined in eq. (2.28). In particular, two non-dimensional correlation parameters are defined based on the shear (LHS term) and the shape factor as shown in eq. (2.29).

$$\frac{\tau_w \theta}{\mu U_e} = \frac{U_e \theta}{\nu}\frac{d\theta}{dx} + \frac{\theta^2 u}{\nu}(2+H) \qquad (2.27)$$

$$\lambda = \frac{\theta U_e}{\nu} = \left(\frac{\theta}{\delta}\right)^2 \Lambda \qquad (2.28)$$

$$\begin{aligned} \frac{\tau_w \theta}{\mu U_e} &\approx S(\lambda) \\ H = \frac{\delta^*}{\theta} &\approx H(\lambda) \end{aligned} \qquad (2.29)$$

$$U_e \frac{d}{dx}\left(\frac{\lambda}{u}\right) \approx 2\Big[S(\lambda) - \lambda(2+H)\Big] = F(\lambda) \qquad (2.30)$$

By eq. (2.29) and eq. (2.27), the integral-momentum relation can be written in the simplified form of eq. (2.30). Thwaites (1949) subsequently used this form to obtain a function that is able to approximate the laminar boundary layer profile. However, he did not base this on the assumption that these profiles can be approximated by "a family of parametric function", rather he proposed to fit a simple single parameter equation to a large collection of analytical and experimental data. His result is a linear function shown in eq. (2.31), which is integrated to obtain θ and eq. (2.28) to acquire τ_w and H (and all other parameters of interest). In practice, the shear and shape factor correlation are either obtained from tabulated values or a convenient curve fit, which is found in either Thwaites (1949) or White (2006). In the former, the coefficients of the linear function are found to be $a \approx 0.45$ and $b \approx 0.6$. Generally, $x_0 = 0$ in eq. (2.32) since a laminar boundary layer develops from the stagnation point.

$$F(\lambda) = a - b\lambda \qquad (2.31)$$

$$\theta = \frac{a\nu}{U_e^b}\int_{x_0}^{x} U_e^{b-1}\, dx \qquad (2.32)$$

Thwaites' method has shown an even simpler approach to approximate laminar boundary layers without assuming a parametric shape which was common in earlier works. In fact, the method only requires the knowledge and capability of integrating $U_e(x)$.

In his extensive comparison between integral methods, Rosenhead (1963) notes that the accuracy of each method in engineering application do not differ significantly and instead one should choose the method based on labor. White (2006) further shows by application of various approximate methods on the case of laminar flow past a circular cylinder, that knowing the true $U_e(x)$ is most critical for the accuracy of all approximate laminar boundary layer methods, rather than the accuracy of the method.

As mentioned before, the boundary layer equations derived earlier do not hold in regions of transition and separation. Hence, the next section aims to answer what mechanisms occur during boundary layer transition and what models are available.

2.2.5. LAMINAR-TO-TURBULENT TRANSITION

In engineering applications, a laminar boundary layer is preferred as it generates up to 90% less skin friction drag compared to a turbulent boundary layer. In particular, for typical airliners in cruise flight, the boundary layer over the body and wing are mostly tur-

bulent, resulting that skin friction drag comprises roughly 50% of the total drag. Hence, knowledge to delay flow separation and controlling wall-bounded flows is of great economical and environmental importance. This chapter serves only to summarize and discuss the required background to develop this report in the subsequent chapters. Therefore, only the possible transition modes and characteristics are discussed in this section.

There are numerous paths in which laminar flow transitions into turbulence. In literature, the paths to turbulence are summarized and extensively discussed in Herbert (1984) and Zaki and Durbin (2021). In general, three types of transition can be identified: natural, forced, and separated flow transition. Natural transition occurs under small external disturbances which cause the development of Tollmien-Schlichting (TS) waves, which is the primary mode of transition (Herbert, 1984). TS waves can be described as vortices moving in the spanwise direction relative to the dominant flow direction. These TS waves increase in size, become non-uniform due to external perturbations, and consequently introduce $\lambda-$, or hairpin vortices. These λ vortices then perturb the TS waves further and form the secondary instabilities. In transition literature, two types of secondary instabilities are distinguished based on whether these hairpin vortices are staggered (H-type transition) or aligned (K-type transition) (Panton, 2013, p. 756-759). Further downstream, these three-dimensional TS waves grow even faster and within a short distance, an intermittent process occurs where the TS waves locally breakdown and form turbulent spots (Panton, 2013). As these turbulent spots become larger and coalesce, transition to full turbulence is achieved. A schematic overview of the natural transition process is shown in fig. 2.7.

Bypass transition, on the other hand is initiated due to large-amplitude external perturbations e.g., freestream turbulence, or surface roughness, in turn these introduce long streamwise streaks in the boundary layer which, under perturbation of secondary instabilities, and turbulent spots, transitions to turbulence.
Lastly, transition can also simply occur under a (strong) adverse pressure gradient. An example, is the process in the formation of a laminar separation bubble, where a laminar boundary layer detaches under an adverse pressure gradient and forms a recirculation region i.e., the separation bubble. Above the bubble, the laminar flow transitions to turbulence, re-energizes the boundary flow and consequently re-attaches downstream, closing the laminar separation bubble.

In a subsequent chapter, transition models in CFD with the focus on RANS and LES applicable models are discussed. However, prior to discussing these models, fundamentals on turbulent boundary layers are elaborated to complete the current discussion of boundary layer flows.

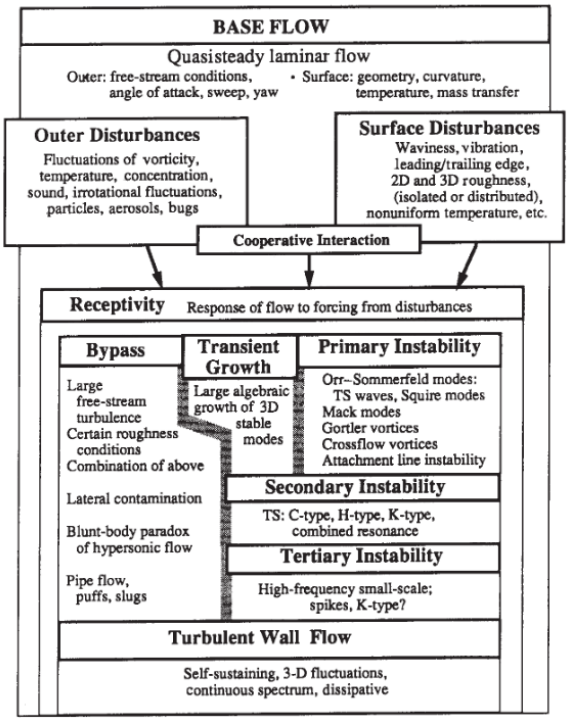

Figure 2.7: Morkovin map of the roads to turbulence (Panton, 2013, p. 757).

2.2.6. TURBULENT BOUNDARY LAYER

The dynamics within turbulent boundary layers are more complex than those under a laminar boundary layer and as such are divided into two parts. An outer layer is defined from the edge of the boundary, which comprises around 80% of the boundary layer thickness. This regime is predominantly affected by the external flow with diminishing strength as one moves closer to the wall. The dynamics in the outer layer are not universal due to the influence of the freestream flow. Moving closer to the wall, the effect of the external flow diminishes and instead, the presence of the wall dominates the flow behavior in this region and is referred to as the inner layer. In contrast, the inner layer is universal in nature compared to the dynamics in the outer layer, which makes modeling the inner layer an attractive alternative to resolving it.

Within these two layers, several sub-layers can be identified. The extent of these regions is usually expressed in y^+, a non-dimensional measure for the distance from the wall and is given by eq. (2.33), where ν is the kinematic viscosity and u_τ the friction velocity defined by eq. (2.34). Here, τ_w is the wall-shear stress and ρ the local fluid density. For far-away regions in the outer layer, the outer-scaling y/δ is used, where δ is the boundary layer height.

$$y^+ = \frac{u_\tau y}{\nu} \tag{2.33}$$

$$u_\tau = \sqrt{\frac{\tau_w}{\rho}} \tag{2.34}$$

Starting from the wall, the first sub-layer in the inner layer is the so-called viscous sub-layer ($y^+ < 5$), where the mean fluid velocity increases linearly with wall-normal distance. Above the sub-layer is the log layer whose name stems from the fact that the velocity profile is universally described by a logarithmic equation shown in eq. (2.35), where κ and B are constants. This log layer starts around $y^+ = 30$ and extends up to $y^+ : \mathcal{O}(10^3)$. As discussed earlier, separation of scales becomes more pronounced as the Reynolds number increases and so the log layer covers a larger extent of the boundary layer.

$$u^+ = \frac{1}{\kappa} \ln y^+ + B, \quad u^+ = \frac{u}{u_\tau} \tag{2.35}$$

Between the log layer and the viscous sub-layer is a transition region ($5 < y^+ < 30$), where the viscous and inertial stresses are roughly equal in magnitude and so is difficult to accurately model. Similarly, between the inner layer (significant viscous effects) and outer layer (negligible viscous effects) is also a transition layer called the buffer layer. At the edge of the boundary layer lies the velocity defect region that extends from the log layer to δ, this region is predominantly affected by the external flow and is therefore not universal. The typical shape of the velocity profile of a high $\mathcal{R}e$ boundary layer is shown in fig. 2.8.

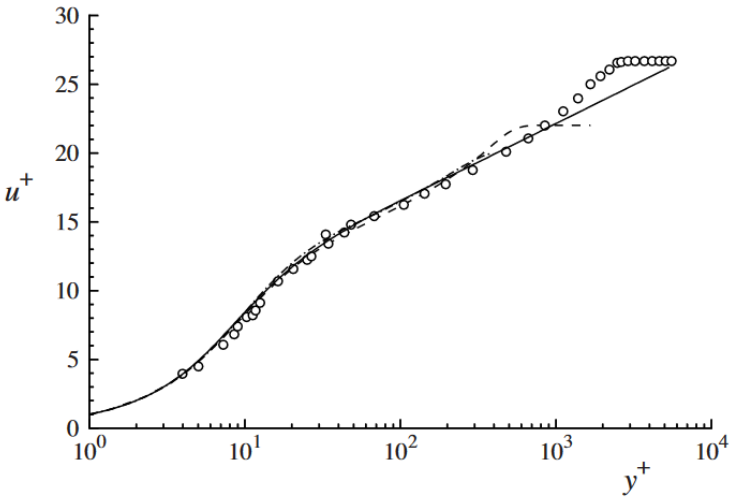

Figure 2.8: Mean streamwise velocity profiles in wall units for wall-bounded flows at various Reynolds numbers (Pope, 2000, p. 303): circles, boundary layer experiments of Klebanoff (1954); dashed line, boundary layer DNS of Spalart (1988), $\mathcal{R}e_\theta = 1410$; dot-dashed line, channel flow DNS of Kim et al. (1987), $\mathcal{R}e = 13750$; solid line van Driest's law of the wall (Van Driest, 1956).

A turbulent boundary layer can also be described by the equations derived earlier in eqs. (2.12a) to (2.12c) which show that the average wall-parallel velocities must satisfy eq. (2.36), and can be seen as an unsteady Reynolds-averaged Navier Stokes (URANS) description of the boundary layer flow. On the left-hand side, the dynamics due to un-

steadiness, convection and pressure gradient are described and combined must equal the total stress in the boundary layer. ν_t is the eddy-viscosity which models the Reynolds stresses from the unresolved scales.

$$\frac{\partial u_i}{\partial t} + \frac{\partial u_i u_j}{\partial x_j} + \frac{1}{\rho}\frac{\partial p}{\partial x_i} = \frac{\partial}{\partial y}\left[(\nu + \nu_t)\frac{\partial u_i}{\partial y}\right], \quad i = 1,3 \tag{2.36}$$

In case it is assumed that the boundary layer is in steady-state i.e., the convective term is balanced out by the pressure gradient, eq. (2.36) can be simplified to eq. (2.37), which is the familiar law of the wall. In this case, a RANS formulation of the turbulent boundary layer is solved.

$$\frac{\partial}{\partial y}\left[(\nu + \nu_t)\frac{\partial u_i}{\partial y}\right] = 0 \tag{2.37}$$

At the start of this literature study, the cost benefit of WMLES over DNS and LES was discussed to understand why WMLES is needed. In this chapter, the fundamentals of boundary layers are discussed as a background before going over the different wall models and the underlying methodologies which will therefore be discussed subsequently.

2.3. TYPES OF WALL-MODELING IN LES

As mentioned earlier, the necessity of wall models are two folds. Firstly, the mesh requirement for wall-bounded flows scales significantly with $\mathscr{R}e$ and hence is too costly to be solved with current computing power. Secondly, current viable mesh sizes are underresolved in the near-wall regions and hence unable to retrieve the right amount of wall-shear stress. Indeed, the goal of wall models in LES is to apply sufficient wall-shear stress to the LES region.
An overview of wall models is given below. First, the "conventional" wall models are discussed which have been proposed in the early stages of WMLES. Afterwards, more recently proposed wall models are addressed.

2.3.1. HYBRID LES/RANS WALL MODEL

One of the more versatile type of wall models employs a zonal approach to predict the wall shear stress in the inner layer. In the hybrid LES/RANS approach, the computational domain is split between a near-wall RANS region with height h_{wm} and a LES region above this RANS domain, hence it is often referred to as a zonal approach as a distinct interface is created between the two methods. Note that this means that the LES region is prescribed up to some distance above the wall. Moreover, a separate grid is employed in the RANS region to solve the inner (boundary) layer flow.

Versions of the hybrid LES/RANS approach are distinguished by how h_{wm} is set. If the wall model height is fixed, then the approach is referred to as a zonal approach (Nikitin et al., 2000). When h_{wm} is set by the grid or solution, the approach is referred to as a "seamless" approach (Baurle et al., 2003).

An issue with the hybrid LES/RANS approach is the difference in computed quantities in the LES and RANS region i.e., LES feeds in instantaneous variables, while RANS is only able to output the time-averaged wall-shear stress to the LES region. In prac-

tice, this results in a phenomenon called log-layer mismatch, where in most cases, a positive bias in the mean velocity profile is found. Several solutions exist to combat or completely eliminate log-layer mismatch. These include adding artificial perturbations around the interface (Piomelli et al., 2003), or improving the blending function between the estimated eddy-viscosities (Shur et al., 2008).

Nevertheless, the hybrid LES/RANS approach also provides benefits in terms of flexibility. Since the RANS region can be prescribed by h_{wm}, the height may be adjusted to run in DES or in full RANS mode which allows the same CFD code to be used for variety of design purposes.

2.3.2. RANS-LIKE WALL MODEL

Another standard approach for wall-modeling in LES is using a wall-stress model which solves the momentum equation in the wall-parallel direction i.e., eq. (2.36), repeated here for convenience. In this method, a probing point is defined at some height h_{wm} to be used as input for the wall model. Compared to the hybrid LES/RANS approach, a subtle difference is that the LES region is defined up to the wall. Note that the equations here solve for the averaged wall-parallel quantities. Finally, an assumption of eq. (2.36), is that a dominant external streamwise flow direction is present. As mentioned earlier, if the inner layer is assumed to be in equilibrium, the LHS becomes zero and the wall model is simplified to follow the famous log-law which can either be solved numerically or algebraically. Since the latter is the cheapest computationally, it is also the most common wall-stress modeling approach. One advantage of numerically solving the log-law is so that other flow physics can be taken into account in the implementation of the wall model (Bose & Park, 2018).

$$\frac{\partial u_i}{\partial t} + \frac{\partial u_i u_j}{\partial x_j} + \frac{1}{\rho}\frac{\partial p}{\partial x_i} = \frac{\partial}{\partial y}\left[(\nu + \nu_t)\frac{\partial u_i}{\partial y}\right], \quad i = 1,3$$

Unfortunately, the equilibrium assumption rarely holds since it requires that the convective term and pressure gradient to even out. In fact, an equilibrium wall-stress model (EQWM) performs poorly in regions with large three-dimensionality, such as juncture, and separated flows (Goc et al., 2021; Lozano-Durán et al., 2020; Tamaki et al., 2019). Still, while the equilibrium condition is not satisfied in most cases, the EQWM performs adequately well under non-equilibrium conditions. Several explanations are given by Larsson et al. (2016). First, the outer layer (>80%) should be well-resolved in WMLES and hence most of the non-equilibrium effects should already be captured. Secondly, the inner layer turbulent dynamics are much faster than the dynamics in the outer layer, as such the inner layer should be close to steady-state in non-equilibrium flows. Finally, note that the LHS of eq. (2.36) describes various processes that includes the unsteadiness, convection, and pressure gradient of the flow. These individual terms are large in magnitude but should balance each other out above the viscous layer ($y^+ > 5$) (Hickel et al., 2012).

When equilibrium is not assumed and all LHS terms are included, a non-equilibrium wall-stress (NEQWM) model is solved. If the accuracy of NEQWM is necessary for engineering applications, Hickel et al. (2012) argue that one should at most include the normal derivatives to reduce excessive additional computational cost.

The issue of log-layer mismatch also occurs in the wall-stress modeling approach, but is much more easily resolved. In the past, it was common to have $\Delta h \approx h_{wm}$ and set the probing point at this first cell from the wall. However, to resolve the energetic scales at h_{wm} the mesh resolution must be sufficiently fine, and therefore having merely one cell between the probing point and the wall may not be adequate. Indeed, Kawai and Larsson (2012) show that to reduce or even eliminate log-layer mismatch, grid refinement must be employed. Kawai and Larsson (2012) found convergence for $\Delta y \leq 0.33 h_{wm}$. Similarly, J. Lee et al. (2013) reported $\Delta y \leq 0.3 h_{wm}$. A common rule of thumb is to have at least three to four cells between the probing point and the wall.

Together with the hybrid LES/RANS approach, wall-stress models are the most commonly implemented wall models. Comparing the two approaches, wall-stress EQWM are computationally cheaper while the implementation is also more straightforward. This is especially true for algebraic EQWM. Moreover, log-layer mismatch is also less of an issue for wall-stress based models. On the other hand, the hybrid LES/RANS allows for the most flexibility. Allowing users to either solve in RANS, DES, or WMLES mode. Both approaches assume a dominant streamwise direction which is not always true and certain non-equilibrium flows still pose a problem in terms of cost and accuracy.

2.3.3. INTEGRAL WALL MODEL

Wall-stress models perform well under equilibrium and relatively well for most non-equilibrium flows. However, the inaccuracies lie in the assumptions of the wall-stress formulation i.e., it assumes a dominant streamwise flow direction. Therefore, a wall-modeling approach that has similar cost, but increased accuracy in non-equilibrium conditions is desired.

Yang et al. (2015) proposed a wall-modeling formulation by vertical integration of the boundary layer equations based on the integral analysis of amongst others, Von Kármán and Pohlhausen discussed in section 2.2.4. Yang et al. (2015) named this approach, iWMLES (integral wall-modeled LES). Similarly to the VKP approach for laminar boundary layers, Yang et al. (2015) assumed a velocity profile and determined several parameters from the boundary conditions. Since the wall model formulation is based on eq. (2.36), non-equilibrium effects such as a pressure gradient is also taken into account.

Additionally, it is also possible to add the effect of wall roughness. iWMLES is advantageous as it is an algebraic method and does not require wall-normal refinement since a velocity profile is assumed. Furthermore, iWMLES is able to approximate the full non-equilibrium boundary layer equations all while retaining similar computational cost of an EQWM.

Yang et al. (2015) have shown improved performance over an EQWM in the wall-mounted cubes test case. Later on, Catchirayer et al. (2018) also performed adiabatic and isothermal quasi- incompressible channel flow simulations and compared iWMLES with an algebraic EQWM. Their results show that the performance iWMLES is on par with algebraic EQWM. Nevertheless, additional testing must be performed to cases with complex geometries for engineering applications.

2.3.4. DYNAMIC SLIP WALL MODEL

A novel approach was proposed by Bose and Moin (2014), who rather than applying a slip wall condition (applied wall-shear stress at the wall), prescribed a Robin condition, allowing mass to flow through the walls (transpiration). A dynamic procedure then computes the appropriate local slip length to predict the right amount of wall-shear stress. The benefits of this dynamic slip wall method (DSWM) are two-folds: no assumptions are made on the state of the boundary layer, which means it is applicable in both equilibrium and non-equilibrium flows, and theoretically in laminar boundary layers. Additionally, DSWM does not require any tuning parameters i.e., no empirical coefficients are needed compared to RANS-like and hybrid LES/RANS approaches. For an extensive explanation on the methodology, the reader is referred to the original paper.

Later on, Bae et al. (2019) extended this wall model by assessing the robustness of the DSWM by varying the Reynolds number, grid size, and used SGS model. While, Bose and Moin (2014) computed the slip length using a least-square fit on a modified form of Germano's identity, Bae et al. (2019) proposed a new framework for DSWM, referred to as the wall-stress invariant model (WSIM). In this model, a new dynamic procedure to compute the slip length is presented which is optimized to achieve a slip length such that the mean wall stress (with a slip boundary condition) approximates DNS accuracy. A key role in the performance of WSIM is enforcing a mean zero mass flow through the walls, while computing the appropriate slip length and filter size.

Test cases performed by Bae et al. (2019) include both (steady) turbulent and transient channel flow, and a zero-pressure gradient turbulent flat plate. The results from turbulent channel flow show the same order of discrepancy as an EQWM. However, the error shows a significant increase for higher Reynolds numbers, much larger than for the EQWM. Bae et al. (2019) notes that the better performance of EQWM is not surprising since the model assumptions are satisfied. Moreover, the larger error is ascribed to the incompatibility of larger filter sizes with the dynamic slip length procedure (a smaller filter size is needed for higher $\mathscr{R}e$). Nevertheless, the results are much better than without a model and the performance of WSIM matches those of EQWM.

Further validation on this method is performed by Whitmore et al. (2021), where flow over a Gaussian bump is simulated. Compared to an EQWM, the results of the WSIM show monotonic convergence for both the C_f as well as the C_p profiles in contrast to the EQWM results while offering approximately the same accuracy.

The above description of WSIM or DWSM sounds promising as the wall model is free of any tuning or empirical coefficients, and is furthermore applicable under non-equilibrium flows, all while having similar costs to an EQWM. However, the viability of the wall model is limited due to the lack of robustness in the calculation of the local slip lengths and sensitivity regarding the choice of SGS model.

2.3.5. MACHINE LEARNING BASED WALL MODEL

In the past years, machine learning has become a popular method to acquire a deeper understanding to long-standing problems. Yang et al. (2019) was one of the first to introduce machine learning to wall-modeling. Using a supervised learning approach which takes as input the wall-parallel velocity at h_{wm}, the grid aspect ratio, and the crossflow pressure gradient and outputs the local wall-shear stress. Using only DNS data of chan-

nel flow at $\mathscr{R}e_\tau = 1000$, the model shows better performance compared to equilibrium and non-equilibrium wall-models at greater Reynolds numbers.

Lozano-Durán and Bae (2020) took a step further and proposed a neural network using supervised learning and data from "canonical" test cases. The assumption used is that any flow behavior occurring in nature can be represented by a set of canonical flow units. In their paper, three flow units: boundary layer with separation bubble via blowing and suction, turbulent duct flow, and turbulent channel flow at various $\mathscr{R}e$ and aspect ratios are used to predict the wall-shear stress, and other flow information. These include for example the confidence of the predicted output and the composition of the simulated flow in terms of the flow units. Subsequently, the model is applied to the NASA juncture flow case and has shown to outperform the algebraic EQWM at a location experiencing near-zero-pressure gradient flow and locations with large flow three-dimensionality and separation. While the model is promising, Lozano-Durán and Bae (2020) warns the reader of applying such a model to other applications since only limited validation is performed.

Indeed, the big issue is that such neural networks require DNS data of the aforementioned flow units at various $\mathscr{R}e$ and as always machine learning-based approaches must be used with caution since the predictions are based on the training data and ultimately can produce erroneous predictions if the flow case cannot be reproduced by the training data. It goes without saying that more research and testing must be performed on combining machine-learning and wall-modeling.

At this point, all the wall models discussed are meant for modeling turbulent boundary layers and perhaps the reader may wonder if there are also wall models for the laminar part of the boundary layer. Moreover, when modeling laminar and turbulent boundary layers, transition must occur inbetween these parts, therefore another question may be whether transition models in LES also exist. Indeed, the latter is discussed in section 2.4 and the former models are discussed subsequently.

2.3.6. SELF-SIMILARITY BASED WALL MODEL

From the infancy of WMLES, attention was solely spent on modeling turbulent boundary layers. However, recently the WMLES community realized that predicting the wall-shear stress at the laminar part of the boundary layer can have a significant impact on the downstream flow (Gonzalez et al., 2020). Moreover, since laminar boundary layers are even thinner than their turbulent counterpart, the associated grid requirement is even more stringent and thus further necessitates the need for laminar wall-modeling.

While several laminar boundary layer approximations exist, some of them discussed in section 2.2, Gonzalez et al. (2020) approached this problem by employing the Falkner-Skan similary solution. The laminar part of the boundary layer over a NACA0012 is assumed to be a locally self-similar Falkner-Skan solution, and that each cell along the surface can be modeled as a wedge. Since the external flow along the surface is assumed to follow a power-law relation, a system of equations can be composed to determine the least square approximation of the Falkner-Skan parameters, β (half-wedge angle), and k (power law exponent). The wall-shear stress is obtained by using tabulated values for the relationship between β and $f'''(0)$. Gonzalez et al. (2020) tested this approach in stagnation flow and a spatially varying pressure gradient boundary layer flow. For both test

cases, the laminar wall model evidently outperformed the no-slip (no wall-modeling) or equilibrium wall-stress model. Moreover, the latter case shows that it is valid to assume local self-similarity over a surface.

However, remark that the original Falkner-Skan self-similarity solution assumes an inviscid flow. Therefore, viscous effects should be considered when applying Falkner-Skan in WMLES. Dauricio and Azevedo (2022) modified the Falkner-Skan formulation by including a correction factor that modified β to compensate for the (viscous) dissipation of the boundary layer. Furthermore, Dauricio and Azevedo (2022) tested their formulation on a NACA 0012 airfoil for various boundary layer growth rate, making h_{wm} a function of the streamwise direction. Regardless of the growth rate, the self-similar wall model shows good agreement with reference data, but underestimates the peak skin friction at the leading edge and overestimates the skin friction in the decelerated region.

The present author has only found a handful of papers on laminar wall-modeling, which is possibly due to the recent awareness regarding the importance of modeling the laminar part of the boundary layer. A second and last proposed laminar wall-modeling approach is discussed next.

2.3.7. POLYNOMIAL-BASED WALL MODEL

The last proposed type of wall model is the polynomial-based (laminar) wall model that may in theory be used in both laminar and turbulent parts of the boundary layer. In essence, the approach aims to use local wall-normal instantaneous quantities which is fed into either a polynomial-based expression of the velocity profile (Woodruff, 2021) or a taylor series expansion (Unglehrt et al., 2022). The former analyzed the accuracy of predicting laminar-turbulent transition in WMLES. In doing so, proposed a pre-transitional (laminar) wall model using the wall-normal plus time derivatives. In particular, Woodruff (2021) considered a polynomial function of order m which is approximated by a least-square fit of the wall-tangent velocity values from m points above the wall. In contrast to wall-stress models, the obtained wall-shear stress is input at some distance above the wall, rather than at the wall itself since the shear stress of the laminar boundary layer is not constant in the near-wall region.

Unglehrt et al. (2022) on the other hand, proposed a third-order Taylor series expansion in which the higher-order derivatives are substituted with compatibility conditions (similar to the approach discussed in section 2.2.4) which results in a PDE for the wall-shear stress. In their work, the aim is to retrieve the correct wall-shear stress from a known velocity and pressure gradient by using only the nearest cell from the wall. Unglehrt et al. (2022) remark that this formulation may be further expanded by including both higher-order terms and the SGS model in the compatibility conditions.

Within the context of the present literature study, these two proposed wall models require a higher mesh resolution than typical WMLES mesh sizes. In fact, the wall model proposed by Unglehrt et al. (2022) is intended for WRLES, and results from Woodruff (2021) are based on a mesh resolution with the first grid point at $y^+ = 0.11$, and a subsequent work of Woodruff (2022) used a mesh resolution of $h = 0.035y/\delta$. Compare this with $\Delta y \leq 0.3h_{wm}$ for typical WMLES grid sizes (Kawai & Larsson, 2012) shows that the polynomial-based wall models are generally unsuitable for WMLES solvers.

2.4. TRANSITION MODELING IN RANS AND LES

With the shift in focus to wall-modeling laminar boundary layers, perhaps the reader wonders whether transition models exist in LES. This chapter focuses on such models developed in the (WM)LES literature, while also discussing similar models developed in RANS, which can potentially be used in LES.

The most famous transition model is the e^N model, which predicts transition based on linear stability theory by monitoring the value of N until a threshold is reached which implied transition. However, the applicability of these models are limited to simple geometries and low-fidelity codes as it requires knowledge of higher-order derivatives which even for current industrial CFD solvers are difficult to reconstruct. The discussion of such models is not the focus in this chapter. Instead, this chapter serves to summarize the previous efforts of applying transition models in RANS and LES.

2.4.1. TRANSITION MODELS IN LES

Roughly a decade ago, Bodart and Larsson (2012) remarked that the predicted skin friction is overestimated by traditional wall models (EQWM) and that the sensitivity to an adverse pressure gradient is limited due to a thicker (turbulent) boundary layer. Consequently, this may result in erroneous flow prediction over the surface of the geometry. Therefore, Bodart and Larsson (2012) looked for a way to distinguish between a laminar or turbulent boundary layer so that separate treatment of the two types of boundary layers can be applied. To achieve this, they used a measure of the local kinetic energy ($u_i^{'}u_i^{'}/2$) normalized with the predicted local friction velocity (u_τ) shown in eq. (2.38). DNS datasets of turbulent channel flow from $180 < \mathscr{R}e_\tau < 2000$ show that this quantity roughly approaches a constant value for $y^+ > 10$ and $y/\delta > 0.2$, which aligns with the region of typical probing points for conventional wall models. For laminar regions, they simply switched off the turbulent wall model which corresponds to solving an underresolved LES.

$$s_{\text{tl}}(x_w, t) = \frac{\left\langle \sqrt{u_i' u_i'/2} \right\rangle}{\langle u_\tau \rangle} \tag{2.38}$$

Test cases performed on an multi-element airfoil and transitional boundary layer show a much better agreement to reference data and prove that adequate treatment of the laminar bounary layer is important for an accurate reconstruction of the flow. While transition physics are not considered, Bodart and Larsson (2012) showed that knowing the transition location, and consequently the laminar and turbulent boundary layer regions are essential towards high-accuracy WMLES.

Much later, Duda et al. (2019) described a similar transition model. As a result, the predicted τ_w from the wall model and the corresponding value of k_{wm} are compared to the local resolved value of k_{LES} in the LES domain. When $k_{\text{LES}} > k_{wm}$, a turbulent flow is assumed, otherwise the flow is laminar. A blending function is also used for the transition region, acknowledging that a pure laminar or turbulent wall model cannot return the skin friction accurately in this region.

In the work of Woodruff (2021), a wall model for the pre-transition (laminar) region is discussed together with a simple blending function for the transition region to study the

possibility of using WMLES in boundary-layer transition investigations. His work shows that transition prediction is possible given three requirements. Namely, that an accurate laminar (pretransition) wall model is utilised, a transition region is considered between the laminar and turbulent wall model, and finally that limitations must be respected regarding the viable spatial and temporal resolution to capture transition physics.

Models to treat the transition region in LES have not been extensively studied yet. In fact, the bulk of transition modeling studies are performed in the RANS domain.

2.4.2. TRANSITION MODELS IN RANS

Two philosophies are mainly followed in the development of transition models in RANS, as remarked by Menter et al. (2022). Either an approach using (linear) stability theory or a form of RANS-type method is followed. The former aims to track the growth of instabilities of the flow up to transition e.g., e^N method is a famous example of this. However, e^N requires reconstruction of higher-order derivatives which is not suitable for general-purpose CFD codes, where lower-order numerical methods are used and hence are not discussed further. RANS-type methods however, utilises various forms of curve-fitting to establish low-cost empirically-based parametric equations. Such methods have gained many variations over the years of which five are discussed briefly.

LCTM: $\gamma - \mathscr{R}e_\theta$

The earliest locally formulated transition model is the $\gamma - \mathscr{R}e_\theta$-model, also described by Langtry and Menter (2009), which solves two additional transport equations to predict transition. Namely, the intermittency (γ) which describes the coverage of turbulent patches at a given streamwise location, and the momentum thickness based Reynolds number ($\mathscr{R}e_\theta$) which detects transition onset. Both parameters rely on tuning based on experimental correlation to obtain accurate results. Nevertheless, $\gamma - \mathscr{R}e_\theta$ incorporates both freestream turbulence and pressure gradient changes in transition onset prediction.

LCTM: γ

Later, Menter et al. (2015) reduced the $\gamma - \mathscr{R}e_\theta$-model to a single transport equation, only needing to solve the intermittency equation. The detection of transition onset in this model is based on computing the wall-normal velocity derivative which serves to approximate the local pressure gradient. Later on, different variants of this one-equation model are proposed which either extends it, or instead uses a different set of correlation parameters. Several variants of these models are summarised by Menter et al. (2022).

LCTM: ALGEBRAIC

A recent development following the one-equation transition models are algebraic models which do not require solving additional PDEs, significantly reducing the computational cost. Many variants of algebraic models exist that are based on different parameters to predict transition onset (Kubacki et al., 2020; Menter et al., 2022; Sandhu & Ghosh, 2021). Some are intended for different environments e.g., high turbulent intensities (Kubacki et al., 2020), and tuned in combination with a certain turbulence model.

$k_T - k_L - \omega$

Alternatively to the above correlation-based models which require extensive tuning, a more physics-based approach can be used. Walters and Cokljat (2008) proposed a turbulence model capable of predicting transition, consisting of three transport equations which follow the turbulent (k_T) and laminar (k_L) kinetic energy, as well as the turbulent specific dissipation rate, ω. Due to the three transport equations, the model is rather complex and therefore difficult to tune and combine with other turbulence models other than the $k-\omega$ turbulence model used in the original paper.

AFT MODEL

Lastly, a transition model based on linear stability theory has been proposed by Coder and Maughmer (2014) that is also viable for general-purpose CFD codes and considers both natural and separation-induced transition. The method is inspired by the well-known e^N-method and transports an amplification factor N to trigger turbulence. Furthermore, in their paper the transition model is combined with the Spalart-Allmaras turbulence model, in total requiring only two transport equations to be solved. For an extensive comparison between the discussed transition models, the reader is referred to Lopes et al. (2020) and Menter et al. (2022).

3

METHODOLOGY

The three-dimensional weakly compressible Navier-Stokes equations are solved in the present work and discussed in section 3.1. Since the present solver is propietary, few details can be given. A short discussion is provided on the immersed boundary method and wall-modeling framework used in section 3.2, which is also discussed in Pasquariello et al. (2023).

3.1. NAVIER-STOKES EQUATIONS

The governing equations can be written as eq. (3.1). With $\mathbf{U} = \left[\rho, \rho u_1, \rho u_2, \rho u_2\right]$, the inviscid and viscous contributions follow eq. (3.2). u_i and τ_{ij} are the velocity vector and viscous stress components. This viscous stress component can be expressed by eq. (3.3), i.e. Stokes theorem for a Newtonian fluid. In LES, the dynamic viscosity is a linear combination of the fluid and the eddy viscosity, i.e. $\mu = \mu_{air} + \mu_{SGS}$ and in the present code, Sutherland's law (eq. (3.4)) is used to approximate the fluid viscosity given the (approximated) adiabatic wall temperature, reference velocity, u_{ref} and temperature T_{ref}.

A linearization of the ideal gas law results in the linear barotropic equation of state eq. (3.5), where A and B are constants derived from the specific gas constant for air. With the NASA Glenn polynomials (McBride et al., 2002), C_p is obtained which consequently determines the γ_{ref}, closing the system of equations.

$$\partial_t \mathbf{U} + \nabla \cdot \mathbf{F}(\mathbf{U}) - \nabla \cdot \mathbf{D}(\mathbf{U}) = 0 \tag{3.1}$$

$$\begin{aligned} \mathbf{f}_i(\mathbf{U}) &= \left[u_i \rho, u_i \rho u_1 + \delta_{i1} p, u_i \rho u_2 + \delta_{i2} p, u_i \rho u_3 + \delta_{i3} p\right]^T \\ \mathbf{d}_i(\mathbf{U}) &= \left[0, \tau_{i1}, \tau_{i2}, \tau_{i3}\right]^T \end{aligned} \tag{3.2}$$

$$\tau_{ij} = \mu\left(\partial_j u_i + \partial_i u_j - 2/3 \delta_{ij} \partial_k u_k\right) \tag{3.3}$$

$$\mu_{air}(T_w) = \mu_{ref}\left(\frac{T_w}{T_{ref}}\right)^{3/2}\frac{T_{ref}+S_{ref}}{T_w+S_{ref}} \tag{3.4}$$

$$T_{ref} = 273.15\ \text{K},$$
$$\mu_{ref} = 17.16\times10^{-6}\ \text{Pa s},$$
$$S_{ref} = 110.4\ \text{K},$$
$$T_w = T_{ref} + \frac{u_{ref}^2}{2C_p(T_{ref})}$$

$$p(\rho) = A\rho + B \tag{3.5}$$
$$A = \gamma_{ref} R T_{ref}$$
$$B = (1-\gamma_{ref})p_{ref}$$

3.2. IMMERSED-BOUNDARY METHOD

The present solver uses a ghost-cell immersed boundary method illustrated in fig. 3.1, in which four types of cells are present. Namely, fluid, solid, ghost and wall-model cells. To help identify these cells a signed distance field is created around the geometry. Fluid cells define the inner computational domain where fluid variables are defined and have positive signed distance. Solids are cells fully contained in the geometry. Ghost cells are cells (partially) contained within the geometry and in which the boundary conditions on the surface are imposed and hence have negative signed distance. Numerically, cells are marked as ghost cells if they have at least one fluid-cell neighbor. Lastly, the wall model is evaluated in the wall-model cells which are the nearest cells above the geometry (positive signed distance). Similarly, a cell is marked as a wall-model cell if it has at least one ghost-cell neighbor. Two image points at 2Δ (IP1) and 1Δ (IP0) normal to the immersed boundary are used to probe fluid information for the wall model.

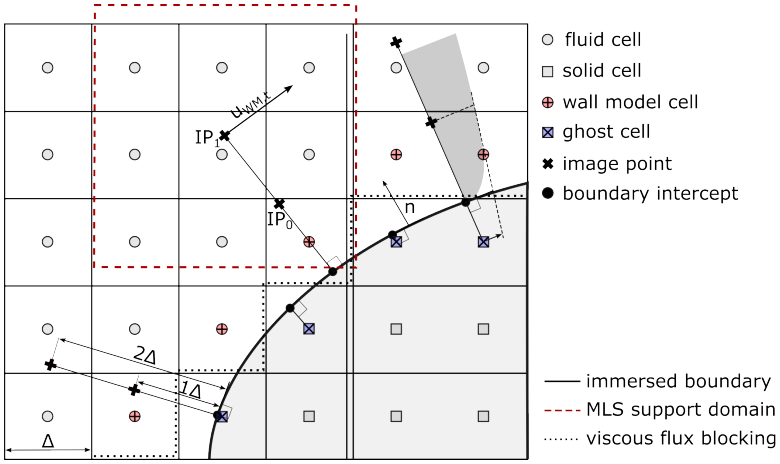

Figure 3.1: Schematics of the ghost-cell immersed boundary method and wall-modeling framework (Pasquariello et al., 2023).

3.3. WALL-MODELING FRAMEWORK

In the present solver, an equilibrium wall-stress model has been developed, where fluid information is exchanged at 2Δ normal to the immersed boundary to compute the wall-shear stress, τ_w. Moving-least-squares (MLS) regression is performed with linear basis functions with neighboring fluid cells to determine the fluid information at the exchange location. The wall-model cells act as a source term by imposing the modeled shear stress onto the fluid domain. It is assumed that the wall function models the total viscous stress, hence the resolved viscous flux is blocked at wall-model cell faces adjacent to ghost cells.

A partial slip velocity boundary condition is imposed on the ghost cells as suggested by Tamaki and Kawai (2021) to alleviate numerical errors introduced by the underresolved near-wall region. The wall-tangential velocity is prescribed using the wall-normal velocity gradient evaluated at 1Δ away from the wall, see fig. 3.1. The wall-normal velocity is obtained by imposing a zero-penetration boundary condition.

4

LAMINAR WALL-MODELING

This chapter discusses the implementation of the laminar wall model i.e., the local Falkner-Skan wall model (FSWM). First, a recap of the theory underlying the FSWM is given in section 4.1. After which the implementation of the FSWM in the present solver is elaborated in section 4.2, which includes details regarding the computation of the distance field, surrogate modeling, velocity probing, and wedge angle computation.

4.1. THEORY

By assuming self-similarity the velocity profile is assumed to retain its shape in the streamwise direction. This self-similarity is achieved by transformation of coordinates, which in this case is done by prescribing an external velocity profile U_e, and similarity variable η, which describes the height of the velocity profile.

$$U_e(x) = Kx^m \tag{4.1}$$

$$\eta = \frac{y}{x}\sqrt{\frac{m+1}{2}\frac{U_e x}{\nu}} \tag{4.2}$$

For the Falkner-Skan formulation, the coordinate transformation is achieved using eq. (4.1) and eq. (4.2), where m is a chosen parameter. Remark that eq. (4.1) implies that a power-law external velocity profile is prescribed and consequently dictates the induced pressure gradient of the boundary layer. In particular, $\frac{dp}{dx} < 0$ for $m > 0$ and $\frac{dp}{dx} > 0$ for $m < 0$. Substituting the similarity variables into the incompressible laminar boundary layer equations results in the Falkner-Skan similarity solution, eq. (4.3), where β is the Falkner-Skan parameter. $f'(\eta)$ is the wall-tangential velocity of the boundary layer and $f''(\eta)$ the wall-tangential acceleration.

$$f''' + ff'' + \beta(1 - f'^2) = 0, \quad \beta = \frac{2m}{1+m} \tag{4.3}$$

In their implementation, Gonzalez et al. (2020) and Dauricio and Azevedo (2022) assumed local self-similarity to compute the Falkner-Skan solution at each computational node. Gonzalez et al. (2020) achieved this by computing the parameters K and m by solving the least-square approximation of eq. (4.1). Knowing U_e and m, the wall shear stress is subsequently computed.

Dauricio and Azevedo (2022) differed slightly in that instead of using information of neighboring cells, only local cell information is used. This is achieved by geometrically computing the parameter m using the streamwise and cell tangential unit vectors. Furthermore, they applied a viscous correction factor tuned to $\mathscr{R}e_c$. For both approaches, the wall shear stress is computed by eq. (4.4), where x denotes the surface distance from the stagnation point. In the present implementation, the approach of Dauricio and Azevedo (2022) is followed as only local information is required.

$$\tau_w = \mu \sqrt{\frac{1}{2-\beta}\frac{U_e^3}{\nu x}} f'' \Big|_{\eta=0} \tag{4.4}$$

4.2. IMPLEMENTATION

The discussion how the Falkner-Skan wall model is implemented is presented subsequently. The implementation consists of two parts, namely the core formulation and the additional logic required to apply the wall model in more general applications.

4.2.1. FORMULATION

The Falkner-Skan wall model proposed by Dauricio and Azevedo (2022) requires the computation of the wedge angle for each computational node of the geometry. In the present solver, the normal vector of each triangle face is available. If the boundary layer edge velocity is known, then the wedge angle and the similarity variable η can be obtained. Consequently, these quantities are used to solve eq. (4.4). The wall-normal derivative $\frac{du}{dy}$ is obtained from eq. (4.4) by omitting the dynamic viscosity. Note that the double derivative, $f'' \big|_{\eta=\eta_{IP}}$ is evaluated at the height of the probing point in that case. To determine f'' a surrogate model is implemented. This surrogate model is further elaborated in section 4.2.2.

Ideally, the probing point of the laminar wall model is outside the boundary layer to obtain an approximation of the local edge velocity. This is in contrast to equilibrium wall models, where the probing point is ideally located within the logarithmic region of the boundary layer. This may pose a problem if WMLES is performed where the mesh resolution is sufficient to somewhat resolve the laminar boundary layer which caues the edge velocity to be underestimated. A similar problem occurs if the mesh is too coarse: the probed velocity is too far away from the boundary layer. To alleviate this issue, an inviscid approximation of the edge velocity U_e can be obtained by Bernoulli's principle, shown in eq. (4.5). However, since this is a potential flow approximation, significant discrepancies may occur in the predicted velocity distribution compared to the viscous flow solution.

$$\frac{U_e}{U_\infty} = \sqrt{\frac{p - p_{ref}}{2}} \tag{4.5}$$

The approach presented above can be used as is without additional work for simple geometries such as flat plates, wedges, and symmetric airfoils. However, when dealing with more complex geometries the reference (starting point) of x must be known. The starting point of x in this case is the stagnation point (or line) of the geometry and must

be known a priori or detected. The distance of all cells with respect to this reference point or line must be computed, which is further discussed in section 4.2.4.

Figure 4.1 shows the flow diagram of the FSWM. First, the wedge angle is computed by computing the angle between the wall-tangent ($\overline{u}_t$) and freestream ($\overline{u}_\infty$) velocity vector. Two exception handling routines are then passed which checks if the distance is at least some epsilon away from the stagnation point and whether the wedge angle is within the applicable range ($-0.1980 < \beta < 2.0$). If both are satisfied, the similarity variable η is computed using additional geometric and flow field information. Namely, the distance from the stagnation point x, the wall-normal distance y, the dynamic viscosity μ, local fluid density ρ, and the boundary layer edge velocity U_e. After determining η, the corresponding non-dimensional velocity derivative f'' at $\eta = 0$ and $\eta = \eta_{IP}$ are computed, which are consequently transformed to determine the wall-shear stress and the wall-normal derivative at the image point.

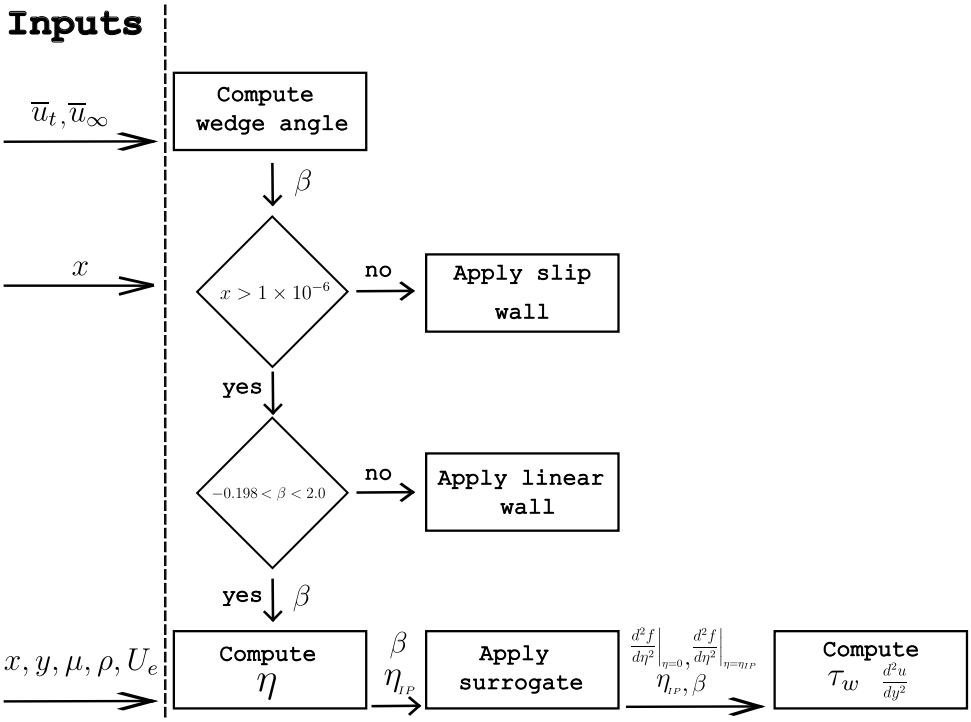

Figure 4.1: Flow diagram of the Falkner-Skan wall model. Here, x is the distance from the stagnation point and y the wall-normal distance. The input variables are retrieved from the geometry and flow field.

4.2.2. SURROGATE MODELING

For each computational cell, the wall-shear stress as well as the wall-normal velocity derivative are approximated using Falkner-Skan equations. Therefore, to obtain these two quantities an ODE must be solved for each computational cell. Solving the FS equations is typically done using a shooting method. However, evaluating the ODE for each

computational cell adds substantial computational cost. To reduce this cost, a look-up table is used instead to obtain an estimate for $f''|_{\eta=0}$.

To obtain $f''|_{\eta=\eta_{IP}}$, the wall-normal derivative at the location of the probing point, a surrogate model for the FS response surface with 25 points (five points in each direction) in (β,η) space is evaluated using bilinear interpolation. These data points are summarized in table A.1 and are near-uniformly placed between $\eta \in [0.0, 4.0]$ and $\beta \in [-0.1980, 2]$ to include all wedge angles. The maximum of $\eta = 4.0$ is chosen as the velocity profiles for $\beta \geq 0$ reach the edge velocity well before $\eta = 4.0$. f'' is set to zero in the case that $\beta > 4.0$.

The response of this surrogate model is compared to the actual response from the ODE in fig. 4.2. It can be remarked that in general f'' is overestimated in regions containing a large gradient ($\eta > 2.0$). Only for adverse pressure gradients ($\beta < 0$) an underestimation of f'' is observed around $1.5 < \eta < 2.5$, which is also shown in fig. 4.2b.

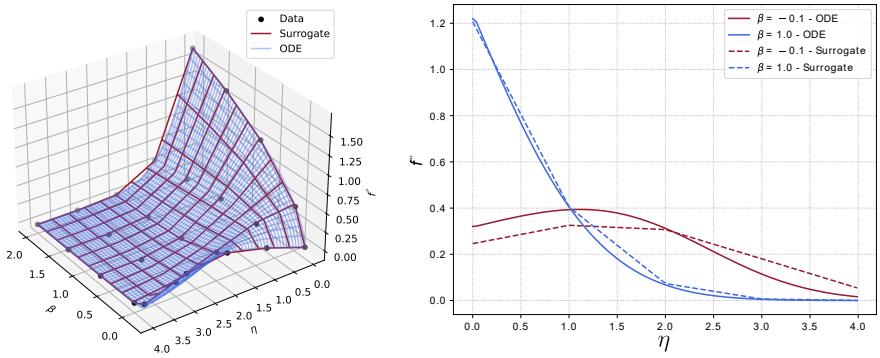

(a) (b)

Figure 4.2: (a) Comparison of the surrogate model with the (a) surface response of the Falkner-Skan ODE, and (b) two selected β angles. The black dots denote the data points used in the surrogate model.

4.2.3. LAMINAR SEPARATION

Unique solutions of the Falkner-Skan equation exist only for $\beta \geq 0$ and at least two solutions exist for $-0.1988 \leq \beta \leq 0$ (White, 2006). For $\beta \leq -0.1988$ infinitely many solutions exist which model separated velocity profiles. In the present implementation, the Falkner-Skan method is used for $\beta \in [-0.1988, 2.0]$. For $\beta < -0.1980$ the flow is assumed to be separated and a no-slip boundary condition is applied. For $-0.1988 < \beta < 0$, the solution is used without backflow at the wall.

4.2.4. LEVEL SET REINITIALIZATION

Modeling laminar boundary layers requires knowing the distance from the stagnation point. To obtain such a distance field, a level set reinitialization (LSR) algorithm is used to find the signed distance field with respect to the stagnation point.

LSR makes use of the fact that the spatial gradient of the signed distance field is one. Therefore, any arbitrary vector field can be forced towards a signed distance field. The

only constraint is that this candidate vector field must have the same zero-crossing as the desired signed distance field.

In other words, let Φ be the candidate scalar field then s the desired signed distance field, where the latter is obtained by solving eq. (4.6), where $S(.)$ is the sign function and $\frac{\partial \Phi}{\partial t}$ is the time derivative of Φ. Note that this time variable is a pseudo time to drive Φ to s. Furthermore, numerical smearing via eq. (4.7) is introduced to prevent oscillatory convergence (Fedkiw et al., 1999).

$$\frac{\partial \Phi}{\partial t} = S(\Phi)(|\nabla \Phi| - 1) = 0 \tag{4.6}$$

$$S(\Phi) = \frac{\Phi}{|\Phi| + \Delta l} \tag{4.7}$$

SIMPLIFIED FEDKIW

A well-known algorithm to solve eq. (4.6) is described by Sussman et al. (1994). However, several conditionals (if-else statements) are needed to implement this algorithm. This can lead to thread divergence in parallel programming in which not all parallel-executed threads finish at the same time, consequently leading to efficiency loss. Several simplifications are therefore made in the present implementation. Firstly, only the (unsigned) distance field is needed. Therefore, the sign function is neglected. Secondly, the distance field is initialized as a uniform field except at the stagnation line, which acts as a boundary condition for the convection equation defined by eq. (4.6). Thirdly, the upwind direction is determined by comparing direct neighboring values.

The SDF along a surface geometry is solved as part of the laminar wall model. In the present implementation, the SDF is computed on an unstructured triangular grid, where a dual grid approach is used. In particular, the distance field is described on the vertices, while the gradient is computed on the face neighbors using a per-cell linear estimation (Mancinelli et al., 2018). Afterwards, the upwind direction at each vertex is determined based on the face neighbor gradient information.

GRADIENT COMPUTATION

A per cell-linear estimation method is used to compute the gradient at the triangle faces described in Mancinelli et al. (2018) and is summarized here. It is assumed in this method that the distance field is defined at the vertices. Furthermore, if the distance field is assumed to be linear within a triangle, then the gradient is constant within a triangle. As such, the gradient f_t can be geometrically computed using eq. (4.8), where v_i, v_j, and v_k denote the three vertices of the triangle, $\frac{(v_i - v_k)^\perp}{2A_t}$, is the dot product between edge e_{ik} and the normal vector of the triangle (rotation with respect to the normal vector), and A_t is the area of the triangle.

$$\nabla f_t = \left(f_j - f_i\right) \frac{(v_i - v_k)^\perp}{2A_t} + \left(f_k - f_i\right) \frac{\left(v_j - v_i\right)^\perp}{2A_t} \tag{4.8}$$

As the distance field is defined on the vertices, the gradient information on the faces are used to determine the upwind direction. Inverse-distance weighted averaging is used

to determine the upwind gradient. A face gradient is considered upwind if two of its three vertices possess an upwind distance value. In case zero upwind neighbors are found, the upwind gradient is assumed to be zero. As a result, the reinitialization step performs a full "correction". A schematic of the upwind selection is shown in fig. 4.3a. In this example, a linear distance field is present from bottom to the top. To determine the upwind gradient of the center node, the neighboring faces are checked if *all* unshared vertices hold a value lower than the evaluated node. In this case, only one upwind face is considered (marked in green) and the corresponding gradient is used to correct the evaluated node during reinitialization. If multiple neighboring faces are marked upwind then the average of their gradient is taken.

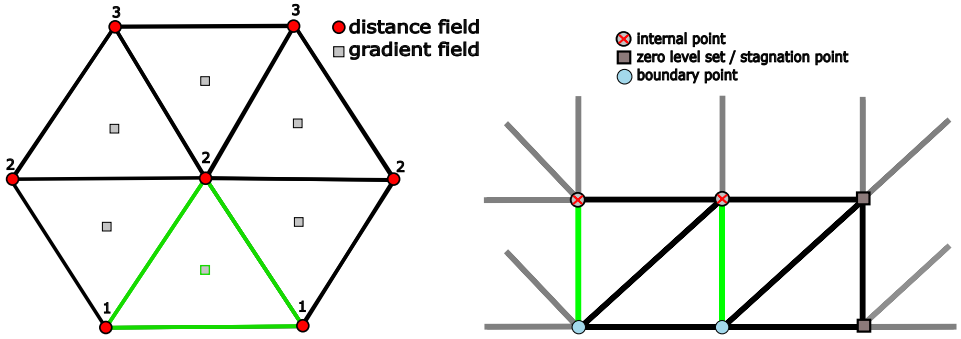

(a) (b)

Figure 4.3: Sketch of the upwind selection (a) and boundary condition applied (b) to ensure a uniform distance field.

BOUNDARY CONDITION

Since the boundary vertices do not have the same number of neighbors as internal vertices, the upwind gradient routine may lead to a far different upwind gradient which results in a non-uniform distance field along a symmetric body (e.g. airfoil, flat plate). Hence, a boundary vertex copies the gradient of the nearest internal vertex given that this vertex is not a stagnation point nor a boundary vertex. This situation is shown in fig. 4.3b, where the green edges indicate the shared gradient information between the two vertices.

STOPPING CRITERIA

The algorithm is stopped after the root-mean square error of $\nabla\Phi$ reaches below 1×10^{-6}. However, note that eq. (4.6) is an advection-like equation. From the zero level set multiple fronts are propagated during the reinitialization. At a certain point these fronts collide, creating an interface and resulting in the breakdown of the algorithm. Continuing the algorithm affects also the (converged) distance field in the vicinity of the colliding fronts. Hence, an additional stopping criteria is applied, where non-monotonic convergence is tracked. Namely, it is counted when the error of the current iteration is larger than the previous error. If this occurs more than ten times, the algorithm stops.

4.2.5. VERIFICATION

Verification is performed on the level set reinitialization method on several simple geometries. These include a flat plate, cylinder, sphere, and a NACA 0012 airfoil.

FLAT PLATE

The zero level set is imposed for vertices $x < 0.01$ of the STL. As a result, the distance field is rectangular with a maximum on the right edge of the STL. The numerical values along the x-coordinate are shown in fig. 4.4a with a RMS error below 1×10^{-6}. For the RMS computation, the numerical curve is corrected for the offset in the distance field due to the finite width of the zero level set (the level set is applied to a row of triangle faces). This is also performed for subsequent test cases.

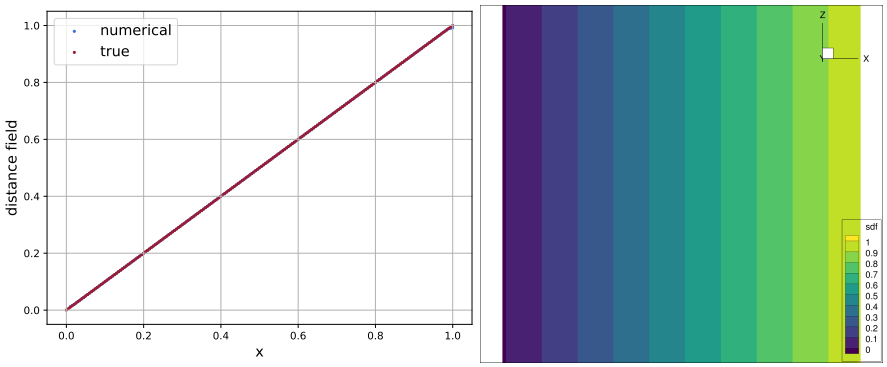

(a) (b)

Figure 4.4: Distance field along a flat plate with zero level set imposed for vertices satisfying $x < 0.01$.

CYLINDER

The zero level set is imposed at $(x, y) = (1, 0)$ after which the reinitialization algorithm propagates the distance field in both directions. The distance field is shown in fig. 4.5a. Note that the advecting waves in both directions collide at the other end of the cylinder, developing an interface. Regardless of the stopping criteria, the distance field value diverges towards a value larger than the analytical maximum at this interface. This is deemed acceptable as the distance field is only used near the zero level set (stagnation point). A RMS error of 1.5×10^{-5} is reached excluding the diverged data points.

SPHERE

A zero level set is imposed at one of the poles of a sphere. In this case, the advection wave propagates in all directions and an interface is developed at the opposing pole. From fig. 4.6a, it is remarked that the discrepancy at the interface is limited. The dashed line indicates the true maximum value of the distance field ($\pi/2$). A RMS error of 1×10^{-4} is found which is partially attributed to the inaccurate location of the zero level set, which is not exactly located at the pole. This also explains the offset seen between the true distance (from pole to pole) and the numerical approximation. Lastly, the non-uniform mesh also contributes to the larger error.

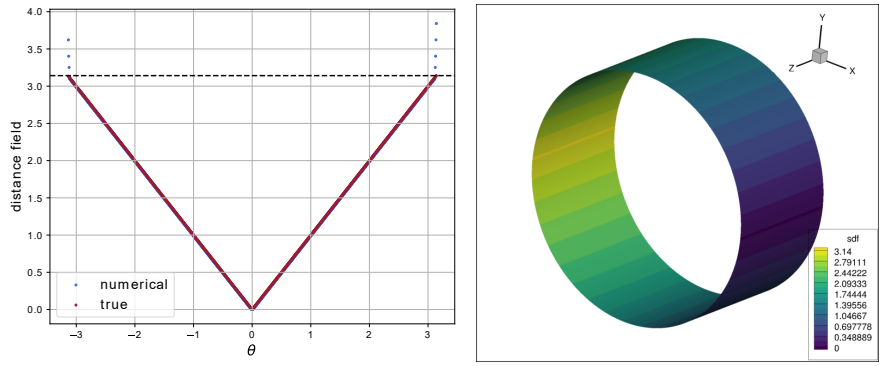

(a) (b)

Figure 4.5: Distance field along a cylinder with the zero level set line imposed at x_{max}.

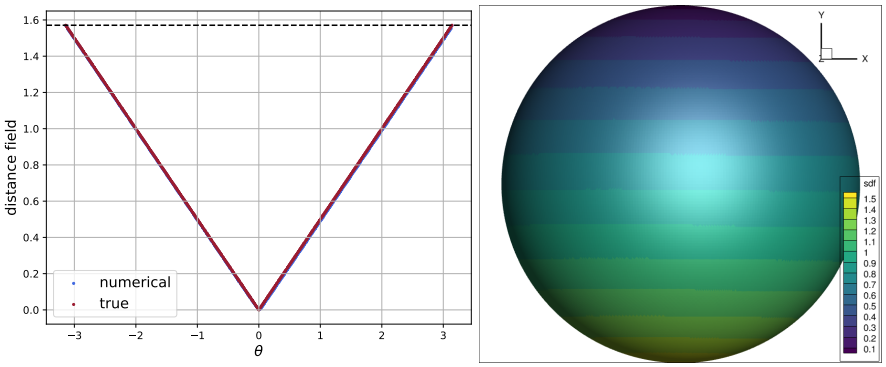

(a) (b)

Figure 4.6: Distance field along a sphere with the zero level set imposed at y_{max}.

AIRFOIL

Lastly, a stagnation line is imposed on a NACA 0012 airfoil at 0.0 x/c, and the results are compared with the distance field from XFoil. Figure 4.7b shows the distance field near the zero level set which closely follows the distance field according to XFoil. A good match is also found between the XFoil and present result beyond the leading edge with a RMS error of 2×10^{-5}.

In the present implementation it is observed that the stopping criteria for non-monotonic convergence occurs more often than reaching the 1×10^{-6} threshold. While the accuracy reached with the present implementation is sufficient for the current use case, the author suggests a special treatment for the interface(s) due to these colliding fronts to improve the accuracy of the computed distance field.

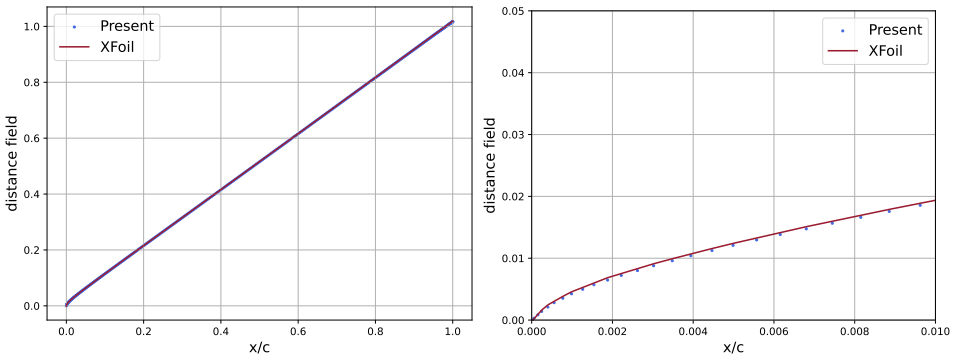

(a) (b)

Figure 4.7: Distance field along a NACA 0012 airfoil where the zero level set (stagnation line) is imposed at $x/c = 0$.

5

TRANSITION MODELING

To apply the computed shear stress in the appropriate regions, a transition model is implemented to distinguish laminar and turbulent regions. In view of the computational cost of more complicated transition models, the simple turbulent-laminar sensor from Bodart and Larsson (2012) is used to distinguish laminar and turbulent boundary layers. This chapter summarizes the formulation of the sensor in section 5.1, after which the implementation and verification are elaborated in section 5.2 and section 5.3, respectively.

5.1. THEORY

Bodart and Larsson (2012) observed that the turbulent kinetic energy ($u_i' u_i'/2$) normalized by the friction velocity (u_τ) approaches a certain value range (1.5-2.0) for increasing $\mathscr{R}e_\tau$ in turbulent channel flow (TCF). This sensor is defined by eq. (5.1), where $\langle . \rangle$ denote time-filtered quantities.

$$s_{tl}(x_w, t) = \frac{\left\langle \sqrt{u_i' u_i'/2} \right\rangle}{\langle u_\tau \rangle} \tag{5.1}$$

$$\tau(t) = (S_{ij} S_{ij})^{-1/2} \tag{5.2}$$

- $s_{tl} = 0$ if laminar
- $s_{tl} > s_{tl,\text{threshold}}$ if turbulent
- $0 < s_{tl} < s_{tl,\text{threshold}}$ if under transition

By comparing the computed s_{tl} with a threshold value, a distinction can be made between laminar and turbulent regions. Bodart and Larsson (2012) used a value of 1.4 in their work which may differ for other CFD codes. In their work, an exponential moving average is used with the time integration constant τ based on the strain rate tensor

(eq. (5.2)) such that the weighting is determined by: $W(t) = \exp(-\Delta t/\tau)$. Remark that the value used is lower than the range (1.5-2.0) given earlier. Since the sensor is applied to WMLES, not all of the turbulent scales are resolved and consequently the s_{tl} becomes underestimated. Since eq. (5.1) only considers the resolved turbulent quantities, the threshold value should be adjusted to a lower value.

5.2. IMPLEMENTATION

In the present solver, the sensor is evaluated on the surface mesh using quantities of the flow field interpolated on to the unstructed triangular grid of the geometry. These quantities are time-filtered and used for the computation of the TKE, friction velocity, and the sensor value. Important to note is that the friction velocity is always computed using the shear stress computed by the turbulent wall model, in this case an equilibrium wall-stress model.

Bodart and Larsson (2012) used a time integration constant based on the strain rate tensor in their implementation. However, this requires connectivity in three directions from the neighboring cells which significantly increases the amount of computations performed. For practicability, the integration constant is a single value and is user-defined. Subsequently, a suitable constant τ is selected in section 6.4.2. A pseudocode of the present algorithm is shown in algorithm 1.

Algorithm 1 Sensor computation

new_weight $\leftarrow \exp(\Delta t/\tau)$
old_weight $\leftarrow 1 - \exp(\Delta t/\tau)$
for all $i \in \{0, \ldots, n_{\text{faces}}\}$ **do**
    u_IP, v_IP, w_IP, rho_$IP \leftarrow$ PROBEFLOWFIELD($loc_{IP}, \ldots$)
    ▷ *Grab filtered quantities from array*
    $u\_f, v\_f, w\_f \leftarrow$ filteredArr[idx_$u_f, \ldots$]
    $k_f \leftarrow$filteredArr[idx_k_f] ▷ *filtered square root of TKE*
    utau_$f \leftarrow$filteredArr[idx_utau] ▷ *filtered friction velocity*
    tau_w, rho_$IP \leftarrow$ CALLWALLMODELFUNC($loc_{IP}, \ldots$)
    ▷ *Compute fluctuating components*
    $u\_p \leftarrow u\_IP - u\_f$
    $v\_p \leftarrow v\_IP - v\_f$
    $w\_p \leftarrow w\_IP - w\_f$
    k_sqrt $\leftarrow \sqrt{0.5 * (u\_p^2 + v\_p^2 + w\_p^2)}$ ▷ *square root of TKE*
    utau $\leftarrow \sqrt{\text{tau\_}w/\text{rho\_}IP}$
    ▷ *Compute new sensor value and store in array*
    sensorArr[i]$\leftarrow k_f/$utau_f
    ▷ *Update time-filtered quantities*
    FilteredArr[idx_u_f]$\leftarrow$ new_weight $\times u\_IP +$ old_weight $\times u\_f$
    $\ldots$
    FilteredArr[idx_k_f]$\leftarrow$ new_weight $\times k$_sqrt$+$ old_weight $\times k\_f$
    FilteredArr[idx_utau]$\leftarrow$ new_weight $\times$utau$+$ old_weight $\times$utau_f
end for

5.3. VERIFICATION OF SENSOR IMPLEMENTATION

A verification of the sensor implementation is performed by running a laminar flat plate and turbulent channel flow case. The former should result in a very low to zero value of the sensor value, while the TCF case should produce a sensor value close to the range of 1.5-2.0. In this verification, the sensor is updated every 100 iteration with a preliminary time integration constant of 1×10^{-2}.

5.3.1. LAMINAR FLAT PLATE

A zero sensor value indicates zero turbulence. In practice, even in laminar flow the value can be slightly non-zero due to numerical noise. To verify the working of the sensor, laminar flow over the flat plate is simulated with a domain length and height of $L = H = 10$, $\mathscr{R}e = 10,000$, and $M = 0.1$. Riemann boundary conditions are used for the inlet, and top patches. A symmetry condition is imposed in the spanwise directions and a static pressure outlet is applied. The result is shown in fig. 5.1. As expected, the sensor value remains close to zero although the value increases along the streamwise direction. This is expected as the friction velocity reduces (τ_w decreases along the length of the plate), while local disturbances grow (increase in TKE).

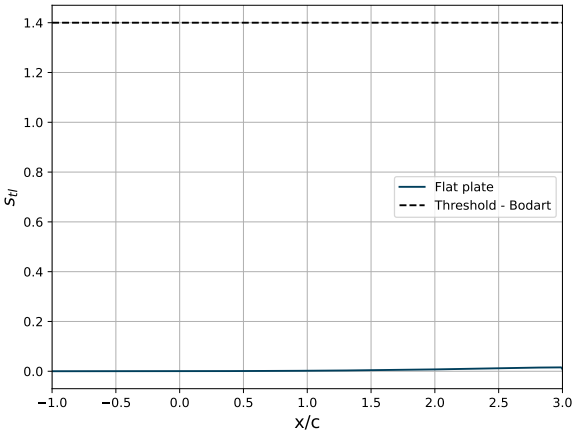

Figure 5.1: Spanwise-averaged sensor value in the streamwise direction of a laminar flat plate

5.3.2. TURBULENT CHANNEL FLOW

Bodart and Larsson (2012) show that the threshold value should be found between 1.5 to 2.0 based on DNS data of TCF simulations at various $\mathscr{R}e_\tau$. In their paper, a slightly lower value of 1.4 is used which is acceptable as only the resolved part of the turbulent quantities in eq. (5.1) is used to detect transition. In WMLES only a part of the turbulence is resolved, therefore it is natural to expect a lower sensor value in WMLES compared to DNS near the transition location.

To verify that the present sensor implementation is close to the expected range of 1.5-2.0, a TCF simulation at $\mathscr{R}e_\tau = 5200$ is performed for two meshes shown in fig. 5.2 with $y^+_{min} \approx 40$, and $y^+_{min} = 20$ for the coarse and fine mesh, respectively. The figure clearly

shows a mesh dependence of the sensor value, in agreement with the reasoning that lower sensor values are expected if less turbulence is resolved. Hence, a value of 1.0 is chosen for the threshold value instead. Note that for the present study only a reasonable value is chosen and is not by any means optimized to be generally applicable for a wide range of flow cases.

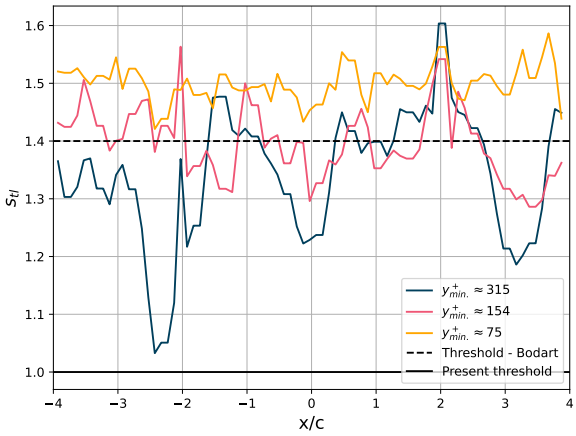

Figure 5.2: Spanwise-averaged sensor value in the streamwise direction of turbulent channel flow at $\mathscr{R}e_\tau = 5200$.

6

VALIDATION OF THE SENSOR-BASED WALL-MODELING APPROACH

The implemented turbulence sensor and FSWM are combined with the existing EQWM and integrated in a new wall model in the present solver. Subsequently, this new laminar-turbulent wall model is validated subsequently. First, academic test cases are presented which aim to validate the FSWM. Specifically, the laminar flate plate (section 6.1), and the wedge flow (section 6.2). Afterwards, laminar flow over a NACA 0012 airfoil is simulated and compared to reference simulations in section 6.3. Finally, section 6.4 tests the fully integrated laminar-turbulent wall model with the inclusion of sensor feedback and laminar and turbulent wall model switching by simulating a high Reynolds number flow over an airfoil under near-stall conditions.

6.1. LAMINAR FLAT PLATE

The laminar flow over a flat plate is simulated and follows the well-known Blasius solution. The described analytical solution is self-similar and applies to laminar flows when $\mathscr{R}e > 1000$ (White, 2006). First the setup of the case is discussed in section 6.1.1, after which a mesh convergence study is performed with three levels of mesh refinements in section 6.1.2. Finally, the FSWM is compared to the linear wall model in section 6.1.3. This linear wall model mimics a no-slip boundary condition in the present wall-modeling framework.

6.1.1. SETUP

For the simulation of a laminar flat plate, an eight unit long flat plate is present, with symmetry boundary conditions in the spanwise direction. A Riemann condition on the upper, and inlet boundaries is used, where a unit freestream velocity is imposed. A static pressure boundary condition is applied at the outlet. A unit Reynolds number of $1 \times$

10^4 is set. The gas properties are set to achieve a non-dimensional simulation. Finally, the simulation is run until $t = 80$. The case parameters and boundary conditions are summarized in table 6.1 and table 6.2, respectively. The flat plate is placed slightly above the bottom boundary patch and spans the whole domain. A slip wall is initially applied near the inlet up to two units from the inlet ($x = 2$).

Mach	$\mathscr{R}e$	L_x	L_y	L_z	SGS	Wall model	Fluid model
0.10	1×10^4	10.0	10.0	0.5	`Falkner-Skan / Linear`	-	`non-dimensional gas`

Table 6.1: Main simulation parameters for the laminar flat plate simulation.

X0	X1	Y0	Y1	Z0	Z1
`Riemann`	`Static pressure`	-	`Riemann`	`Symmetry`	`Symmetry`

Table 6.2: Boundary conditions for the laminar flat plate simulation.

	Min cell size [$\times 10^{-3}$]	Number of blocks	Number of cells [$\times 10^6$]
`Coarse`	15.6	17522	71
`Medium`	7.8	1100	6.4
`Fine`	3.9	3340	19.5

Table 6.3: Mesh settings for the laminar flat plate simulation. Each block contains 16^3 cells.

6.1.2. MESH CONVERGENCE

Figure 6.1 verifies the convergence of the integral drag (F_x) and lift (F_y) forces for the conducted simulations with the FSWM. Statistics are recorded after $t = 75$ as highlighted by the gray area. Note that small oscillations persist after convergence is reached. However, these oscillations are minute, having magnitudes in the order of 10^{-5}. Remark that a flat plate simulation is performed with the freestream flow tangent to the plate. While on first sight it may imply that F_y should oscillate around zero as no lift is generated, this is not the case as will be shown subsequently.

Figure 6.2 showcases the density and streamwise velocity field of the fine mesh. At $x = 2$ the symmetry boundary condition ends, and the flow impinges on the leading edge of the plate, resulting in a slight pressure gradient around this leading edge. As the flow continues downstream, a boundary layer is developed.

When comparing with the Blasius solution, the numerical solution at a given streamwise location $x_{phys.}$ is compared with the solution at $x_{Blas.}$ so that the $\delta_{99\%}$ is the same. This ensures a fair comparison of the predicted boundary layer properties as the boundary layer thickness is matching. Results are probed far away from both the inlet and outlet at $3 < x_{phys.} < 5$ to minimize boundary condition influences.

Figure 6.3 shows the boundary layer parameter distributions. Note that the x in these figures are not with respect to the leading edge, but matched to the boundary layer thickness ($\delta_{99\%}$) found using Blasius as mentioned earlier. Observing fig. 6.3a, a considerable underestimation of the displacement thickness δ^* is remarked and the boundary layer

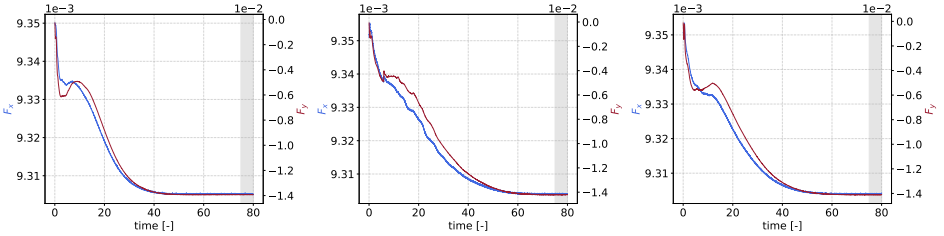

(a) (b) (c)

Figure 6.1: Drag and lift force convergence monitored for the three simulations performed with the FSWM: (a) coarse, (b) medium, and (c) fine.

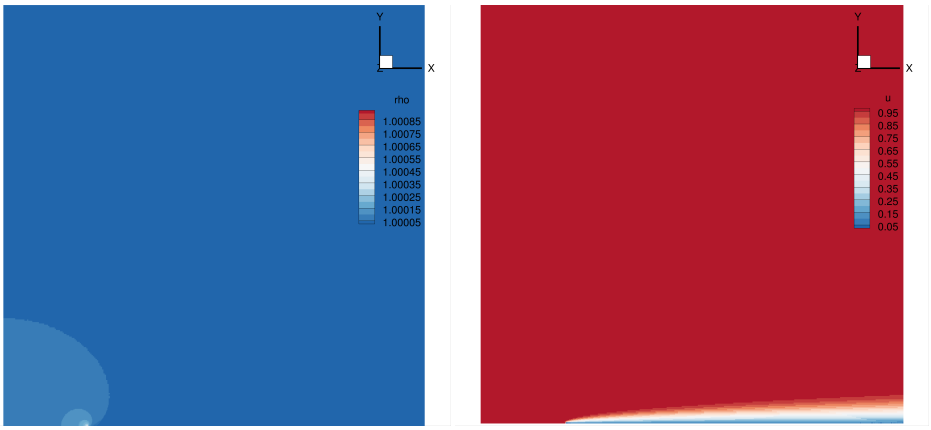

(a) (b)

Figure 6.2: Density (a) and u-velocity (b) field for the finest mesh.

growth is also less compared to the reference curve. Three levels of mesh refinement improves the discrepancy but a large offset remains.

In contrast, an overestimation of the momentum thickness θ is observed. The curvature shown by the medium and fine mesh are similar but offset to the Blasius curve, indicating a structural bias in the present simulation. The C_f distribution however, shows an underestimation compared to Blasius. Similarly to θ, the gradient of the numerical solutions is similar to the Blasius solution. With the FSWM, this indicates that there is a "lag" between $x_{phys.}$ and $x_{Blas.}$.

Indeed, while an underestimation of C_f combined with an overestimation of θ looks contradictory, the quantities are plotted against a virtual (Blasius) x-coordinate. Figure 6.3a shows that the streamlines outside the boundary layer are less displaced; the boundary layer is felt less by the external flow and so for the same δ^* one has to move further downstream i.e., $x_{Blas.} < x_{phys.}$. Figure 6.4 shows the same quantities plotted against the streamwise coordinate with respect to the leading edge.

The present results also show "wiggles" which is due to the linear interpolation used to compute the the boundary layer thickness ($\delta_{99\%} = 0.99U_e$). The interpolation be-

comes less noticeable as the mesh is refined.

The streamwise and wall-normal velocity profiles are shown in fig. 6.5b, where η is the non-dimensional similarity variable, describing the height of the self-similar boundary layer. The present results in fig. 6.5a show excess velocity throughout the boundary layer, and consequently a slip velocity near the wall. Mesh refinement reduces the discrepancy, but still remains for the finest mesh. The excess velocity is in agreement with the earlier results shown in fig. 6.3c: At a given boundary layer thickness, too few wall-shear stress is applied according to Blasius.

$$v = \sqrt{\frac{\nu U}{2x}} \left(\eta f' - f \right) \tag{6.1}$$

The wall-normal velocity is very sensitive as the magnitudes are very small, see also fig. 6.5b. Since v is defined by eq. (6.1), this means that each curve follows a different reference solution. An upwelling of the flow takes place due to the displacement effect of the boundary layer, hence a small non-zero wall-normal velocity exists in the external flow. Figure 6.5b shows convergence in the lower part of the curve, close to the wall. However, the FSWM fails to approach the correct far-field velocity. Note that the upwelling effect results in the earlier observed non-zero F_y shown in fig. 6.1. Zig-zag patterns may be seen in the present results and is due to probing near a mesh coarsening step during post-processing.

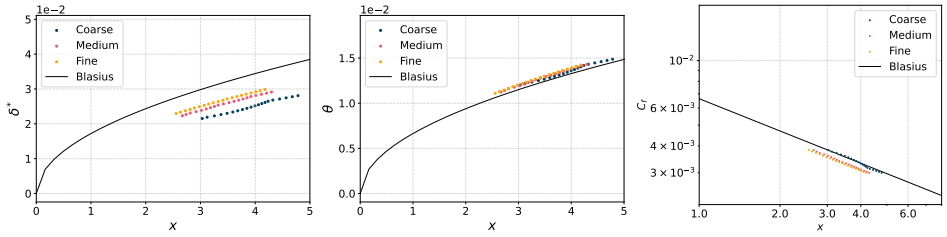

Figure 6.3: Displacement (a), momentum (b) thickness, and (c) skin friction distribution for three mesh resolutions plotted against the Blasius streamwise coordinate.

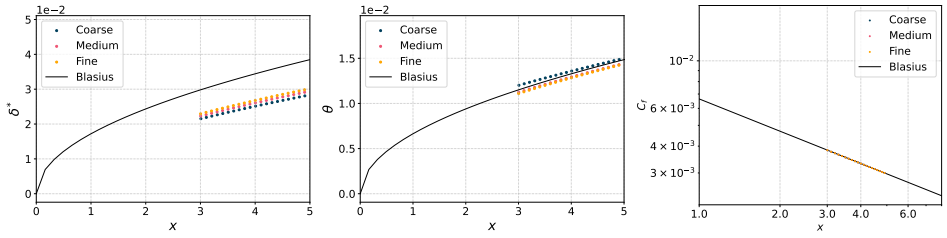

Figure 6.4: Displacement (a), momentum (b) thickness, and (c) skin friction distribution for three mesh resolutions plotted against the physical streamwise coordinate.

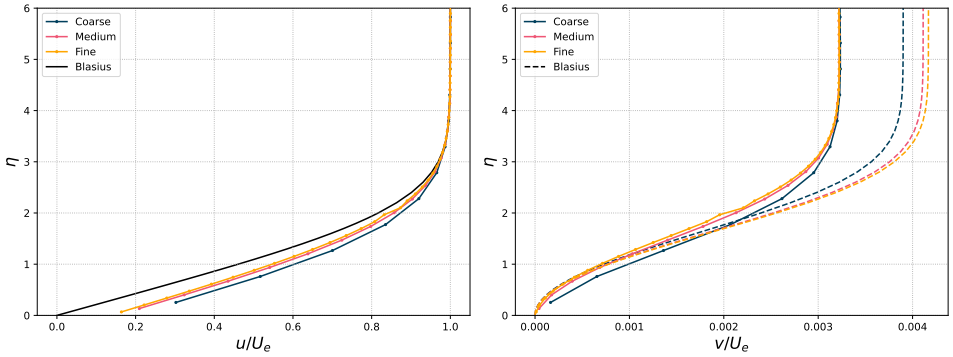

(a) (b)

Figure 6.5: Streamwise (a) and wall-normal (b) velocity profile for three mesh resolutions.

6.1.3. COMPARISON WITH LINEAR WALL MODEL

The FSWM is compared to a linear wall model on the fine mesh. The linear wall model assumes a zero slip velocity at the wall, and a linear relation for the shear and wall-normal derivative. For the present case study, where the laminar boundary layer over the flat plate is resolved this formulation is consistent as the velocity profile is indeed linear close to the wall. The boundary layer parameters and velocity profiles are shown in fig. 6.6 and fig. 6.7b, respectively. In general, the no-slip wall outperforms the FSWM and is able to approximate the boundary layer thickness very well. The linear wall model slightly overestimates C_f compared to Blasius, but also follows the linear trend in log scale. This is consistent with the results in fig. 6.6a. Namely, the boundary layer imposes a smaller displacement to the flow than Blasius, hence a larger velocity gradient exists near the wall, in turn resulting a higher wall shear stress and skin friction. Remark that the linear wall model has an advantage over the FSWM as the former is independent of x which allows it to adjust the wall-shear stress locally.

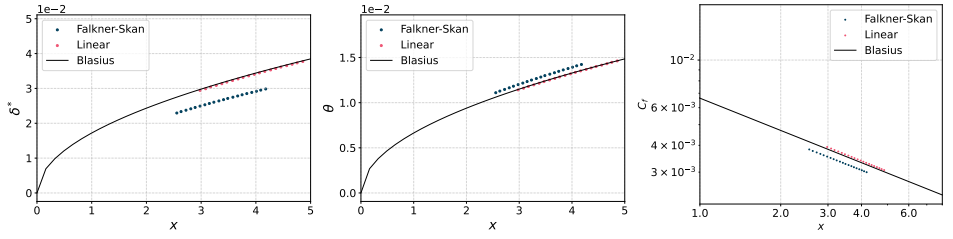

(a) (b) (c)

Figure 6.6: Displacement (a), momentum (b) thickness, and skin friction (c) distribution for two wall models.

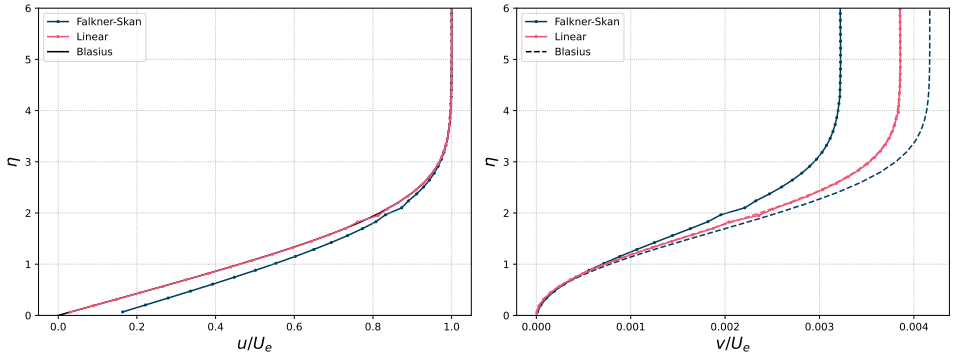

(a) (b)

Figure 6.7: Streamwise (a) and wall-normal (b) velocity profile for three boundary condiions. The dashed lines indicate the respective reference solution from Blasius.

6.1.4. LAG BETWEEN PHYSICAL AND BLASIUS COORDINATE

The essential issue of simulating laminar flow over a flat plate with the FSWM is the lag between $x_{Blas.}$ and $x_{phys.}$. The discrepancy along the flat plate is shown in fig. 6.8. Note that the lag is increasing throughout the domain with the FSWM. Although the magnitude is much smaller, this lag is also observed with a linear wall model. Hence, a fixed offset to the physical x-coordinate does not cause the FSWM to produce more accurate results.

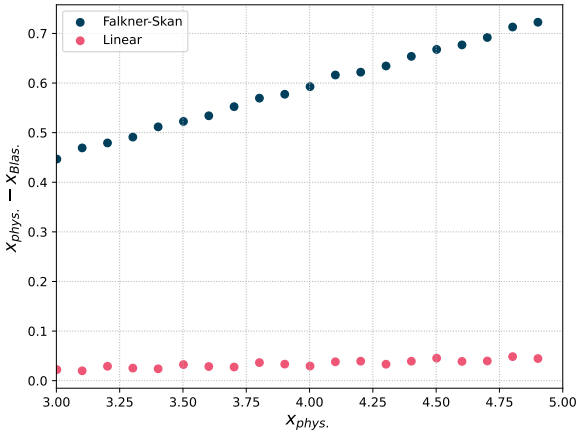

Figure 6.8: Lag between the physical streamwise coordinate (with respect to the leading edge) and the streamwise Blasius coordinate for the FSWM and linear wall model.

FSWM provides the shear stress based on the Blasius analytical solution to laminar flow on a flat plate. Consequently, the shear stress is applied at the provided x-coordinate regardless of the state of the flow. The latter can also be seen as a disadvantage to the present wall model.

Namely, x_{blas} corresponds to a given boundary layer thickness and associated shear stress. If the shear stress applied at the given $x_{phys.}$ does not match the boundary layer thickness at the same x-value in Blasius, then a different velocity profile is obtained. If $x_{phys.} < x_{blas.}$, then too much shear is applied to the given boundary layer at that slice. Potentially, this induces flow-reversal. When $x_{phys.} > x_{blas.}$, too few wall-shear stress is applied, resulting in a slip-velocity near the wall. This lack of shear also causes an excess momentum downstream, translating to a smaller boundary layer growth than predicted by the analytical Blasius equation.

The issues described above introduce a significant error to the obtainable boundary layer characteristics using FSWM compared to a linear wall model. As one approaches the wall asymptotically, all laminar boundary layers display a linear velocity profile. So for a resolved simulation a linear wall model is a natural and consistent choice. Additionally, a linear wall model does not rely on a streamwise distance x. Hence, a resolved simulation converges towards the Blasius solution beyond the influence of the leading edge.

It must be emphasized that the results above do not by any means imply that a linear wall model is a good option to model laminar boundary layers in WMLES application. The results obtained are accurate predominantly due to the boundary layer being resolved. In practice, especially in high Reynolds number flows this is not the case, as the very thin boundary laminar boundary layers are not resolved.

The laminar flat plate case is deemed to be difficult to simulate perfectly, especially given that the lag between the physical and Blasius x-coordinate remains non-constant throughout the domain.

6.2. WEDGE FLOW

To test the performance of the wall model also in non-face-aligned geometries, the inclined laminar flat plate case is performed. The flow can be seen as a wedge flow and follows the Falkner-Skan self-similar solution.

6.2.1. SETUP

The case setup is similar to the laminar flat plate case, where the only difference is the inclination of the plate which is set to 9° or $0.1\pi/2$. Again, the domain is $10 \times 10 \times 0.5$ with $M = 0.1$ and $\mathscr{R}e = 1 \times 10^4$. A unit freestream flows over a symmetry plane up to one-third of the domain, where the flow impinges and is accelerated over the wedge and a boundary layer is developed. A static pressure outlet is applied to drive the flow. Symmetry boundary conditions are applied in the spanwise direction. The setup and boundary conditions are summarized in table 6.4 and table 6.5, respectively. A sketch of the domain is also shown in fig. 6.9a.

The freestream velocity distribution over a wedge is known and is given by eq. (6.2) (White, 2006), where again β is the Falkner-Skan parameter, and K is an unknown. A power-law freestream flow field cannot be directly imposed above the boundary layer. Moreover, the implemented Bernoulli approach to obtain the incompressible estimate of U_e has shown to cause large oscillations over the wedge. It is found that passing the power-law relation directly to the FSWM eliminates these oscillations. Hence, in the subsequent wedge-flow simulations, the power-law relation is used with $K = 1$. In the subsequent case study, again a mesh sensitivity study is performed with three mesh refinement levels described in table 6.6. A comparison of the FSWM with the linear wall model is also conducted. The density and u-velocity field of the medium mesh are shown in fig. 6.9. Note the wedge angle in fig. 6.9c is exaggerated to show the developed boundary layer.

$$U_e(x) = K x^{\frac{\beta}{2-\beta}} \tag{6.2}$$

Mach	$\mathscr{R}e$	L_x	L_y	L_z	SGS	Wall model	Fluid model
0.10	1×10^4	10.0	10.0	0.5	`Falkner-Skan / Linear`	-	`non-dimensional gas`

Table 6.4: Main simulation parameters for the wedge flow case.

X0	X1	Y0	Y1	Z0	Z1
`Riemann`	`Static pressure`	-	`Riemann`	`Symmetry`	`Symmetry`

Table 6.5: Boundary conditions for the wedge flow case.

	Min cell size [$\times 10^{-3}$]	Number of blocks	Number of cells [$\times 10^{6}$]
Coarse	7.81	1415	8.3
Medium	3.91	6903	40.3
Fine	1.95	33888	197.6

Table 6.6: Mesh settings for the wedge flow case. Each block contains 16^3 cells

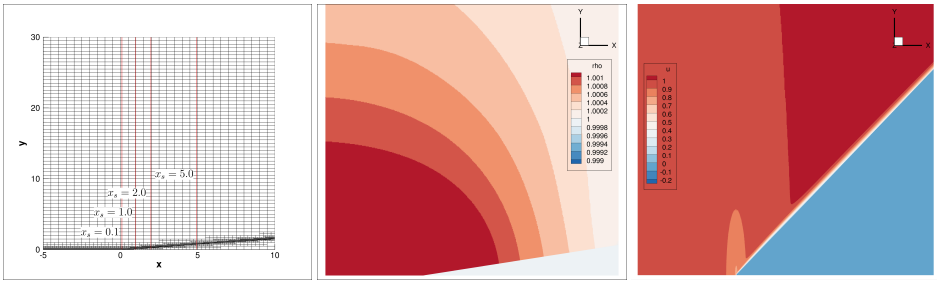

(a) (b) (c)

Figure 6.9: Domain (a), density (b) and u-velocity (c) field for the medium mesh.

6.2.2. MESH CONVERGENCE

Similarly to the case-aligned laminar flat plate case, results from the simulation are probed away from the outlet. The probed region is therefore limited between $0.0 < x < 5$ and is shown in fig. 6.9a, where x_s denote the wall-tangent distance from the tip. In contrast to the flat plate flow, x is with respect to the tip of the wedge ($x_{tip} = 0$). The convergence of present results for the three mesh levels are shown in fig. 6.10. Statistics are recorded between $t = 8$ and $t = 10$ highlighted by the gray area.

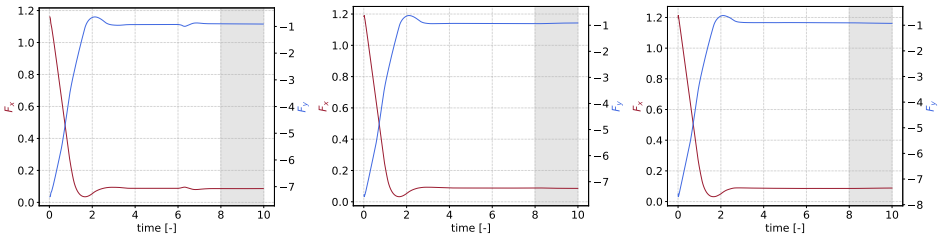

(a) (b) (c)

Figure 6.10: X- (F_x) and Y-force (F_y) convergence monitored for the three simulations performed with the FSWM: (a) coarse, (b) medium, and (c) fine mesh.

The u-velocity profiles at four x_s locations are shown in fig. 6.11. Again η denotes the similarity variable and can be seen as the non-dimensional boundary layer height. U_s and U_e are the wall-tangent and local edge velocity. The approximation improves with mesh refinement, however it is evident that the discrepancy between the present results and the analytical Falkner-Skan velocity profile increases as the profiles are compared further downstream. This is attributed to the use of the power-law edge velocity which

does not consider the actual velocity above the boundary layer in the flow field. Hence, for fig. 6.11c and fig. 6.11d the edge velocity is underestimated, resulting in excess momentum in the boundary layer. In contrast, the results in fig. 6.11a and fig. 6.11b show good agreement with the reference profile, but show an underestimation of the velocity for $\eta < 2$ for the finest mesh, which is attributed to a slight excess wall-shear stress applied.

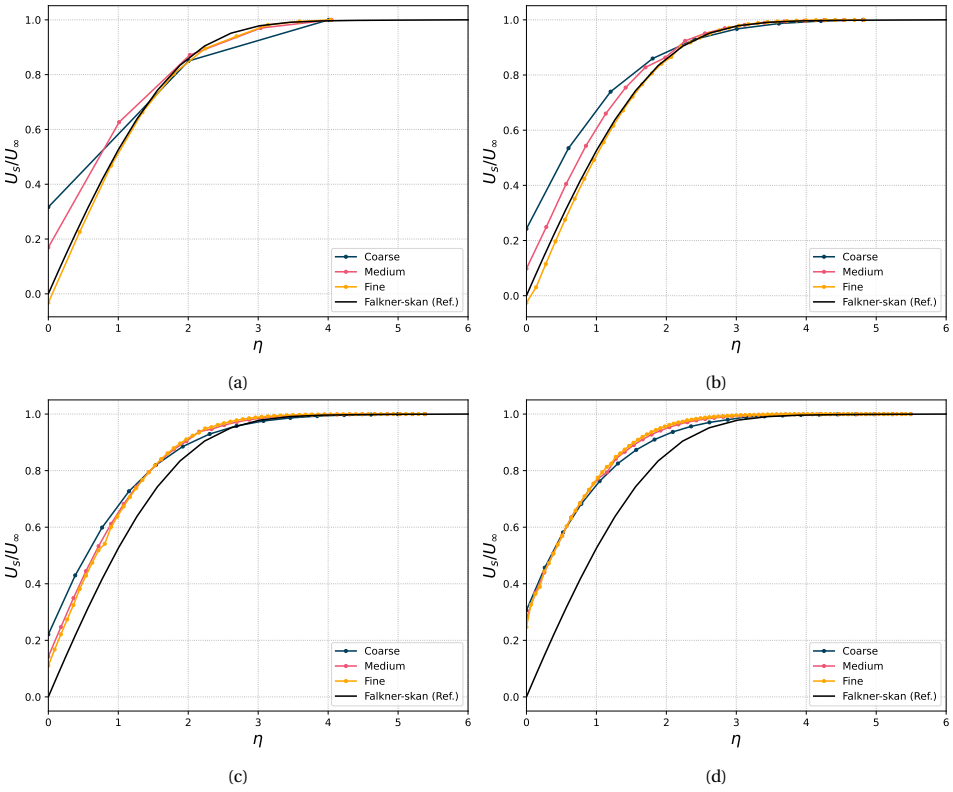

Figure 6.11: Wall-tangent velocity profiles at (a) $x_s = 0.1$, (b) $x_s = 1.0$, (c) $x_s = 2.0$, and (d) $x_s = 5.0$.

6.2.3. COMPARISON WITH LINEAR WALL MODEL

Next, the FSWM and linear wall model are compared using the fine mesh. The comparison is summarized in fig. 6.12. Interestingly, the linear wall model also exhibits an overestimation of the velocity moving away from the wall which worsens downstream of the wedge. Since laminar boundary layers are affected by the flow history, one explanation is that this is due to the accumulation of error upstream. For the linear wall model, a smaller error growth is seen due to the resolved nature of the simulation (beyond the tip) and the imposed no-slip condition at the wall. However, while the FSWM develops a slip velocity downstream of the wedge, the shape of the velocity profile remains identical in contrast to the linear wall model.

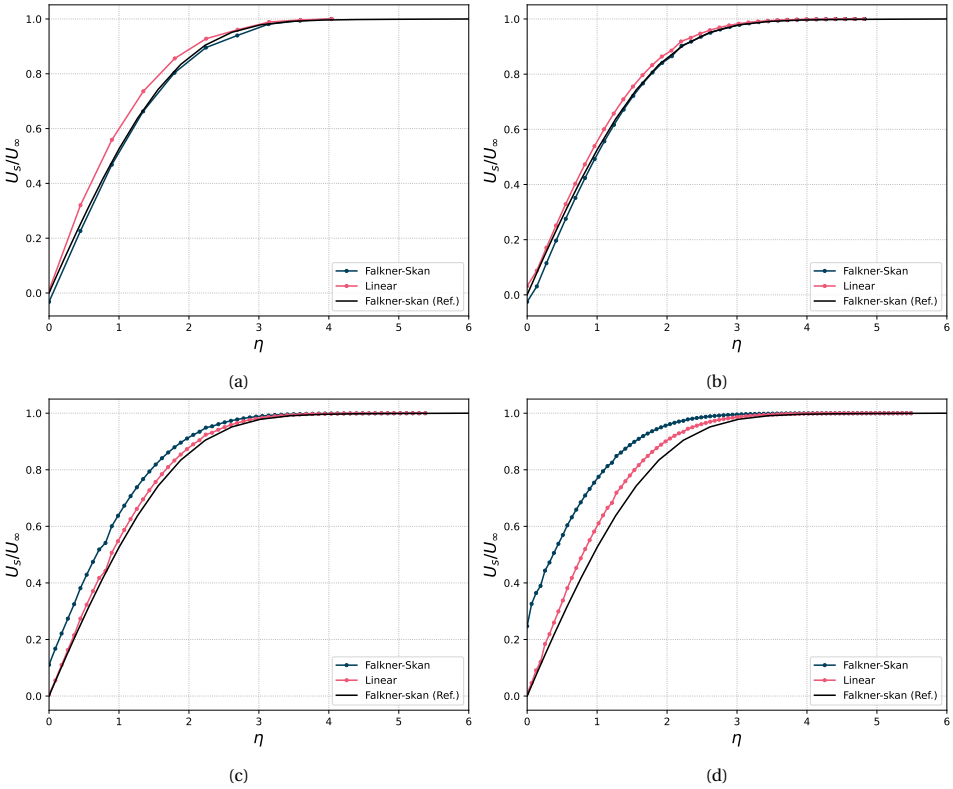

Figure 6.12: Comparison of the wall-tangential velocity profiles for the FSWM and linear wall model at (a) $x_s = 0.1$, (b) $x_s = 1.0$, (c) $x_s = 2.0$, and (d) $x_s = 5.0$.

6.3. LAMINAR NACA 0012

A final case to test the FSWM is performed by simulating laminar flow over a NACA 0012 airfoil at $\mathscr{R}e = 5 \times 10^3$ and $M = 0.5$. Reference data are retrieved from Dauricio and Azevedo (2022) and Swanson and Langer (2016). The airfoil makes a 0 deg angle of attack and based on the resolved simulation of Swanson and Langer (2016), trailing edge separation occurs at $x/c \approx 0.8$.

6.3.1. SETUP

A sketch of the domain is shown in fig. 6.13a and a close-up of the mesh is shown in fig. 6.13b. The airfoil is placed $6c$ away from the inlet and $9c$ away from the outlet, inside a domain with a volume of $16c \times 10c \times 1c$. A Riemann boundary condition is applied at the inlet, botom and top patches. A static pressure condition is imposed at the outlet and periodic boundary conditions are applied in the spanwise directions. The fluid properties are chosen such that a non-dimensional simulation is performed. The simulation parameters are summarized in table 6.7 and table 6.8.

Mach	$\mathscr{R}e$	L_x	L_y	L_z	SGS	Wall model	Fluid model
0.50	5×10^3	16.0	10.0	1.0	-	-	`non-dimensional gas`

Table 6.7: Main simulation parameters for the laminar NACA 0012.

X0	X1	Y0	Y1	Z0	Z1
`Riemann`	`Static pressure`	`Riemann`	`Riemann`	`Periodic`	`Periodic`

Table 6.8: Boundary conditions for the laminar NACA 0012.

Name	Min cell size [$\times 10^{-3}$]	Number of blocks	Number of cells [$\times 10^6$]
`Coarse`	7.81250	720	4.2
`Medium`	3.90625	2806	16.4
`Fine`	1.95312	13530	78.9

Table 6.9: Mesh settings for the laminar NACA 0012. Each block contains 16^3 cells.

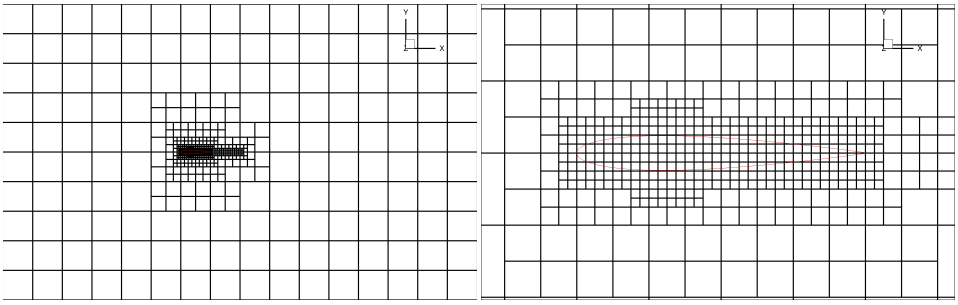

(a) (b)

Figure 6.13: Domain (a), and domain close-up (b) for the medium mesh.

6.3.2. MESH CONVERGENCE

Convergence is verified by observing the time series of C_L and C_D shown in fig. 6.14 for the three mesh levels. Since $\alpha = 0$, the lift generated should oscillate around zero which is seen in all three figures. The amplitude of the oscillation decrease as the mesh is refined. The u-velocity contours for the three meshes are shown in fig. 6.15.

The pressure distribution and skin friction distribution for three levels of mesh refinement are shown in fig. 6.16. Looking at the C_p curves, the pressure peak in fig. 6.16a is underestimated with the presence of a shallow laminar separation bubble between $0.3 < x/c < 0.5$, which based on resolved simulations is not present. This separation bubble is attributed to the higher shear stress applied downstream, causing flow-reversal near the wall. Note that the separation bubble moves further upstream as the mesh becomes more refined.

The predicted skin friction is in good agreement with the results from Dauricio and Azevedo (2022). The mesh refinements show that the skin friction peak is more accurately captured if the mesh is refined. table 6.10 shows the peak C_f obtained from the reference data and the present results of the fine mesh.

Downstream, the present results also follow the curve from Dauricio and Azevedo (2022) which is expected as a very similar laminar wall model formulation is used. As Swanson and Langer (2016) mentions, in their resolved simulation separation occurs at $x/c \approx 0.8$ which also roughly occurs in the present simulations. As mentioned earlier in chapter 4, a linear boundary condition is applied in separated regions ($\beta < -0.1980$) since the Falkner-Skan equations are not applicable in this regime. Due to this switch, a drop in shear stress is seen in the plot, marking the point of separation. This drop is due to the lower predicted shear from the linear approximation of the shear stress.

Table 6.10: Skin friction peak from reference and present simulations with the finest mesh.

	Dauricio	Swanson	Present (fine, FSWM)	Present (fine, Linear)
C_f [-]	0.116	0.145	0.117	0.089

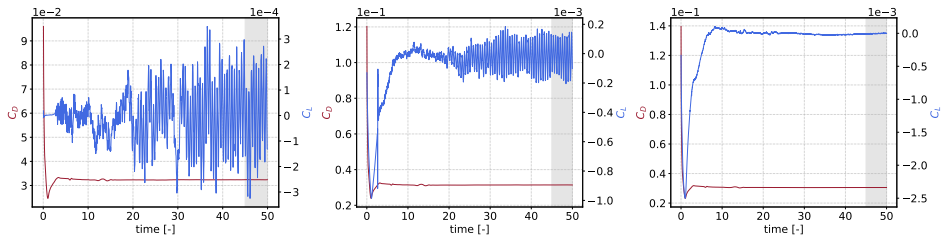

(a) (b) (c)

Figure 6.14: C_L and C_D convergence monitored for the three simulations performed with the FSWM: (a) coarse, (b) medium, and (c) fine.

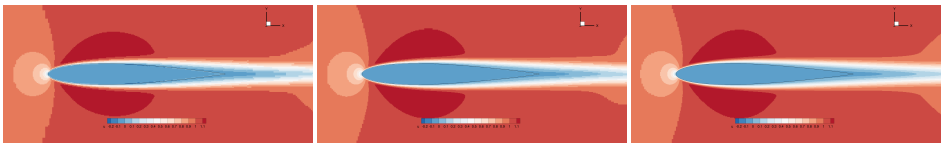

(a) (b) (c)

Figure 6.15: U-velocity contours for three levels of mesh refinement. 14 contour levels are used for $u \in [-0.2, 1.1]$.

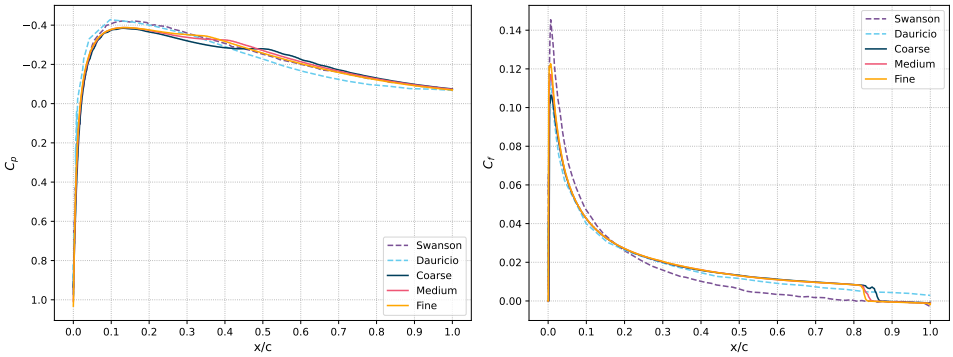

(a) (b)

Figure 6.16: Pressure (a), and (b) skin friction coefficient distribution for three levels of mesh refinement.

6.3.3. OTHER WALL MODEL FORMULATIONS

In Dauricio and Azevedo (2022), a viscous correction is applied to consider the reduction in effective flow angle and hence β which is tuned for their respective code. However, the correction value worsened the results in the present solver. As a result, this correction is not applied. Also in this case study, a simulation is performed using a linear wall model.

$$\chi\left(\frac{x}{c}, \mathscr{R}e_c\right) = \frac{1-(\sqrt{x/c})e^{-A\mathscr{R}e_c}}{1+e^{-A\mathscr{R}e_c}} \tag{6.3}$$

$$\hat{\beta} = \beta - |\beta|(1-\chi) \tag{6.4}$$

Figure 6.17 shows the pressure and skin friction distribution comparison between the linear and FSWM. Note that in contrast to the FSWM the plateau in the pressure distribution, physically indicating a separation bubble, does not exist with the linear wall model. The pressure peak is also more pronounced compared to the FSWM. Moreover, the linear wall model is in better agreement with the results of Swanson and Langer (2016) which is consistent as the linear wall model assumes that the boundary layer is well-resolved.

In fig. 6.17b, the advantage of the FSWM in a non well-resolved mesh is evident: the skin friction peak is better resolved compared to the linear WM. However, similarly to Dauricio and Azevedo (2022) the C_f is overpredicted downstream of the leading edge. In their work, however the integral shear was insufficient to trigger separation near the trailing edge.

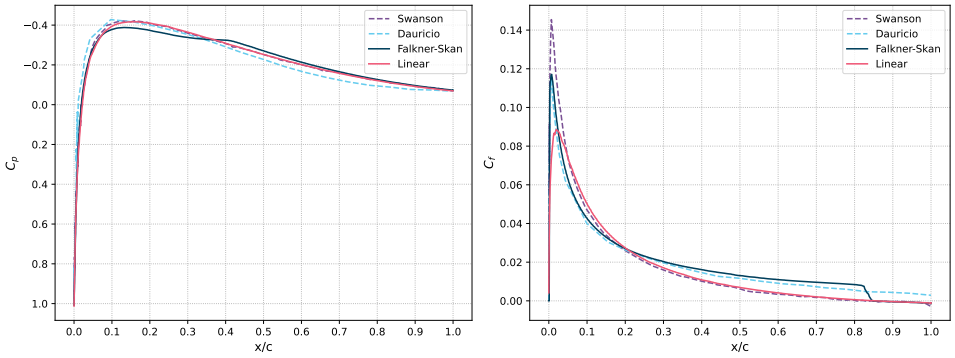

(a) (b)

Figure 6.17: Comparison of the pressure (a), and (b) skin friction coefficient distribution for the linear and Falkner-Skan wall model.

6.3.4. WEDGE ANGLE AND EDGE VELOCITY COMPUTATION

Bernoulli's principle is used to compute the incompressible approximation of the edge velocity. The accuracy of this approximation decreases as the simulated fluid is in the compressible regime, such as the present case study. Figure 6.18a compares the estimated U_e against numerical results from XFoil. In general the approximation is in

good agreement with XFoil, but as observed earlier, the pressure peak is underestimated which also implies an underestimation in the velocity returned by Bernoulli's principle. A slight underestimation is observed as well near the trailing edge. Additionally, also the computation of β is assessed by comparing the angle made between the panel and the freestream flow from XFoil. The results are shown in fig. 6.18b and shows a perfect agreement till $x/c \approx 0.80$, where flow separation occurs and the estimated β diverge. This makes sense as the XFoil curve computes the local angle of the geometry and the streamwise vector, while the present code computes the angle between the local flow tangent vector and freestream velocity vector. This may allow one to detect separation ($\beta < -0.1980$).

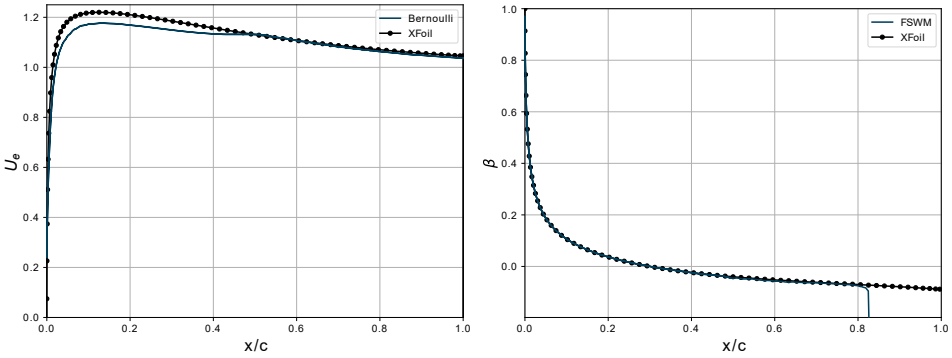

(a) (b)

Figure 6.18: Assessment of the Bernoulli approximation of U_e (a) and computation of the wedge angle (b) with results from XFoil.

6.4. LESFOIL

The next test case considers a case study from the LESFOIL project, where the feasibility of large eddy simulations to perform accurate numerical simulations of complex turbulent flows is assessed by simulating the flow around the A-airfoil at $M = 0.15$ and $\mathscr{R}e = 2.07 \times 10^6$. In the present study, an airfoil at 13.3° angle of attack is simulated to assess the performance of the laminar-turbulent sensor and observe if the laminar and turbulent regions are correctly identified. At this angle of attack the airfoil encounters a complex flow regime. At the leading edge, a small laminar region is present, which transitions to turbulence after $x/c = 0.14$. Near the trailing edge the turbulent boundary layer also separates. Results of this test case include a mesh convergence study with three levels of mesh refinement using the presently developed laminar-turbulent wall model, comparison wih other wall models and experimental data. The laminar-turbulent wall model integrates the earlier tested FSWM, turbulence sensor, and the existing EQWM.

6.4.1. SETUP

For the boundary conditions, a Riemann inflow boundary condition is applied with a unit flow velocity deflected 13.3°. The same is done for the top and bottom boundary patches. Periodic boundaries are used for the spanwise boundary conditions, and for the outlet a Dirichlet static pressure boundary condition is applied. The A-airfoil has a unit chord length with the span of the A-airfoil set to 20% of the chord. The length and height of the domain are 20 chords length. For all simulations in this case study, the Vreman SGS model (Vreman, 2004) is used and the fluid properties are set so that a non-dimensional simulation is performed. The main simulation parameters and boundary conditions are summarized in table 6.11 and table 6.12. Four levels of mesh refinements are used and the details are summarized in 6.13. Sketches of the used meshes are shown in appendix A.2.

Mach	$\mathscr{R}e$	L_x	L_y	L_z	SGS	Wall model	Fluid model
0.15	2.07×10^6	20.0	20.0	0.2	`vreman`	`EQWM, FSWM-EQWM, Linear-EQWM`	`non_dimensional_gas`

Table 6.11: Main simulation parameters for LESFOIL.

X0	X1	Y0	Y1	Z0	Z1
`Riemann`	`Static pressure`	`Riemann`	`Riemann`	`Periodic`	`Periodic`

Table 6.12: Boundary conditions for LESFOIL.

Name	Min cell size [$\times 10^{-3}$]	Number of blocks	Number of cells [$\times 10^6$]
`Very coarse`	4.687	4839	28
`Coarse`	2.344	6589	38
`Medium`	1.172	10369	60
`Fine`	0.586	42261	246

Table 6.13: Mesh settings for LESFOIL. Each block contains 16^3 cells.

6.4.2. SENSOR SENSITIVITY STUDY

This sensitivity analysis is performed to obtain a suitable value for the time integration constant τ, and update interval. Note that the optimization is not meant to be exhaustive, rather to obtain satisfactory value to showcase the laminar-turbulent wall model. The purpose is to obtain hyperparameters so that the marked laminar and turbulent regions is in agreement with the local flow field. In the subsequent LESFOIL simulations, the (known) transition point is imposed by forcing the wall model switching to occur at $x/c = 0.14$. No sensor feedback is provided so the sensor value depends only on the mesh resolution, time integration constant (τ), and the update interval. The convergence of the simulations performed are shown in appendix A.3.

TIME INTEGRATION CONSTANT

In general a larger τ results in a more sensitive sensor and cause smaller flow variations to be detected. A too large τ however, may cause large-scale transient flow features to be mistakenly seen as turbulence and as a result, the sensor detects transition prematurely. Similarly, if τ is too small, turbulent fluctuations are not detected. The goal of the sensor tuning is to obtain τ so that the sensor detects turbulence as much as can be resolved by the mesh.

Figure 6.19 shows the sensor value distribution for three levels of τ for the pressure (a) and suction side (b) of the airfoil. Note that the transition point is imposed at $x/c = 0.14$ and the flow is laminar and must be or close to zero upstream of this location. It was found that $\tau = 1 \times 10^{-1}$ has an excessively long "memory" such that the initial transient of the flow is still included in the time-filtered quantities of the sensor. As a result, the TKE computed led to spuriously high sensor values in the laminar region. This problem was not found for the $\tau = 1 \times 10^{-2}$ and $\tau = 1 \times 10^{-3}$ curves. On the contrary, the sensor value remains near-zero in the laminar region. Post-transition, $\tau = 1 \times 10^{-2}$ shows a similar behavior as $\tau = 1 \times 10^{-1}$ with large variation in the sensor value. $\tau = 1 \times 10^{-3}$ on the other hand shows higher frequency, but smaller amplitude oscillations after transition.

On the pressure side, similar observations are seen. The transition point on the pressure side is imposed at $x/c = 0.30$. A high sensor value is predicted in the laminar region by $\tau = 1 \times 10^{-1}$, in contrast to the other two curves. A larger variation in transition location is seen and as expected the transition location moves upstream as τ decreases (increasing sensitivity). However, all three curves are significantly off from the actual transition point.

A large peak near the stagnation line is seen in all curves. This is due to the shear stress approaching zero in the vicinity of the stagnation line. As the denominator is defined by the time-filtered friction velocity, the sensor consequently attains a large value.

$\tau = 1 \times 10^{-1}$ shows a closer transition prediction, but suffers from too high values predicted in the laminar region as explained earlier. $\tau = 1 \times 10^{-3}$ on the other hand is less sensitive than $\tau = 1 \times 10^{-2}$, resulting in a worse transition prediction on the pressure side. Based on the these observations a value of $\tau = 1 \times 10^{-2}$ is used.

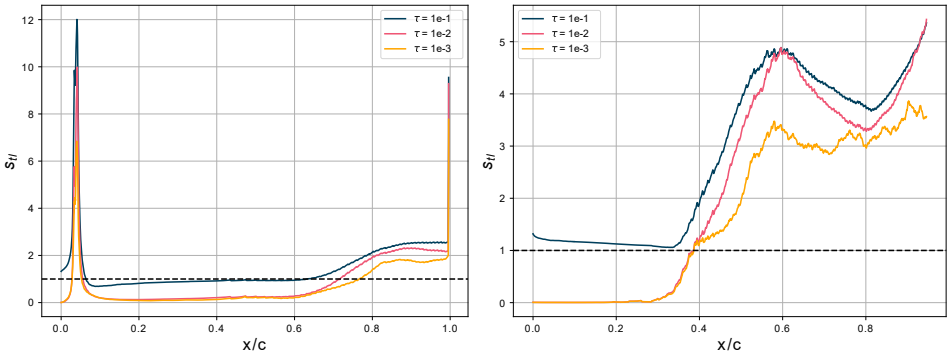

(a) (b)

Figure 6.19: Streamwise sensor value for three levels of time integration constant τ with an update interval of 100: (a) on the suction side, (b) and on the pressure side.

UPDATE INTERVAL

Executing the sensor algorithm every iteration significantly increases the computational cost. Preferably, the sensor is only updated every nth iteration. Figure 6.20 shows three levels of update intervals. A shorter update interval shows a more downstream prediction of the transition location and the post-transition behavior is more sensitive for a shorter update interval. Similar observations are seen on the pressure side. Comparing the figure with fig. 6.19 shows that a lower update interval has a similar effect as increasing τ. It was found that this is due to an identical effective weighting function as the timestep of each simulation is the same. Hence, an update interval of 100 iterations is also chosen.

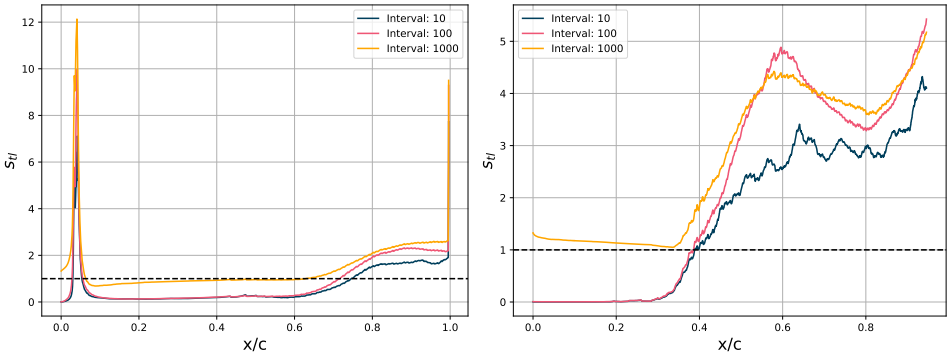

(a) (b)

Figure 6.20: Streamwise sensor value for three levels of update intervals for $1/\tau = 100$: (a) on the pressure side, (b) and on the suction side.

MESH SENSITIVITY

A small mesh sensitivity study is conducted with $1/\tau = 100$ and an update interval of 100. The velocity contour plot of each mesh is shown in fig. 6.21 and the sensor value distributions are shown in fig. 6.22. A great dependence on the mesh is observed, with the largest change in transition location when the mesh is refined to the medium mesh resolution.

The predicted transition location is in agreement with the turbulence seen in the velocity contours. In general, the transition location is predicted closely to where large turbulent structures are resolved by the mesh, but is significantly off from the true transition location ($x/c = 0.14$). In the shown flow fields in fig. 6.21c, the turbulent boundary layer still looks laminar near the true transition point. Hence, the sensor should not detect transition yet based on resolved flow information. The sensor formulation, reiterated in eq. (6.5), shows that the time-filtered TKE is based solely on the resolved contribution. Therefore, (parts of) the turbulent fluctuations must be captured by the mesh for the sensor to work. This implies that the mesh must, to some extent, capture the TKE near the transition point.

It is also remarked that the extremes are lower as the mesh becomes refined and also the sensor value distribution is lower, but remain well above the threshold value. The very coarse and coarse mesh did not detect any transition on the pressure side, which is attributed to the relatively thin boundary layer present. Additional figures of the sensor field on the suction and pressure side can be found in appendix A.4

$$s_{tl}(x_w, t) = \frac{\left\langle \sqrt{u_i' u_i'/2} \right\rangle}{\langle u_\tau \rangle} \tag{6.5}$$

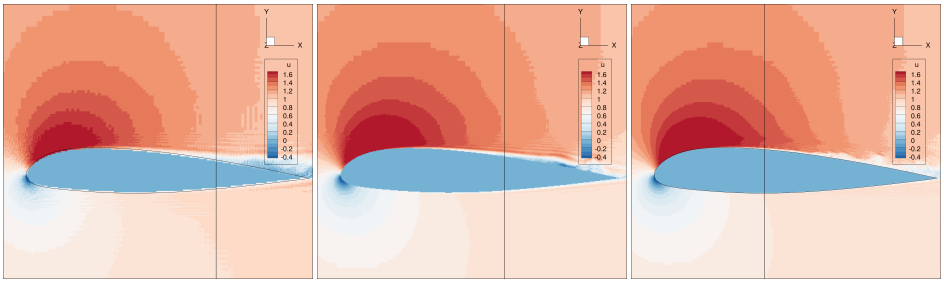

(a) (b) (c)

Figure 6.21: Three mesh resolutions for $1/\tau = 100$ and update interval of 100 iterations: (a) very coarse, (b) coarse, and (c) medium mesh.

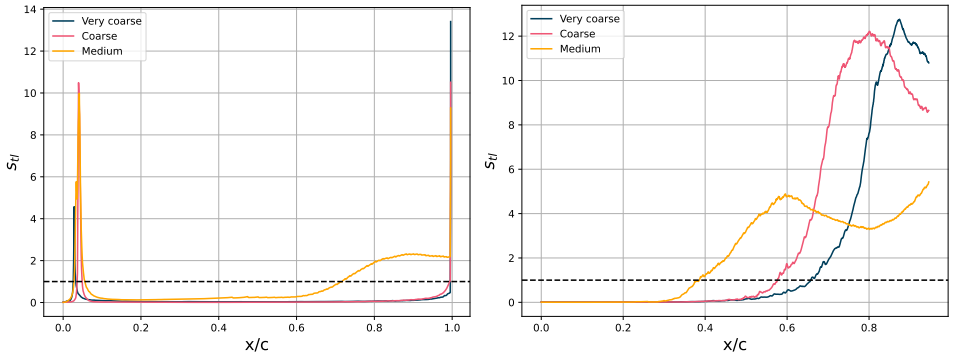

Figure 6.22: Sensor value distribution for three levels of mesh refinement: (a) on the pressure side, (b) and on the suction side.

6.4.3. MESH CONVERGENCE

A mesh convergence study is performed using the meshes described in table 6.13 and the developed laminar-turbulent wall model. The convergence is verified by observing the time series of the lift (C_L) and drag coefficient (C_D). Most simulations are performed till $t = 40$, where the statistics are recorded in the last ten convective time units (CTU). The convergence plots of all simulations performed are found in appendix A.

Figures 6.23a to 6.23c show the velocity contours for the three mesh levels from coarse to fine. Figures 6.23d to 6.23f also show the sensor contours associated with the predicted flow field. It is evident that the predicted flow field changes as the mesh becomes refined as more large-scale turbulence becomes resolved. For the flow field of the coarse mesh in fig. 6.23a, the mesh is insufficient to capture the near-wall unsteadiness but is able to resolve more of the boundary layer as it grows further downstream. Observing fig. 6.23d, the sensor only managed to mark the turbulent boundary layer near the trailing edge.

Doubling the mesh resolution clearly improves the predicted flow field as shown by fig. 6.23b. More unsteadiness is resolved in the aft part of the airfoil. However, the mesh is still inadequate to partly resolve fluctuations in the turbulent boundary layer upstream of $x/c \approx 0.40$. Nevertheless, the medium mesh greatly increased the region marked as turbulent. Note that on the pressure side, some spanwise variation is seen similar to the results obtained by Bodart and Larsson (2012). Lastly, note the marked turbulent region near the stagnation line which is due to the friction velocity, u_τ approaching zero in the vicinity of the stagnation line, as discussed earlier in section 6.4.2.

Further doubling the mesh resolution resolves more turbulence upstream and hence the turbulence sensor marks a more extensive region as turbulent. The spanwise variation is also decreased on the pressure side. The contours show that the utility of the sensor depends on the ability of the mesh to resolve turbulence. Moreover, the sensor corresponds well with the resolved flow field.

The pressure and skin friction coefficient distribution are shown in fig. 6.24. An overestimation of the pressure peak is observed compared to the WRLES and WMLES (with

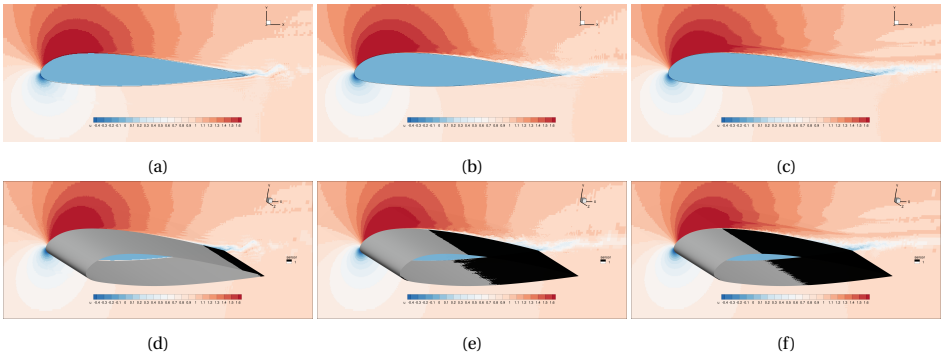

Figure 6.23: U-velocity contours for three levels of mesh refinement: (a) coarse, (b) medium, and (c) fine. 21 contour levels are used for $u \in [-0.4, 1.6]$. The sensor field is also shown for the three meshes: (d) coarse, (e) medium, and (f) fine.

an EQWM)performed by Tamaki et al. (2019). Earlier work from Lars et al. (2003), shows that the trailing edge separation is strongly coupled with the predicted pressure peak. Namely, an overestimation of the pressure peak is observed unless the trailing edge separation is predicted.

The present C_p curves also display small-scale oscillations in the laminar and near-transition region. This behavior in the present code is known and is earlier found to be attributed to using a coarse mesh, and simulating an underresolved boundary layer. However, fig. 6.24a shows that the oscillations persist over three mesh levels. A potential reason is found to be of similar origin: the FSWM attempts to model the laminar boundary layer, but is unresolved by meshes used.

A kink at $x/c = 0.14$ in the C_p curve is present in the reference WRLES curve and denotes the laminar separation bubble and consequent transition. For the present simulations, the kinks are also present at $x/c \approx 0.36$ for the medium mesh and $x/c \approx 0.25$ for the fine mesh but are not able to capture a laminar separation bubble. For the coarse mesh the transition point occurs at $x/c \approx 0.86$ and a small kink in the curve is observed. According to experimental data and WRLES data, trailing edge separation occurs around $x/c = 0.83$. However, this is not predicted by the present simulations as shown by fig. 6.24b.

The C_f curves clearly show the laminar-turbulent transition point. Since the transition point is predicted too aft downstream, also the skin friction peak is severely underestimated. Namely, the velocity has already been decelerated over the airfoil when the transition point occurs and so the transition to a turbulent boundary layer provides a far lower C_f increase. Just after the transition point, the skin friction drops significantly and consequently rises rapidly again. This is the transition physically taking place after switching to the turbulent EQWM. A similar behavior is observed from the results of Chalmers University of Technology shown in Lars et al. (2003, pg. 80–96). Lastly, the laminar skin friction peak is well-matched but the overall the C_f in the laminar region is overestimated by all three meshes. This is ascribed to the inability to capture the laminar-separation bubble just before the true transition point ($0.12 < x/c < 0.14$).

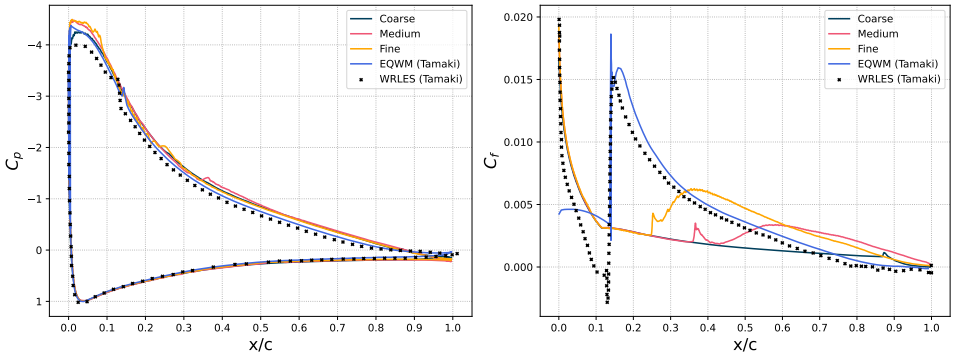

(a) (b)

Figure 6.24: Pressure (a), and (b) skin friction coefficient distribution for three levels of mesh refinement.

6.4.4. COMPARISON TO OTHER WALL MODELS

The presently developed laminar-turbulent wall model is compared to other wall model formulations and reference WRLES, and EQWM from Tamaki et al. (2019). The compared wall models include the standard EQWM, and the laminar-turbulent linear-EQWM, where the linear wall model replaces the FSWM. As shown earlier, the sensor is unable to capture the transition point near $x/c = 0.14$ with the present fine mesh. For a fair comparison, the sensor is forced to switch at $x/c = 0.14$. The C_p and C_f comparison are shown in fig. 6.25. All simulations from the present solver overestimate the pressure peak compared to the reference WRLES, which is partially in agreement with EQWM simulation performed by Tamaki et al. (2019) and earlier work performed summarized in Mellen et al. (2003). The trailing edge pressure is also overestimated as the present solver settings and mesh used are unable to predict both trailing edge separation and laminar separation bubble (Mellen et al., 2003).

Compared to the other wall model formulations of the present solver, the FSWM-EQWM performs the best overall. Namely, a good agreement is found for both the laminar and turbulent skin friction peak. As expected, the EQWM is only able to predict a single peak and also seems to transition well before $x/c = 0.14$. For the EQWM results of Tamaki et al. (2019), a linear profile is assumed prior to transition, which explains the differences between the present EQWM results.

Since the laminar boundary layer is underresolved by the present mesh, the linear approximation poorly estimates the laminar C_f peak, but shows a better transition behavior than the FSWM-EQWM. It is believed that the lower shear applied in the laminar region, provides the flow additional momentum towards $x/c = 0.14$. Due to the higher velocity, a greater change in shear stress is provided, resulting in a more rapid transition. Both the EQWM and FSWM-EQWM exhibit a similar transition behavior in the C_f plot.

The velocity as well as sensor contours for the FSWM-EQWM (left) and linear-EQWM (right) are shown in fig. 6.26. Note that the sensor value is computed but not fed back to the simulation. Remark that the predicted laminar and turbulent regions with forced switching at $x/c = 0.14$ produces a near-identical sensor field compared to fig. 6.23f. This confirms that the sensor field is limited by the present mesh resolution. A similar

sensor field is obtained for the linear wall model. However, turbulent patches are also predicted in the laminar region, which is found to be caused by higher TKE present near the leading edge which could be due to larger numerical noise present in the linear-EQWM simulation as evidenced by the oscillations seen in fig. 6.25a.

Since the sensor and FSWM are proposed to be added in conventional industrial WMLES, the additional computational time due to these new features must be considered. Table 6.15 compares the wall-clock time of the conventional EQWM and the hybrid wall-modeling routine after simulating 40 convective time units (CTU) for two meshes. It must be remarked that the newly added features are unoptimized, hence the performance deficit can be alleviated. Still, the addition of a turbulence sensor and laminar wall model only brings a 2.8% decrease in solver performance with the fine mesh which is deemed acceptable.

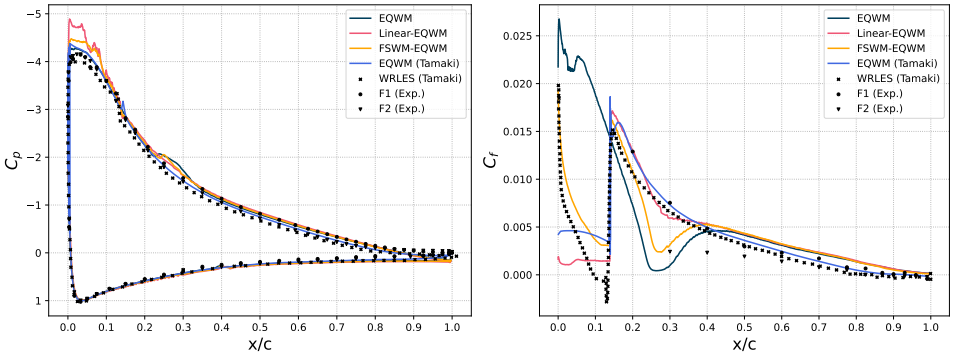

Figure 6.25: Comparison of the pressure (a), and (b) skin friction coefficient distribution with different wall-model formulations.

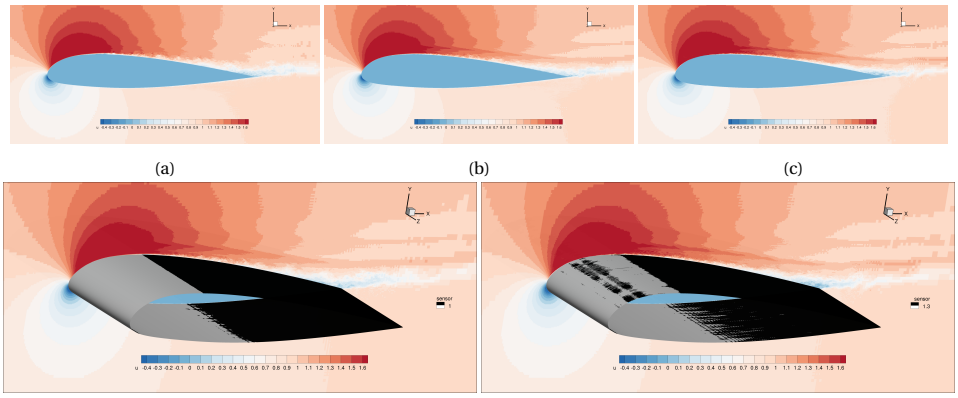

Figure 6.26: U-velocity contour for the (a) EQWM, (b) FSWM-EQWM and (c) linear-EQWM. 21 contour levels are used for $u \in [-0.4, 1.6]$. The sensor field is also shown for the (d) FSWM-EQWM, and (e) Linear-EQWM.

Table 6.14: Comparison of the lift and drag predictions from several wall models and reference data.

	EQWM (Present)	Linear-EQWM	FSWM-EQWM	EQWM (Tamaki)	WRLES (Tamaki)	F1 (Exp.)	F2 (Exp.)
C_L	1.637	1.704	1.671	1.576	1.496	1.56	1.515
C_D	0.0446	0.0224	0.0301	-	-	0.0204	0.0308

Table 6.15: Wall-clock time given in (hh:mm) while simulating 40 CTU with two wall-modeling routines performed on the fine and coarse mesh.

	EQWM	Hybrid Wall Model
Fine	05:54	06:04
Coarse	00:19	00:20

7

Conclusion and Discussion

A conclusion of the findings and answer to the questions posed at the start of the thesis is provided together with the author's recommendation for future work.

7.1. Conclusion

In wall-modeled large eddy simulation (WMLES), typically a wall model assuming an equilibrium turbulent boundary layer is used. This equilibrium assumption is less restrictive than believed, and to some extent is also applicable to non-equilibrium flows (Larsson et al., 2016). However, the standard equilibrium wall models (EQWM) are not applicable to laminar boundary layers. While the extent of laminar boundary layer in high Reynolds number flows is limited, poorly resolving this region can have detrimental effect on the predicted flow field. For typical industrial WMLES mesh resolutions, the laminar boundary layer will almost always be underresolved, and hence poorly predicted.

The present thesis has attempted to extend the applicability of WMLES by firstly implementing and combining a Falkner-Skan-based laminar wall model (FSWM) with conventional EQWM and secondly, implementing a turbulence detecting sensor to automatically switch between the two wall models. In doing so, the following sub-questions are answered:

Can the Falkner-Skan wall model improve the shear stress prediction compared to the linear wall model?

Shear stress prediction of the FSWM and linear wall model are compared in most case studies performed in the present thesis. In the resolved cases, such as the laminar flat plate and the laminar NACA 0012 it is concluded that the linear wall model outperforms the FSWM as the shear stress is in better agreement with reference data. This is attributed to the less restrictive formulation and a mesh being able to fully resolve the boundary layer. Namely, the velocity profile near the wall of a laminar boundary layer is indeed linear and hence the shear stress and wall-normal derivative naturally follows from the linear wall model.

However, in regions where the laminar boundary layer is underresolved such as near the leading edge and in high Reynolds number flows, the FSWM captures the shear stress more accurately as the linear assumption does not hold. Results from the LESFOIL case study further shows that indeed the linear wall model is inadequate in obtaining appropriate amount of shear in underresolved regions. It must be emphasized that there are still deficiencies in the presently implemented FSWM. Notably, the discrepancies in the predicted velocity profiles and boundary layer properties for the resolved cases studied.

WHAT ARE THE DIFFERENCES IN PREDICTED VELOCITY FIELD OF WALL-BOUNDED FLOWS COMPARED TO AN EQWM?

The comparison of the velocity contours between the EQWM and FSWM-EQWM laminar-turbulent wall model (LTWM) for the LESFOIL case shows that a thinner boundary layer has developed over the suction side of the airfoil. The boundary layer only starts to thicken significantly after the transition at $x/c = 0.14$. In contrast, a boundary layer already develops near the leading edge and large turbulent fluctuations become resolved much earlier due to a more developed turbulent boundary layer. Besides that, no significantly noticeable features distinguish the flow field between the two simulations in the LESFOIL case, partially due to the inability of the present mesh to resolve the trailing edge separation and laminar separation bubble before transition.

HOW ROBUST IS THE TURBULENCE DETECTING SENSOR IN DISTINGUISHING LAMINAR AND TURBULENT REGIONS OVER A SURFACE?

Results of LESFOIL simulations performed with three levels of refinement show that the sensor is greatly dependent on whether the mesh is able to resolve large-scale turbulence. This is expected since the sensor formulation is based on the resolved turbulent kinetic energy, therefore the mesh must be sufficiently fine for the solver to capture parts of the turbulent fluctuations. In this regard, the sensor is unrobust.

The sensor sensitivity study performed also shows that for the given mesh, changing the sensor threshold value does not necessarily result in a significantly better transition location. As transition occurs, the sensor value rises rapidly, and so the distance travelled by lowering the threshold value is marginal. Still, lowering the threshold value too much however may result in false-positives i.e., parts of the laminar region may be marked as turbulent. Notably, the sensor consistently marks the vicinity near the stagnation line as turbulent if a threshold value of 1.0 is used.

However, it must be emphasized that this sensitivity study only considered the LESFOIL case and additional cases must be simulated to check the robustness of the sensor. Especially, the effect of the time integration constant must be more thoroughly investigated on a wider range of test cases. Results show that setting this integration constant too high tends to result in high sensor values in laminar regions. Similarly, setting the integration constant too low causes the sensor to be too sensitive, resulting in more downstream predictions of the transition location.

WHAT IS THE DIFFERENCE IN COMPUTATIONAL COST BETWEEN THE PROPOSED WALL MODEL AND THE EQWM?

WMLES is applied to analyze complex unsteady, turbulent flows in wall-bounded flows, with significant cost reduction compared to LES. Therefore, features designed to im-

prove the accuracy of WMLES must also be cost-efficient to maintain the cost effectiveness of WMLES over LES. Earlier it was shown that the added sensor and laminar wall model resulted in an increase of 2.8% to the wall-clock time of the LESFOIL simulation using the finest mesh. Larsson et al. (2016) show that for WMLES of a NACA 0012 airfoil at 2.5 deg at $\mathscr{R}e_c = 10^6$, equivalent to $\mathscr{R}e_\tau = 10^3$ requires approximately a quarter of the cost of traditional LES. Hence, a slight increase of 3% over the WMLES computing time is minimal. Especially, given that the discussed features in the present code are yet to be optimized, which could reduce this cost penalty.

The above answered sub-questions help to address the main research question posed at the beginning of the present thesis.

HOW DOES THE PROPOSED LAMINAR-TURBULENT WALL MODEL IN A SENSOR-BASED APPROACH COMPARE TO A TURBULENT EQUILIBRIUM WALL MODEL?

The LTWM without a priori known transition location shows to be more accurate than results obtained with the EQWM. The benefit of the LTWM is evident in the skin friction distribution, where the laminar peak is well captured, and as well as the turbulent peak if the transition location is known. The C_p curve differs moderately between the two wall models, with only the pressure peak becoming more overestimated by the LTWM. However, this is due to the solver being unable to capture the laminar separation bubble and trailing edge separation with the given mesh. Mellen et al. (2003) have shown that capturing these two flow features is crucial to reach a good agreement with the experimental and reference data.

For the LTWM with sensor feedback, the used mesh in combination with the sensor is unable to come close to the true transition location as part of the TKE must be resolved for the sensor to detect a turbulent boundary layer. Hence comparing the C_p and C_f distributions, the present LTWM with sensor feedback can be seen as worse than the EQWM. Especially given additional computational costs incurred. Still, if the sensor can be tuned or a better sensor formulation can be found to detect the transition location more accurately without needing to resolve (part of) the outer layer TKE, the LTWM has the potential to outperform the EQWM. Especially in cases where the laminar boundary layer has a significant effect on the downstream flow field.

7.2. FUTURE WORK AND RECOMMENDATIONS

Many improvements for a LTWM to improve the applicability of WMLES are left to be investigated at the end of this thesis. Several recommendations and future work are described below.

STAGNATION POINT DETECTION ALGORITHM

In the present code, the stagnation line is imposed, however, for laminar wall models to be incorporated in conventional WMLES, the stagnation line must be found in-the-loop. This prevents the need of knowing the stagnation line a priori and makes the LTWM more robust and applicable as the stagnation line is generally not known a priori.

ROBUST REINITIALIZATION ALGORITHM APPLICABLE TO 3D GEOMETRIES

The developed reinitialization method is tested for two-dimensional shapes. However, the present mehod may break down for three-dimensional geometries. For an arbitrary shape, many advecting fronts may collide and consequently break down the distance field. Since two-dimensional geometries are only tested, the fronts usually collide at the maximum of the distance field. However, this is generally not the case, especially if the zero level set is non-linear.

Also in the present implementation, a better method to track and prevent the interface of the advecting fronts in affecting the converged distance field must be found. Currently, this is done by logging non-monotonic convergence and (prematurely) stopping the reinitialization algorithm after ten non-monotonic iterations. However, this has found to decrease the accuracy of the obtained distance field.

IMPROVE SENSOR TURBULENCE DETECTION

In-the-loop prediction of the transition location is crucial for LTWM-like wall-modeling formulations to succeed and consequently make WMLES more widely accepted. Section 6.4 suppports this as evidenced by significant improvements in the skin friction prediction given an a priori known transition location. However, the transition location is predicted too far downstream, resulting in a poorly reconstructed flow field and C_f distribution. One way to improve the sensor, while limiting computational cost, is to perform better tuning of the presented sensor formulation described in chapter 5. In contrast to the original formulation proposed by Bodart and Larsson (2012), a constant time integration is proposed. The time integration as well as the update interval can be tuned to obtain better predictions. How the sensor performs in various other turbulent, high Reynolds number cases, must also be investigated.

Another approach is to adopt a different sensor formulation to detect turbulence. One suggestion, which retains the current formulation, is to also include the sub-grid contribution of the TKE in the sensor value by coupling the SGS model to the sensor. Bodart and Larsson (2012) mention a range for the threshold value based on numerous TCF cases of a moderate range of $\mathscr{R}e_\tau$. However, this range is applicable only if the turbulent flow is fully resolved. In LES, and especially WMLES this is not the case. Hence, a lower threshold value must be chosen. However, if typical WMLES grid resolution is insufficient to resolve enough of the TKE, then lowering the threshold may cause laminar regions to be falsely identified as turbulent. The information from a SGS model may provide a way to avoid such errors.

ACCURATE DETERMINATION OF VELOCITY DISTRIBUTION

Accurate approximation of the velocity distribution above the laminar boundary layer is quintessential for modeling them. In the conducted case studies, the use of a potential flow approximation of the edge velocity has shown to underestimate the edge velocity compared to the "true" velocity distribution. Merely probing the edge velocity is difficult for general-purpose codes. Large probing distances mean a greater chance that the point lies inside a nearby geometry. Moreover, the boundary layer grows downstream and therefore the probing distance must scale accordingly. For robustness, a technique to obtain a better estimate of the local edge velocity without the need of probing further than 2Δ away is recommended to advance laminar wall-modeling.

EXTEND VALIDATION OF FALKNER-SKAN WALL MODEL

Validation work of the present FSWM shows reasonable agreement with reference data in the laminar NACA 0012, and the wedge flow case, but poor results for the flat plate case. The latter is partially attributed to the difficulty of matching the physical streamwise coordinate with the Blasius streamwise coordinate, which is an important variable in the Blasius equation. For the wedge flow, the results are mixed, showing a streamwise variation in the results obtained. The FSWM is able to capture the skin friction peak for the laminar NACA 0012. However, in the resolved downstream region, the skin friction is overestimated. Therefore, it is recommended to extend the validation work.

BIBLIOGRAPHY

Bae, H. J., Lozano-Durán, A., Bose, S. T., & Moin, P. (2019). Dynamic slip wall model for large-eddy simulation. *Journal of Fluid Mechanics*, *859*, 400–432. https://doi.org/10.1017/jfm.2018.838

Baurle, R., Tam, C.-J., Edwards, J., & Hassan, H. (2003). Hybrid simulation approach for cavity flows: Blending, algorithm, and boundary treatment issues. *AIAA journal*, *41*(8), 1463–1480. https://doi.org/10.2514/2.2129

Blasius, H. (1908). Grenzschichten in flussikeiten mit kleiner reibung. *Z. Angew. Math. Phys.*, *56*, 1–37.

Bodart, J., & Larsson, J. (2012). Sensor-based computation of transitional flows using wall-modeled large eddy simulation. *Center for Turbulence Research Annual Briefs*, *2012*, 229–240. https://web.stanford.edu/group/ctr/ResBriefs/2012/20_bodart.pdf

Bose, S. T., & Moin, P. (2014). A dynamic slip boundary condition for wall-modeled large-eddy simulation. *Physics of Fluids*, *26*(1), 015104. https://doi.org/10.1063/1.4849535

Bose, S. T., & Park, G. I. (2018). Wall-modeled large-eddy simulation for complex turbulent flows. *Annual Review of Fluid Mechanics*, *50*(1), 535–561. https://doi.org/10.1146/annurev-fluid-122316-045241

Catchirayer, M., Boussuge, J.-F., Sagaut, P., Montagnac, M., Papadogiannis, D., & Garnaud, X. (2018). Extended integral wall-model for large-eddy simulations of compressible wall-bounded turbulent flows. *Physics of Fluids*, *30*(6), 065106. https://doi.org/10.1063/1.5030859

Chapman, D. R. (1979). Computational aerodynamics development and outlook. *AIAA journal*, *17*(12), 1293–1313.

Choi, H., & Moin, P. (2012). Grid-point requirements for large eddy simulation: Chapman's estimates revisited. *Physics of Fluids*, *24*(1), 011702. https://doi.org/10.1063/1.3676783

Coder, J. G., & Maughmer, M. D. (2014). Computational fluid dynamics compatible transition modeling using an amplification factor transport equation. *AIAA Journal*, *52*(11), 2506–2512. https://doi.org/10.2514/1.J052905

Dauricio, E. T., & Azevedo, J. L. F. (2022). A wall model for external laminar boundary layer flows applied to the wall-modeled les framework. https://doi.org/10.2139/ssrn.4142016

Duda, B. M., Fares, E., Kotapati, R., Li, Y., Staroselsky, I., Zhang, R., & Chen, H. (2019). Capturing laminar to turbulent transition within the lbm based cfd solver powerflow. In *Aiaa scitech 2019 forum*. https://doi.org/10.2514/6.2019-1832

Fedkiw, R. P., Aslam, T., Merriman, B., & Osher, S. (1999). A non-oscillatory eulerian approach to interfaces in multimaterial flows (the ghost fluid method). *Journal of*

Computational Physics, *152*(2), 457–492. https://doi.org/10.1006/jcph.1999.6236

Goc, K., Bose, S., & Moin, P. (2021). Large-eddy simulation of the nasa high-lift common research model. *Annual Research Briefs*, 3–16. https://web.stanford.edu/group/ctr/ResBriefs/2021/03_Goc.pdf

Gonzalez, C., Karp, M., & Moin, P. (2020). Wall-stress modeling for laminar boundary layers in coarse grids. *Annual Research Briefs 2020*. http://web.stanford.edu/group/ctr/ResBriefs/2020/10_Gonzalez.pdf

Herbert, T. (1984). Analysis of the subharmonic route to transition in boundary layers. In *22nd aerospace sciences meeting*. https://doi.org/10.2514/6.1984-9

Hickel, S., Touber, E., Bodart, J., & Larsson, J. (2012). A parametrized non-equilibrium wall-model for large-eddy simulations. *Proceedings of the Summer Program 2012*.

Hughes, T. J. R., Mazzei, L., Oberai, A. A., & Wray, A. A. (2001). The multiscale formulation of large eddy simulation: Decay of homogeneous isotropic turbulence. *Physics of Fluids*, *13*(2), 505–512. https://doi.org/10.1063/1.1332391

Kawai, S., & Larsson, J. (2012). Wall-modeling in large eddy simulation: Length scales, grid resolution, and accuracy. *Physics of Fluids*, *24*(1), 015105. https://doi.org/10.1063/1.3678331

Kim, J., Moin, P., & Moser, R. (1987). The turbulence statistics in fully developed channel flow at low reynolds number. *Journal of Fluid Mechanics*, *177*, 133–166. https://doi.org/10.1017/S0022112087000892

Klebanoff, P. S. (1954). *Characteristics of turbulence in a boundary layer with zero pressure gradient* (Technical Notes). NASA. https://ntrs.nasa.gov/citations/19930084922

Kubacki, S., Simoni, D., Lengani, D., & Dick, E. (2020). An extended version of an algebraic intermittency model for prediction of separation-induced transition at elevated free-stream turbulence level. *International Journal of Turbomachinery, Propulsion and Power*, *5*(28). https://doi.org/10.3390/ijtpp5040028

Langtry, R. B., & Menter, F. R. (2009). Correlation-based transition modeling for unstructured parallelized computational fluid dynamics codes. *AIAA Journal*, *47*(12), 2894–2906. https://doi.org/10.2514/1.42362

Lars, D., Davor, C., Jochen, F., Michael, L., A., Chris, M., & Wolfgang, R. (2003). *Lesfoil: Large eddy simulation of flow around a high lift airfoil*. Springer Berlin. https://doi.org/10.1007/978-3-540-36457-3

Larsson, J., Kawai, S., Bodart, J., & Bermejo-Moreno, I. (2016). Large eddy simulation with modeled wall-stress: Recent progress and future directions. *Mechanical Engineering Reviews*, *3*(1), 15–00418. https://doi.org/10.1299/mer.15-00418

Lee, J. H., Kwon, Y. S., Hutchins, N., & Monty, J. P. (2012). Spatially developing turbulent boundary layer on a flat plate. https://doi.org/10.48550/ARXIV.1210.3881

Lee, J., Cho, M., & Choi, H. (2013). Large eddy simulations of turbulent channel and boundary layer flows at high reynolds number with mean wall shear stress boundary condition. *Physics of Fluids*, *25*(11), 110808. https://doi.org/10.1063/1.4819342

Lopes, R., Eça, L., & Vaz, G. (2020). On the numerical behavior of rans-based transition models. *Journal of Fluids Engineering*, *142*(5). https://doi.org/10.1115/1.4045576

Lozano-Durán, A., Bose, S., & Moin, P. (2020). Performance of wall-modeled les for external aerodynamics in the nasa juncture flow. *Annual Research Briefs*, 37–48.

Lozano-Durán, A., & Bae, H. J. (2020). Self-critical machine-learning wall-modeled les for external aerodynamics. *Annual Research briefs*. http://web.stanford.edu/group/ctr/ResBriefs/2020/20_LozanoDuran.pdf

Mancinelli, C., Livesu, M., & Puppo, E. (2018). Gradient Field Estimation on Triangle Meshes. In M. Livesu, G. Pintore, & A. Signoroni (Eds.), *Smart tools and apps for graphics - eurographics italian chapter conference*. The Eurographics Association. https://doi.org/10.2312/stag.20181301

McBride, B. J., Zehe, M. J., & Gordon, S. (2002). *Nasa glenn coefficients for calculating thermodynamic properties of individual species* (Technical Publication). NASA. https://ntrs.nasa.gov/citations/20020085330

Mellen, C. P., Frohlich, J., & Rodi, W. (2003). Lessons from lesfoil project on large-eddy simulation of flow around an airfoil. *AIAA Journal*, *41*(4), 573–581. https://doi.org/10.2514/2.2005

Menter, F. R., Matyushenko, A., Lechner, R., Stabnikov, A., & Garbaruk, A. (2022). An algebraic lctm model for laminar–turbulent transition prediction. *Flow, Turbulence and Combustion*, 1–29. https://doi.org/10.1007/s10494-022-00336-8

Menter, F. R., Smirnov, P., Liu, T., & Avancha, R. (2015). A one-equation local correlation-based transition model. *Flow, Turbulence and Combustion*, *95*, 583–619. https://doi.org/10.1007/s10494-015-9622-4

Moser, R. D., Haering, S. W., & Yalla, G. R. (2021). Statistical properties of subgrid-scale turbulence models. *Annual Review of Fluid Mechanics*, *53*(1), 255–286. https://doi.org/10.1146/annurev-fluid-060420-023735

Nikitin, N. V., Nicoud, F., Wasistho, B., Squires, K. D., & Spalart, P. R. (2000). An approach to wall modeling in large-eddy simulations. *Physics of Fluids*, *12*(7), 1629–1632. https://doi.org/10.1063/1.870414

Panton, R. L. (2013). Incompressible flow. John Wiley & Sons, Ltd. https://doi.org/10.1002/9781118713075.ch25

Pasquariello, V., Bunk, Y., Eberhardt, S., Huang, P.-H., Matheis, J., Ugolotti, M., & Hickel, S. (2023). Gpu-accelerated simulations for evtol aerodynamic analysis. *AIAA SCITECH 2023 Forum*, 2107. https://doi.org/10.2514/6.2023-2107

Piomelli, U., Balaras, E., Pasinato, H., Squires, K. D., & Spalart, P. R. (2003). The inner–outer layer interface in large-eddy simulations with wall-layer models. *International Journal of heat and fluid flow*, *24*(4), 538–550. https://doi.org/10.1016/S0142-727X(03)00048-1

Pohlhausen, E. (1921). Der wärmeaustausch zwischen festen körpern und flüssigkeiten mit kleiner reibung und kleiner wärmeleitung. *ZAMM - Journal of Applied Mathematics and Mechanics / Zeitschrift für Angewandte Mathematik und Mechanik*, *1*(2), 115–121. https://doi.org/10.1002/zamm.19210010205

Pope, S. B. (2000). *Turbulent flows*. Cambridge University Press. https://doi.org/10.1017/CBO9780511840531

Rosenhead, L. (1963). *Laminar boundary layers: An account of the development, structure and stability of laminar boundary layers in incompressible fluids, together with a description of the associated experimental techniques*. Oxford University Press.

Sandhu, J. P. S., & Ghosh, S. (2021). A local correlation-based zero-equation transition model. *Computers & Fluids*, *214*, 104758. https://doi.org/10.1016/j.compfluid.2020.104758

Shur, M. L., Spalart, P. R., Strelets, M. K., & Travin, A. K. (2008). A hybrid rans-les approach with delayed-des and wall-modelled les capabilities. *International Journal of Heat and Fluid Flow*, *29*(6), 1638–1649. https://doi.org/10.1016/j.ijheatfluidflow.2008.07.001

Spalart, P. R. (1988). Direct simulation of a turbulent boundary layer up to $\mathscr{R}e_\theta$ = 1410. *Journal of Fluid Mechanics*, *187*, 61–98. https://doi.org/10.1017/S0022112088000345

Sussman, M., Smereka, P., & Osher, S. (1994). A level set approach for computing solutions to incompressible two-phase flow. *Journal of Computational Physics*, *114*(1), 146–159. https://doi.org/10.1006/jcph.1994.1155

Swanson, R., & Langer, S. (2016). *Comparison of naca 0012 laminar flow solutions: Structured and unstructured grid methods* (Technical Memorandum). NASA. https://ntrs.nasa.gov/citations/20160003623

Tamaki, Y., Fukushima, Y., Kuya, Y., & Kawai, S. (2019). Large-eddy simulation of airfoil flows at near-stall conditions using equilibrium/non-equilibrium wall models. In *Aiaa scitech 2019 forum*. https://doi.org/10.2514/6.2019-1646

Tamaki, Y., & Kawai, S. (2021). Wall modeling for large-eddy simulation on non-body-conforming cartesian grids. *Phys. Rev. Fluids*, *6*, 114603. https://doi.org/10.1103/PhysRevFluids.6.114603

Thwaites, B. (1949). Approximate calculation of the laminar boundary layer. *Aeronautical Quarterly*, *1*(3), 245–280. https://doi.org/10.1017/S0001925900000184

Unglehrt, L., Kreuzinger, J., & Manhart, M. (2022). A wall model for high-fidelity large-eddy simulation. *The 18th Conference on Fluid Flow Technologies*. https://www.cmff.hu/papers/CMFF22_Final_Paper_PDF_20.pdf

Van Driest, E. R. (1956). On turbulent flow near a wall. *Journal of the Aeronautical Sciences*, *23*(11), 1007–1011. https://doi.org/10.2514/8.3713

Vreman, A. W. (2004). An eddy-viscosity subgrid-scale model for turbulent shear flow: Algebraic theory and applications. *Physics of Fluids*, *16*(10), 3670–3681. https://doi.org/10.1063/1.1785131

Walters, D. K., & Cokljat, D. (2008). A three-equation eddy-viscosity model for reynolds-averaged navier–stokes simulations of transitional flow. *Journal of Fluids Engineering*, *130*(12). https://doi.org/10.1115/1.2979230

White, F. (2006). *Viscous fluid flow*. McGraw-Hill.

Whitmore, M., Griffin, K., Bose, S., & Moin, P. (2021). Large-eddy simulation of a gaussian bump with slip-wall boundary conditions. *Annual Research Briefs*, 45–58. https://web.stanford.edu/group/ctr/ResBriefs/2021/06_Whitmore.pdf

Woodruff, S. (2021). WMLES of Boundary-Layer Transition. *AIAA Scitech 2021 Forum*. https://doi.org/10.2514/6.2021-1841

Woodruff, S. (2022). WMLES of K-Type and Bypass Boundary-Layer Transition. *AIAA Scitech 2022 Forum*. https://doi.org/10.2514/6.2022-1070

Yang, X. I. A., Sadique, J., Mittal, R., & Meneveau, C. (2015). Integral wall model for large eddy simulations of wall-bounded turbulent flows. *Physics of Fluids*, *27*(2), 025112. https://doi.org/10.1063/1.4908072

Yang, X. I. A., Zafar, S., Wang, J.-X., & Xiao, H. (2019). Predictive large-eddy-simulation wall modeling via physics-informed neural networks. *Phys. Rev. Fluids*, *4*, 034602. https://doi.org/10.1103/PhysRevFluids.4.034602

Yang, X. I. A., & Griffin, K. P. (2021). Grid-point and time-step requirements for direct numerical simulation and large-eddy simulation. *Physics of Fluids*, *33*(1), 015108. https://doi.org/10.1063/5.0036515

Zaki, T. A., & Durbin, P. A. (2021). Chapter eight - transition to turbulence. In P. Durbin (Ed.), *Advanced approaches in turbulence* (pp. 373–397). Elsevier. https://doi.org/10.1016/B978-0-12-820774-1.00014-8

A

APPENDIX

A.1. FALKNER-SKAN DATA TABLE

Table A.1: f'' data points used for the Falkner-Skan surrogate model.

β \ η	0	1	2	3	4
-0.198	2.7496e-02	2.1781e-01	3.5445e-01	2.8924e-01	9.8349e-02
0	0.4696e-00	4.3564e-01	2.5851e-01	6.9252e-02	7.1251e-03
0.67	1.0306e-00	4.3657e-01	9.8353e-02	1.0161e-02	4.3987e-04
1.33	1.3837e-00	3.7314e-01	4.8430e-02	2.9890e-03	8.1526e-05
2.0	1.6623e-00	3.1438e-01	2.6927e-02	1.1283e-03	2.1610e-05

A.2. LESFOIL GRID SKETCHES

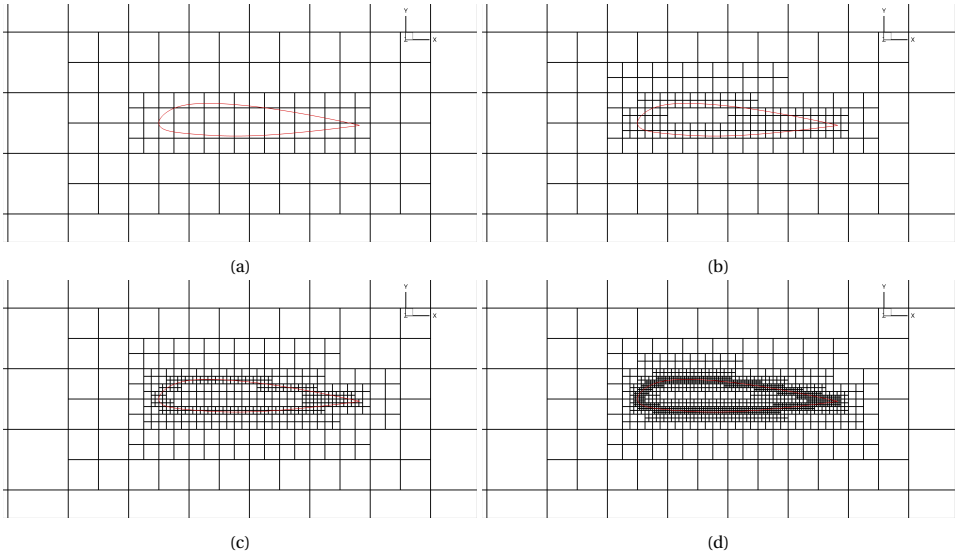

Figure A.1: Sketches of the four meshes used in the LESFOIL case study: (a) very coarse, (b) coarse, (c) medium, (d) fine.

A.3. LESFOIL CONVERGENCE PLOTS

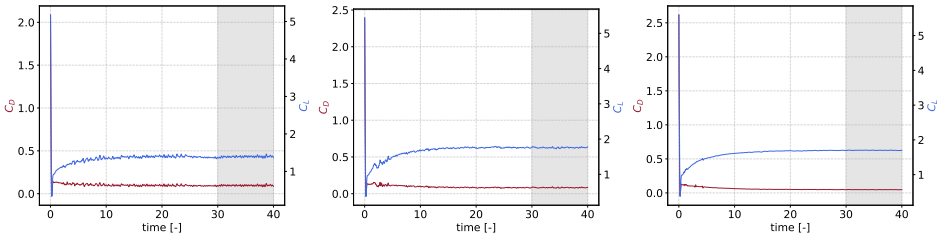

(a) (b) (c)

Figure A.2: Convergence of the LESFOIL simulations with hard-coded wall-model switching for the sensor sensitivity study (a) very coarse, (b) coarse, (c) medium. The gray-shaded area indicates the time interval in which statistics have been computed.

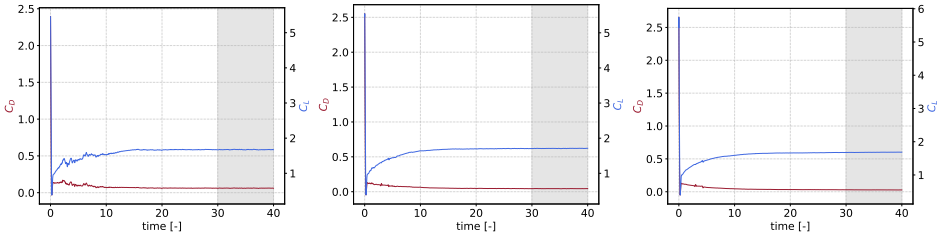

(a) (b) (c)

Figure A.3: Convergence of the LESFOIL simulations with sensor feedback using the FSWM-EQWM hybrid wall model with the coarse (a), medium (b) and fine (c) mesh. The gray-shaded area indicates the time interval in which statistics have been computed.

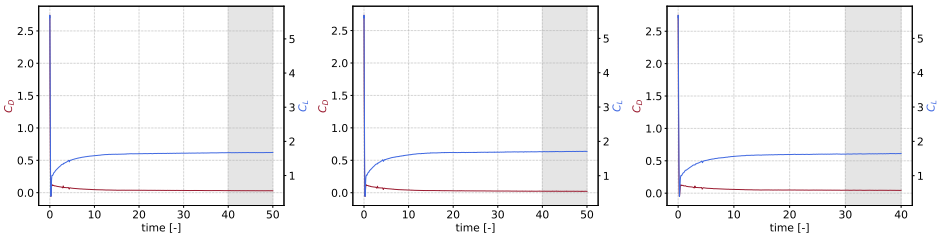

(a) (b) (c)

Figure A.4: Convergence of the LESFOIL simulations with hard-coded wall-model switching with the FSWM-EQWM (a), Linear-EQWM (b), and (c) EQWM. The gray-shaded area indicates the time interval in which statistics have been computed.

A.4. LESFOIL SENSOR CONTOUR PLOTS

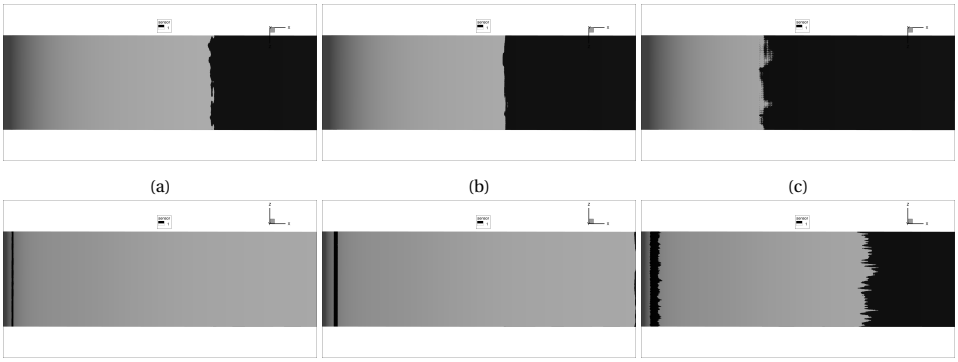

(a) (b) (c)

(d) (e) (f)

Figure A.5: Sensor contours of the pressure (d)-(f) and suction sides (a)-(c) in the mesh sensitivity study. (a) and (d) show the very coarse mesh, (b) and (e) the coarse mesh, and (c) and (f) the medium mesh sensor contour.

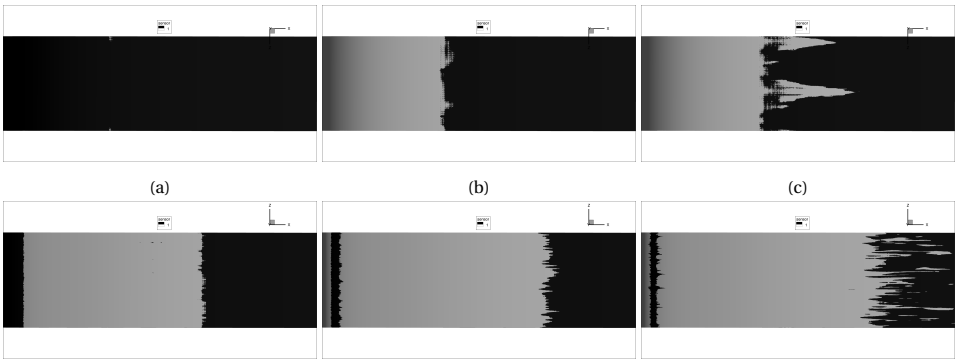

(a) (b) (c)

(d) (e) (f)

Figure A.6: Sensor contours of the pressure (d)-(f) and suction sides (a)-(c) for increasing levels of τ. (a) and (d) show the $\tau = 10$, (b) and (e) the $\tau = 100$, and (c) and (f) the $\tau = 1000$ sensor contour.

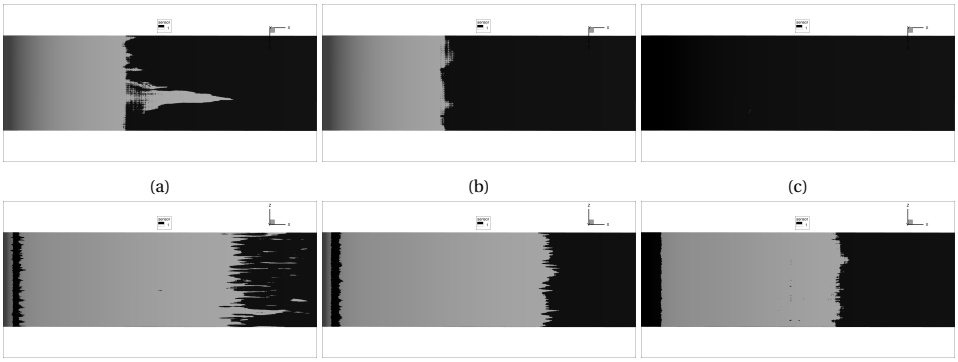

(a) (b) (c)

(d) (e) (f)

Figure A.7: Sensor contours of the pressure (d)-(f) and suction sides (a)-(c) for increasing update intervals (UI). (a) and (d) show the $UI = 10$, (b) and (e) the $UI = 100$, and (c) and (f) the $UI = 1000$ sensor contour.